Spring 2010

Evaluation of liquefaction-induced lateral spreading in the midwest

Kermit Nathanial Applegate

EVALUATION OF LIQUEFACTION-INDUCED LATERAL SPREADING IN THE MIDWEST

by

KERMIT NATHANIAL APPLEGATE

A THESIS

Presented to the Faculty of the Graduate School of the

MISSOURI UNIVERSITY OF SCIENCE AND TECHNOLOGY

In Partial Fulfillment of the Requirements for the Degree

MASTER OF SCIENCE IN CIVIL ENGINEERING

2010

Approved by:

Dr. Ronaldo Luna, Advisor
Dr. Abdeldjelil Belarbi
Dr. J. David Rogers
Dr. Yu-Ning Ge

ABSTRACT

The Central United States is home to several seismically active regions: the Wabash Valley Seismic Zone, the South Central Illinois Seismic Zone, and the New Madrid Seismic Zone. All three of these regions are capable of inducing large ground motion throughout the Mississippi Valley and along the eastern border of Missouri. This has been supported by many paleoseismic studies conducted throughout the region, which have identified numerous instances of liquefaction phenomena. The fluvial deposition process associated with the Mississippi river valley makes it a prime location for possible liquefaction and lateral spreading effects. However, there are few studies pertaining to lateral spreading phenomena in the Midwest. This thesis investigates the current state-of-practice in lateral spreading estimation and determines an evaluation process adequate for the specific needs of the Midwest. A bridge site along the Mississippi River, the Bill Emerson Memorial Bridge, is evaluated for lateral spreading and recommendations for the applicability of the process to the Midwest are made.

ACKNOWLEDGMENTS

I would like to extend my sincerest gratitude to my graduate advisor, Dr. Ronaldo Luna, for all the opportunities that I have been afforded throughout my academic ventures. If it were not for his persistent encouragement and timely feedback, the contents of this thesis may have remained in draft form. I would also like to express my appreciation to my graduate committee members, Dr. Abdeldjelil Belarbi, Dr. J. David Rogers and Dr. Yu-Ning Ge, for sharing their expertise and time throughout my studies.

I would be remiss if I did not address the many individuals from the professional community that aided in my academic pursuit by providing valuable data. So . . . thank you Bill Lawrence for sharing your collection of research on the topic; thank you Conor Watkins for the stellar LIDAR data; thank you Missouri DOT staff, i.e. Alan Miller and Greg Sanders; and thank you Illinois DOT staff, i.e. Ve'niecy Pearman-Green, Robert Graeff, Mary Lamie, and Casey Teckenbrock. The data that you provided was instrumental in completing this thesis.

I must also express my appreciation to Missouri University of Science and Technology for their financial support. The Chancellor's Fellowship in conjunction with graduate teaching and research assistantships helped me fund my graduate endeavors. In addition, a research grant from the National Science Foundation aided my academic success.

Finally, special thanks to the one's that made everything I do possible, my parents. The moral strength of my mother and the inspiring memory of my father guide my hand in all that I do . . . thank you.

TABLE OF CONTENTS

LIST OF ILLUSTRATIONS

LIST OF TABLES

1. INTRODUCTION

1.1. HISTORY OF LATERAL SPREADING

Our host planet has shaken the foundations of many civilizations since the inception of man. Written accounts of earthquakes as early as 780 B.C. describe terrifying earth motions that produced widespread damage west of Xian, China in the Shanxi Province, and Italian records highlight a sixteen year period of seismic activity prior to the infamous Mt. Vesuvius eruption in A.D. 79 (Kramer, 1996). However, reports of lateral spreading from these accounts are non-existent.

The lack of identification does not confirm the lack of existence though. In a paper presented to the National Center for Earthquake Engineering Research (NCEER), Leslie Youd (1997) deciphered documentation that detailed bridge damage during the 1868 Hayward, CA and 1886 Charleston, SC earthquakes. He noticed that compressional damage, indicative of laterally spreading ground, was reported in several locations. This illuminates the possibility that the lack of lateral spreading record is due to a lack of understanding rather than the absence of such phenomena.

Current knowledge about lateral spreading stems from the dramatic events of 1964. In that year, the most devastating earthquake damage to bridge structures in U.S. history was incurred by a Mw=9.2 earthquake that struck Prince William Sound on March 27 (Youd, 1997). Three months later, a Mw=7.5 earthquake struck Niigata, Japan. The combined carnage of these two earthquakes brought widespread attention to the mechanics of soil failure during seismic activity. Typical damage fomented by the Alaska and Niigata earthquakes is illustrated in Figures 1-1 and 1-2, respectively.

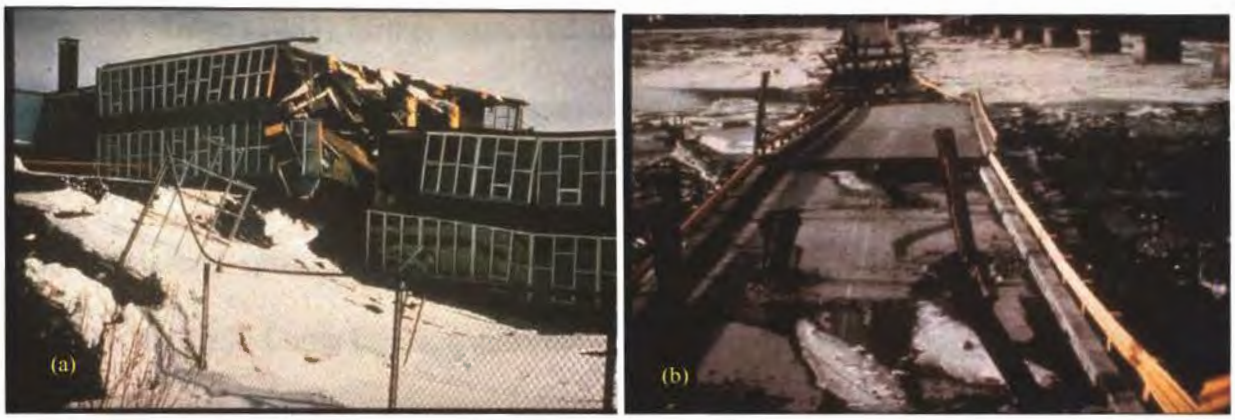

Figures 1-1a,b: Typical damage from the 1964 Alaska earthquake (a) school (b) 20-mile river bridge (http://www.smate.wwu.edu/teched/geology/GeoHaz)

Figure 1-2a,b: Typical damage from 1964 Niigata, Japan Earthquake (a) factory (b) Shinano River Bridge (http://www.johnmartin.com/earthquakes/eqshow/images)

The ensuing research developed theories on liquefaction and identified the different manifestations of liquefaction failures, e.g. lateral spreading. By 1978, the first formal definition of lateral spreading was published. Varnes (1978), in his work on ground deformation and slope failures, described lateral spreading with the following description:

> "[Ground] Movements may involve fracturing and extension of coherent material . . . owing to liquefaction or plastic flow of subjacent material. The coherent upper units may subside, translate, rotate, or disintegrate, or they may liquefy and flow."

Whitman (1985) further narrowed the scope of the definition to incorporate only ground deformations resulting from liquefaction-induced lateral spreading. Based on the definition proposed by Whitman (1985), the last few decades have produced several cases of lateral spreading throughout the world. Incidents of significant importance include: the 1989 Loma Prieta, California earthquake, the 1995 Hyogoken-Nanbu, Japan earthquake, the 1999 Kocaeli, Turkey earthquake, the 2001 Bhuj, India earthquake, the 2007 Peruvian earthquake, and the 2009 Honduras earthquake (an in-depth discussion of the Honduras earthquake is provided in chapter five of this thesis).

A more detailed discussion on liquefaction and lateral spreading is presented in chapter three of this thesis.

1.2. LATERAL SPREADING AND THE MIDWEST

Since the definition of liquefaction-induced lateral spreading, there have been no earthquakes of large enough magnitude to initiate lateral spreading in the Midwest, but research done to quantify the 1811-1812 New Madrid Seismic Zone (NMSZ) events, as discussed in chapter two, has identified several locations of ancient liquefaction via paleoseismic studies. One report from this series of earthquakes described the lateral movement of soil blocks that slid towards the Mississippi River (Obermeier, 1988), which indicates that lateral spreading most likely occurred.

Despite the lack of historical record, it is prudent to address the potential hazard in the Midwest. For example, a fault zone near Kutch, India shares a similar seismic setting as the NMSZ. It is an intra-plate fault that had not released an earthquake since 1819, but on January 26, 2001 (182 years later) a M_w=7.7 earthquake ended its period of

dormancy (Chen et. al, 2005). It was nicknamed the forgotten earthquake, but ignorance was not bliss in this case.

1.3. LATERAL SPREADING MODELS AND THE MIDWEST

The paucity of large magnitude earthquakes (M_w>5.0) in the Midwest and the unique fault structure of the NMSZ present many difficulties for estimating the degree of lateral spreading. As discussed in chapter three, most of the lateral spreading models have been developed from a composite database of recorded seismic events that induced lateral spreading. In these models, the fault characteristics strongly influence the ground response. Unfortunately, the NMSZ is an intra-plate fault which reacts distinctly different than an inter-plate fault, and the complete sum of recorded intra-plate earthquakes is not sufficient to develop an independent model. Therefore, all of the empirical models are influenced by earthquakes in regions with high seismicity and inter-plate fault slips, i.e. Japan and California. To further complicate a Midwest application of these models, the attenuation relationships associated with highly seismic regions are different than in the Midwest. The bedrock in seismically active regions is highly fractured by their propensity for seismic activity, so ground motion attenuates much quicker. For these reasons, the empirical models that have been developed are not conducive to an evaluation in the Midwest.

More advanced models that incorporate mechanistic or numerical modeling techniques have been developed for evaluating lateral spreading extents, but these advanced models require knowledge of the fault rupture characteristics. Since there have been no measured strong ground motions for a NMSZ earthquake series, the required

information is not available in the Midwest. Therefore, these methods are difficult to apply to this region.

1.4. RESEARCH OBJECTIVES

Due to the distinct nature of the NMSZ and the lack of historical lateral spreading studies in the region, there are no clear processes for estimating lateral spreading displacements in the Midwest. Therefore, the objectives of this thesis were to:

- Identify the methods currently available for estimating lateral spreading displacements
- Compare the data available in the Midwest to the data required for each method
- Select the most appropriate models for a site in the Midwest
- Determine the sensitivity of each selected model to variations in critical parameters (i.e. ground slope and free-face height)
- Evaluate the appropriate models to estimate the anticipated lateral spreading at a Midwest bridge site

1.5. CONTRIBUTION OF THESIS

The content of this thesis evaluates the impact of the discrepancies between the Midwest seismic setting and current empirically based models. An analysis procedure that includes four empirically based lateral spreading models, along with a list of their advantages and disadvantages, has been developed in order to progress the current state-of-practice for lateral spreading evaluation in the Midwest. To illustrate the process, a

lateral spreading evaluation was conducted on a section of the Mississippi River's flood plain near the Bill Emerson Memorial Bridge.

1.6. THESIS ORGANIZATION

The information provided within this thesis has been organized to facilitate the evaluation of lateral spreading in the Midwest, and the progression of the information parallels the evaluation process. Therefore, the thesis begins with background information about the unique setting of the NMSZ before addressing the development of lateral spreading theory. After addressing lateral spreading theory, the available techniques for estimating lateral spreading displacements are explored to determine their compatibility with a Midwest lateral spreading evaluation. Following the selection of the appropriate models, this thesis describes the results of a sensitivity analysis conducted on two critical parameters within the selected models (i.e. ground slope and free-face height). The same models were then utilized to estimate the anticipated lateral displacement at the Bill Emerson Memorial Bridge site (a site in Cape Girardeau, MO).

As a compliment to this research, the author was afforded the opportunity to engage in an earthquake reconnaissance investigation after the May 28, 2009 event in the Sula Valley of Honduras, where evidence of liquefaction, lateral spreading, and related damage were documented. A description of the ensuing activities and discoveries are presented in Chapter 5. Finally, conclusions are presented to synthesize the information presented in the thesis, and recommendations are made for future research.

The appendix provides a step-by-step procedure for preparing a lateral spreading evaluation spreadsheet that contains each of the selected models.

2. REGIONAL SEISMIC BACKGROUND

2.1. TECTONIC EVOLUTION

In the beginning . . . well, in late Pre-Cambrian time, convective currents within the earths core were driving sea-floor spreading and continental rifting within cratonic masses around the globe. The South American and African plates were joined. This conjoined craton was rotating and pulling away from the North American craton. Widespread incipient rifts capable of separating these massive super-continents were attempting to spawn new oceans (Yungul, 1971).

The Atlantic Ocean is a testament to the capabilities associated with the rifting process, but not all the rifts conceived oceans. A litany of failed rifts, called aulacogen, are strewn about the surviving continents calling attention to the dynamic nature of our planet and influencing its evolution (Mooney, 1983). Within the North American continent, at least two large aulacogen networks have been discovered from the late Pre-Cambrian activity: the Central North American Rift System (CNARS) and the New Madrid Rift Complex (NMRC) (Ervin and McGinnis, 1975). The CNARS extends from Lake Superior into Kansas, and the NMRC reaches from the Gulf of Mexico up into Illinois and Missouri.

2.1.1. New Madrid Rift Complex. The NMRC was proposed by Braile et. al (1986) to contain the Reelfoot Rift with extensions to the Northwest (St. Genevieve Fault Zone), Northeast (Wabash Valley Fault Zone), and East (Rough Creek Fault Zone). The NMRC is illustrated in Figure 2-1 with the Mississippi Embayment and the NMSZ.

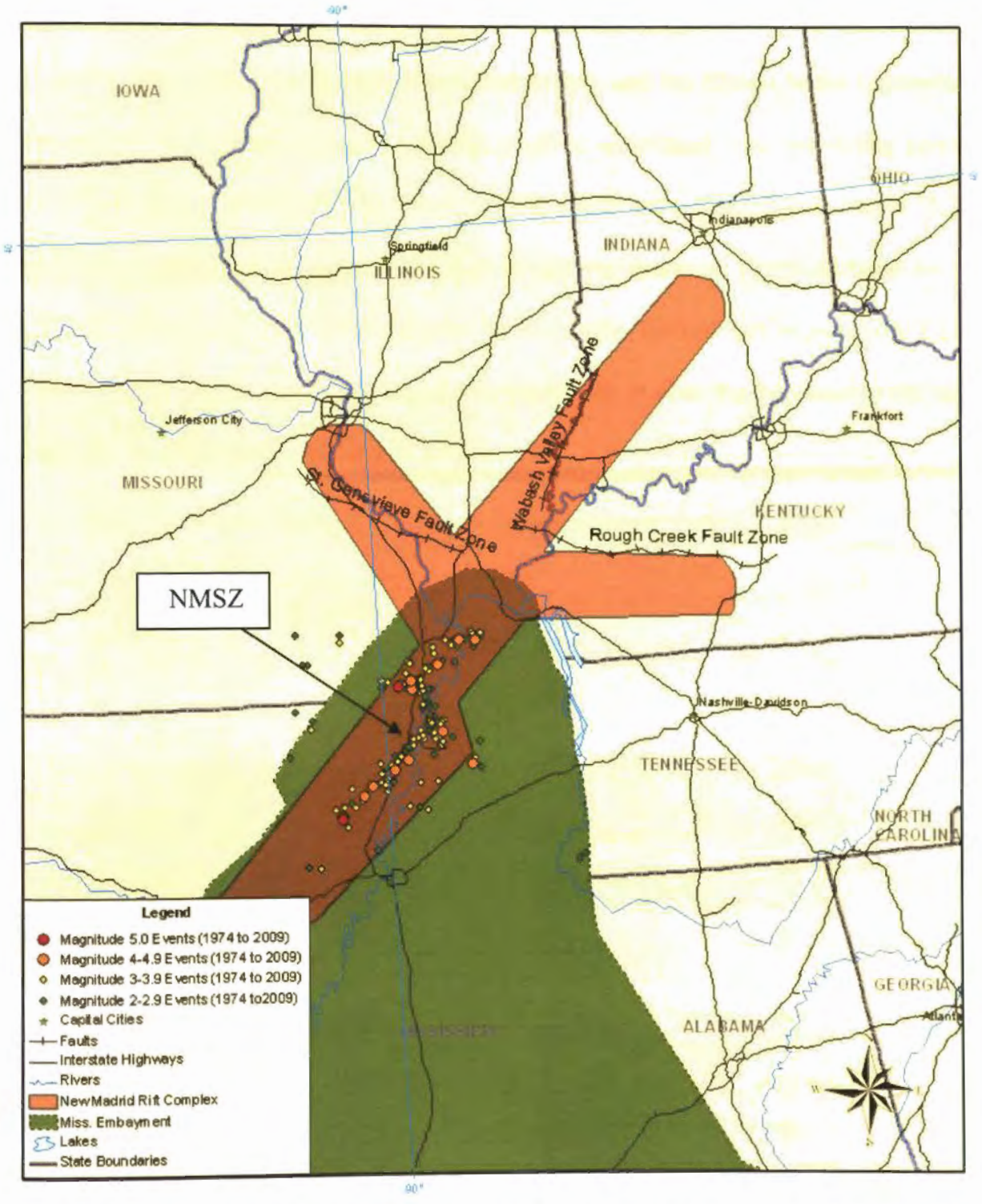

Figure 2-1: New Madrid Rift Complex with Estimated Fault Locations, Mississippi Embayment, and NMSZ (modified from Braile et al., 1986)

Despite the relative distinctness of these zones, as shown in a contemporary map, their existence is the product of the same late Pre-Cambrian tectonic rifting.

2.1.1.1 Evolution of the New Madrid Rift Complex. During late Pre-Cambrian time, the region that now hosts the Mississippi Embayment and the Illinois basin experienced epeirogenic, or widespread, uplift. Mantle material associated with the rifting process was being emplaced into the local crust causing a vast area to swell (see Figure 2-2a). The brittle upper-crust material could not sustain the immense forces induced by the crustal expansion, so graben or axial rifts formed within the uplifted regions (see Figure 2-2b). Rifting forces and active denudation continued to alter the landscape until early Paleozoic time (Ervin and McGinnis, 1975).

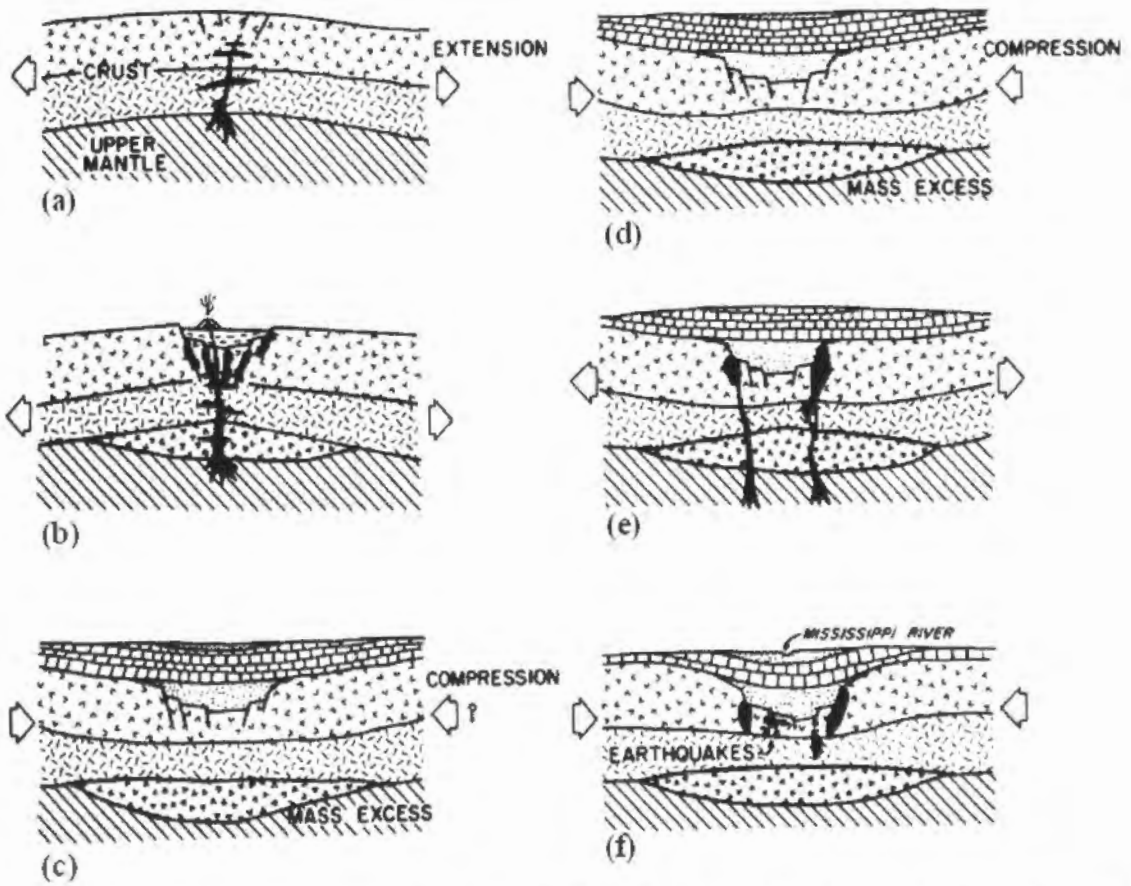

Figure 2-2: Schematic Cross Section of NMRC illustrating the evolution of the rift complex through time (a) Late Precambrian: Incipient Rifting (b) Late Precambrian-Early Cambrian: Rifting (c) Early to Middle Paleozoic: Subsidence (d) Late Paleozoic: Subsidence, Localized Deformation (e) Mesozoic: Uplift, Reactivation (f) Late Mesozoic to Present: Subsidence, Compression (taken from Braile et al., 1986)

Once the rifting forces were dissipated, a state of disequilibrium was set into place. The mafic intrusions within the local crust resulted in an increased relative density of the uplifted regions, so a long phase of subsidence overtook the area (see Figure 2-2c). The subsiding region began to accumulate sediment in its exposed valley and displace excess mantle material laterally. The shifting mantle material helped to create the Ozark uplift and the Nashville Dome which both flank the Mississippi Embayment today (Ervin and McGinnis, 1975).

The Ozark Uplift and Nashville Dome continued to accumulate mass, while the contemporaneous development of the Pascola Arch and the Clifton Saddle began to transect the Northern edge of the Mississippi Embayment. Eventually, the Ozark Uplift, Pascola Arch, Clifton Saddle and Nashville Dome were a contiguous mass isolating the Northern and Southern portions of the Mississippi Embayment (Ervin and McGinnis, 1975). This blockage altered deposition patterns between the northern Mississippi Embayment, in Illinois and Missouri, and the southern portion of the Mississippi Embayment.

By the late Paleozoic era, the tensional forces induced on the crustal material caused a failure between the Ozark Uplift, Nashville Dome, and the connecting arch. Sediment began to escape the northern portion of the embayment and trickle its way south once again. The increased sediment load in conjunction with the high-density emplaced material allowed isostatic subsidence to reinitiate (See Figure 2-2d).

Towards early and middle Mesozoic time, a period of dormancy prevailed. Erosional patterns deposited vast amounts of material west onto the Great Plains and south towards the Gulf of Mexico (Ervin and McGinnis, 1975). Despite the regional

quiescence, the North American Craton and the South American/African craton were continuing to shift apart. This gradual shifting caused significant subsidence of the Gulf Coastal Plain which lied between them. The subsiding Gulf Coastal Plain developed tension within the embayment region and reactivated the ancient rift lying underneath it (see Figure 2-2e; Yungul, 1971). In addition to reactivating the rift, the downward drag of the subsiding Gulf Coast Plate initiated concurrent subsidence near the southern end of the embayment (see Figure 2-2f). Gradually, the subsiding regions extended to the north and west.

The rate of subsidence within the Mississippi embayment has continually diminished as the region approaches a state of equilibrium.

2.1.1.2 Influence of New Madrid Rift Complex. The NMRC, based on gravity and aeromagnetic studies, resides almost directly below the region known as the New Madrid Seismic Zone (NMSZ; Braile et al. 1986). The NMSZ encompasses a northeasterly trending area, centered on New Madrid Missouri, which is the most seismically active region east of the Rockies (Doyle and Rogers, 2005; the earthquake trend in Figure 2-1 illustrates the NMSZ). Since the NMRC contains the only known tectonic features within the NMSZ, several theories have been derived to associate the rift network to the seismic activity experienced within the region. Only a few anomalous events exist outside the rift zones.

Two of the most popular theories, if used in conjunction, are: the plane of weakness model and the local basement inhomogeneity model (Braile et al., 1986). The plane of weakness model assumes that the graben fractures associated with the ancient rifting processes have left planes of weakness within the rifts. These weak planes

combine with a nearly East-West compressional stress (the current stress state in North America; Doyle and Rogers, 2005 and Braile et al., 1986) to invoke a seismic event. The strength of this model is attributed to the consistent failure mechanism between observed events and the model calculations. If the Northeasterly trending Reelfoot Rift were exposed to an East-West compression, the result would be a right-lateral strike-slip failure mechanism, similar to recorded events. The local basement inhomogeneity model compliments the plane of weakness model by providing an explanation for the few earthquakes that do not directly coincide with the rift network. In this model, the redistribution of stresses within weak portions of the rock mass initiates the earthquake activity near the extremities of the NMSZ.

Regardless of whether or not the NMRC dictates seismic activity throughout the region, it has directly governed the geologic setting within the NMSZ. The subsidence associated with the rifting process has channeled the major river systems directly into the created valley. Since at least early Mesozoic time, the lower Mississippi River has braided or meandered down the same course depositing vast quantities of sediment within the Reelfoot region (Braile et al., 1986; this time frame is coincident with the break-up of the Pascola Arch). Centuries upon centuries of sedimentation accumulated to create the Mississippi Embayment. Even Pleistocene glacial melt navigated its way down the river network and contributed to the stratification of soil within the embayment.

2.2. CURRENT GEOLOGIC SETTING

The current geologic setting within the NMSZ is dominated by the characteristics of the Mississippi Embayment, an arm of the Gulf Coast Plain that extends up the

Mississippi River Valley (an approximate outline is shown in Figure 2-1). The embayment is comprised of a down warped syncline, a structural trough, embedded in Paleozoic rock that extends from the Gulf of Mexico to the southern portions of Missouri and Illinois (Hashash and Park, 2001). The trough is filled with unconsolidated to poorly consolidated sediment from the Mesozoic and Cenozoic eras (Grohskopf, 1955 and Kolata et al., 1980). The surficial exposure of the sediment follows a broad plain that slopes gradually to the south, but the subsurface resembles a wedge of sediment that thickens southward. Regions in the northern cusp of the embayment host an erosional featheredge of the sedimentary soil, and southern regions, like Mississippi and Arkansas have over 4000 feet of unconsolidated sediment (Kolata et al., 1980).

Due to the consistent mode of deposition within the embayment area, the soil stratigraphy maintains a relatively ubiquitous horizontal distribution throughout the region. As the wedge of sediment gradually thickens, the thickness of each stratum within the wedge increases. In the vertical direction, the presence of distinct strata is the product of variances in depositional patterns throughout time. Therefore, it is advantageous to associate each stratum with a particular system in the geologic time scale. (It should be noted that the period marked by a continuous Pascola Arch experienced isolated depositional patterns between the northern and southern portions of the embayment. The remainder of this discussion addresses conditions found in the northern Mississippi Embayment.)

The basement rock material is predominantly of the Paleozoic era and consists of varying layers of dolomite, sandstone, limestone, chert, and shale (Grohskopf, 1955 and Kolata, 1980). The unconsolidated sediments that fill the trough are the product of

Mesozoic and Cenozoic depositional activity with the oldest soil conforming to the basement rock. Table 2-1 provides a chronological geologic sequence of the major soil strata, and the paragraphs that follow will introduce the general soil descriptions and isolate the soil formations associated with each geologic time frame, starting from basement rock.

Table 2-1: Chronological Sequence of Major Soil Strata (based on Kolata, 1980)

Era	System	Series	Formation	Strata Description
Cenozoic	Quaternary	Holocene		alluvium, colluvium, and lacustrine deposits
		Pleistocene		uniform loess
	Tertiary	Pliocene	Mounds Gravel	sub-angular chert gravel in a matrix of clayey quartz sand
		Eocene	Wilcox	fine to coarse, micaceous sand with lenses of fine gravel and beds of clay
		Paleocene	Porter's Creek	dark clay
			Clayton	glauconitic sand and clay
Mesozoic	Cretaceous	Gulfian	Owl Creek	silty clay with fine to coarse sand
			McNairy	clayey quartz sand
				clayey silt
				clayey quartz sand
			Tuscaloosa	rounded chert gravel
Paleozoic	Pre-Cretaceous	Pre-Gulfian	Bedrock	varying layers of: dolomite, sandstone, limestone, chert and shale

The oldest soil layers are associated with the Gulfian series of the Cretaceous system in the Mesozoic era. The base layer, or Tuscaloosa formation, is comprised of well rounded chert gravel and varies in thickness, depending on the contour of the basement rock. The McNairy formation overlays the Tuscaloosa formation with three distinct layers, two layers of fine, clayey quartz sand that sandwich a layer of clayey silt.

The Owl Creek Formation, silty clay with fine to coarse grained sand, follows the McNairy formation (Kolata, 1980).

Into the Tertiary system and Quaternary system of the Cenozoic era, a greater number of distinct depositional patterns can be observed. The time of the Paleocene series brought glauconitic sand and clay (marine deposits) of the Clayton formation with a cap of dark clay from the Porters Creek formation (Grohskopf, 1955). Throughout the Eocene series, fine to coarse, micaceous sand with lenses of fine gravel and beds of clay up to six feet thick were deposited to create the Wilcox formation. Then, the Pliocene series carried sediment from the southern Appalachians and Lake Superior region to deposit sub-angular chert gravel within a matrix of clayey quartz sand (Kolata, 1980). Finally, the Pleistocene series of the Quaternary system covered the region with a blanket of uniform loess, and in recent time, the flood plains and river valleys continue to collect alluvium, colluvium, and lacustrine deposits.

The presence of the Mississippi Embayment introduces many difficulties for civil engineering design. The great depth of unconsolidated settlement causes serious seismic design issues for structures with a medium to long period. The large difference between the shear wave velocity of the unconsolidated sediments and the basement Paleozoic rock creates an impedance contrast that is conducive to ground motion transformations. As the wave propagates from the fault to the surface, it must pass through the boundary between rock and soil. When the wave hits the unconsolidated soil, it has a tendency to amplify the ground motion. Increased ground motion amplitudes in saturated granular materials results in an elevated risk of liquefaction and its associated phenomena (e.g. lateral spreading). Another analytical difficulty associated with the embayment and the

practice of dynamic soil mechanics is the incoherence between the vertical and lateral propagation patterns within the stratigraphy of the sediment layers. However, the meager slope of the embayment trough (20 to 30 ft/mi) allows a one-dimensional analysis to be conducted in a free-field condition (Hashash and Park, 2001).

2.3. LOCAL SEISMICITY

Throughout the winter of 1811 and 1812, the NMSZ hosted a sequence of earthquakes with no comparison anywhere in the world (Johnston and Schweig, 1996). Within eight weeks, three earthquakes, each with moment magnitudes of approximately 8.0, shook the entire populated United States. The lateral extent of ground shaking induced by these events surpasses any other earthquake within the contiguous United States (McKeown, 1982). Interspersed between and trailing these great earthquakes were 203 damaging aftershocks (Nuttli, 1982). From that time until 1982, twenty damaging earthquakes ($M_w \approx 4.0$-6.5) were emitted from the same seismic zone (Nuttli, 1982).

Since the installation of accelerographs in 1974, over 3000 small earthquakes ($M_w < 5.0$) have been detected within the NMSZ, but no record of an earthquake series comparable to the 1811-1812 sequence has been recorded (Johnston and Schweig, 1996). However, paleoseismic studies conducted in the region have discovered evidence of at least two previous comparable earthquake sequences in the NMSZ. According to Tuttle et al. (2002), sequences similar to the 1811-1812 earthquakes occurred around 1450 AD, 900 AD, and some time before 800 AD (this series has a poorly constrained date). Based on their studies, Tuttle et al. (2002), suggested a recurrence interval of approximately 500+/-300 years, but they stated, "There is no reason to assume a constant earthquake

recurrence rate anywhere and certainly not in intra-plate regions like the NMSZ, where the tectonic driving forces are not understood."

Despite the uncertain time frame, it is safe to assume that another sequence of large earthquakes will strike the NMSZ eventually and the implications associated with such a series of events would be catastrophic. It was suggested by Obermeier (1988) that a recurrence of the 1811-1812 earthquakes would result in: an impassable interstate system between Cairo, IL and Memphis, TN, damaged bridges due to lateral spreading or stream bed collapse, and severe flooding due to an upsurge of agitated ground water.

2.4. PALEOSEISMOLOGY

Paleoseismology consists of studying various earthquake features that remain preserved in a geologic record in order to predict fault rupture and ground shaking (Tuttle, 2001). In situations where faults are not manifested on the surface or the historic record for the region is younger than the anticipated recurrence interval, paleoseismology allows the investigator to determine approximate dates, sizes, and locations of past earthquakes. The NMSZ has been a prime candidate for paleoseismic studies, because it lacks surficial manifestations of faulting and the historic record is an order of magnitude less than the anticipated recurrence interval.

The primary earthquake features utilized in the evaluation of pre-historic earthquakes is the presence of liquefaction-induced ground failures (Tuttle, 2001 and Obermeier et al., 2005). Sand blows, dikes and sills created by liquefaction-induced failures are generally preserved within a soil stratigraphy, and the level of ground shaking required to induce such features can be easily back-calculated, except on liquefaction-

induced slope failures (Obermeier et al., 2005). For that reason, liquefaction-induced failures that occur on nearly flat ground (i.e. hydraulic fracturing, lateral spreading, and ground oscillations) dominate the current body of knowledge associated with paleoseismology.

Estimating the age of a pre-historic earthquake incorporates a combination of radiocarbon dating, pedology, soil stratigraphy, and emplaced archeological artifacts (Obermeier, 2005). The most popular method is radiocarbon dating coupled with a stratigraphic analysis (Tuttle, 2001). In this method, the material directly above the sand blow provides a minimum date of intrusion; the material below the sand blow provides a maximum date of intrusion; and material within the sand blow can be construed as contemporaneous with the intrusion. By incorporating this method to several locations throughout a large area, the window of uncertainty for each event can be diminished.

Determining the magnitude and epicentral location of a pre-historic earthquake is typically performed congruently by analyzing a vast region of liquefaction-induced failures (ideally this area would exhaust the extent of failures). For each individual feature, an estimate of the ground shaking necessary to induce the observed dimensions based on the liquefaction potential of that site is determined. Once the ground shaking intensity at each site is estimated, a distance verse magnitude relationship is applied to approximate the epicentral location and magnitude associated with the earthquake (Tuttle, 2001).

In the NMSZ, a synthesis of paleoseismic studies was compiled by Tuttle et al. (2002) which incorporated nearly 250 individual sites. The age estimates for these studies consisted of radiocarbon dating of charcoal and plant remains within the

stratigraphy near the documented sand blows, as well as an archeological analysis of Native American artifacts that remained within the stratigraphy. This study expanded a previous investigation that identified liquefaction features as far as 200 km to the northeast, 240 km to the northwest, and 250 km to the south of New Madrid, MO (Tuttle, 2001).

The most interesting facet of the study was the composition of the sand blow structures. Like most sand blows, there was a fining upward trend which insinuates a loss of energy associated with the dissipation of excess pore pressure as the event progresses. However, there were several layers of fining upward lifts divided by thin silt layers (indicative of periods of quiescence between lifts), and each layer had a similar thickness. The presence of this compound structure indicates that the sand blows were the product of several, closely-spaced, similar-sized earthquakes (Tuttle et al., 2002).

2.5. LIQUEFACTION / LATERAL SPREADING SUSCEPTIBILITY

As illustrated from paleoseismic studies conducted in the region, liquefaction-induced failures are ubiquitous throughout a majority of the NMSZ. Within the meizoseismal area, hydraulic fracturing is the dominant manifestation of liquefaction-induced failures, but at greater distances lateral spreading phenomena are more prevalent due to the mechanisms associated with each failure (Obermeier et al., 2005).

2.5.1. Influencing Factors. There are many factors that influence the inception of liquefaction, and several more that control the failure mechanism and surface manifestations. As discussed in chapter three, liquefaction is induced by an increase in pore pressure beyond the confining stress which results from the soil skeletons tendency

to shift during cyclic shearing. Therefore, any property that contributes to the elevated pore pressure, the confining pressure within the soil, or the soils ability to withstand shear stress has an influence over its susceptibility to liquefy. In particular, relative density, grain size distribution, depth to liquefiable layer, depth to water table, and age of the sediment are the primary factors that influence liquefaction susceptibility (Obermeier et al., 2005).

The failure mechanism, on the other hand, proves slightly more ambiguous. Since hydraulic fracturing requires a tensile rupture of the cap material, the thickness of the liquefiable layer is the primary contributor (Obermeier et al., 2005). A thick liquefiable layer promotes more dramatic increases in pore pressure and an elevated volume of expelled water that is available to penetrate the cap. For lateral spreading to occur, the geometry must lack lateral restraint by the presence of a gradual slope or an open face (see chapter three for details). In the case of surface oscillation where the ground moves back and forth to form dikes, the tendency of the cap material to promote surface waves controls ground failure (Obermeier et al., 2005).

2.5.2. Historical Studies. The efforts expended towards identifying the source, magnitude and recurrence interval of the 1811-1812 earthquake series through paleoseismic studies have resulted in numerous accounts of liquefaction studies within the NMSZ. For a detailed synopsis, the interested reader should investigate Obermeier (1988), Johnston and Schweig (1996), Tuttle (2001), Tuttle et al. (2002), and Obermeier et al. (2005).

The literature addressing lateral spreading in the NMSZ is much sparser. Doyle and Rogers (2005) developed a method to analyze topographical anomalies near

Crowley's Ridge, on the western portion of the NMSZ. Crowley's Ridge is the most prominent geologic feature within the NMSZ, and its sloping banks host several instances of slope failures. The methodology developed by Doyle and Rogers (2005) utilizes aerial photography and topographical maps to identify possible locations of historic slope failures. Throughout their research in developing the graphical identification method, they discovered that the only instance of reported lateral spreading east of the Rockies was presented in a paper by Fuller (1912), in which he discussed fissures along the Chickasaw Bluffs east of the Mississippi River.

3. LATERAL SPREADING

3.1. THE CATALYST – LIQUEFACTION

Liquefaction is one of the most prolific forms of seismic failure in geotechnical engineering, but the concept was first acknowledged prior to realizing the capacity for seismic induction of it. Arthur Casagrandre addressed the impact of static or monotonic liquefaction in his 1936 paper on the stability of earth fills, nearly thirty years before the inspirational events of 1964. As discussed in chapter one, 1964 brought vigorous attention to seismic liquefaction failures, and by 1969 multiple authors had attempted to coalesce the available data into theory, e.g. Ambraseys and Sarma (1969) and Castro (1969). Eventually, empirical models, like the one developed by Seed (1979), sprang up for use in engineering practice.

Liquefaction is the result of increased pore-water pressure due to seismic shear waves penetrating the soil profile. As the seismic shear waves propagate through the soil, cyclic shear stresses are induced onto the soil structure, and cyclic shear strains begin to accumulate. If the soil consists of loose sand, it will experience contractive behavior which reduces the pore volume. Below the water table, the voids within the soil structure are filled with incompressible fluid, so the soil's tendency to contract against the incompressible water will produce an increase in pore pressure. Once the pore-pressure reaches the confining pressure, the soil has an effective stress of zero, which compromises the shear strength of the soil and it liquefies.

3.2. MECHANISM OF FAILURE

One of the most damaging manifestations of liquefaction is lateral spreading. In this form of liquefaction failure, large blocks of intact, non-liquefiable soil float along the surface of a liquefied soil layer. Any structure founded on, or through, these floating blocks experiences significant lateral forces from the dislocating soil mass. Other failures associated with liquefaction include: ground oscillation and flow failure. Ground oscillations are marked by successive opening and closing of fissures within the ground, and flow failures consist of large sections of flowing land.

Research has determined that the local topography strongly influences the type of liquefaction failure that develops (Obermeier, 1988). For lateral spreading to occur, either a free-face or a mild ground slope (<5%) must exist at the site. If the site consists of level ground without a free-face, the anticipated failure would be ground oscillations, but sites with a slope steeper than about 5% generally induce a flow failure. The free-face, e.g. trench, ditch or river, provides no lateral confinement to resist the soil movement, so the anticipated ground oscillations produce large lateral deformation towards the free-face. If there is no free-face, but a gradual slope exists, smaller deformations may be anticipated in the down-slope direction. As the distance from the free-face increases, the influence of the free-face diminishes until the deformation is controlled by the slope of the ground, instead of the free-face. Figure 3-1 illustrates a schematic of a lateral spread with increased deformation close to the river, or free-face.

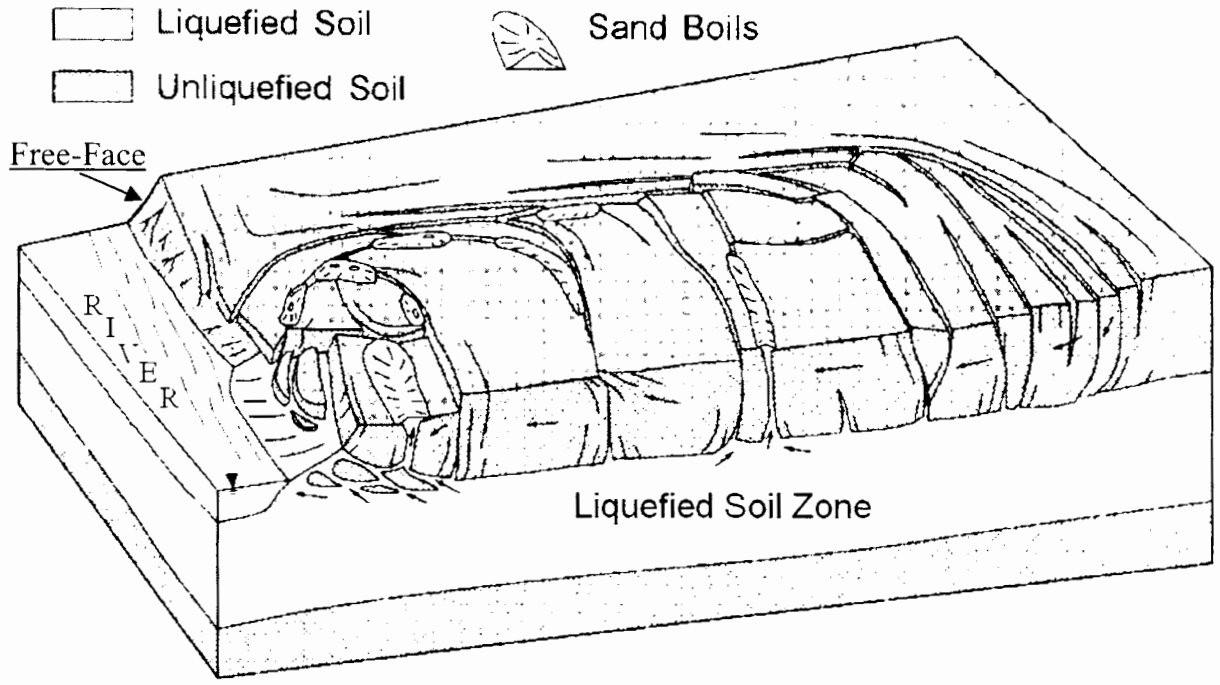

Figures 3-1: Schematic of Lateral Spreading Soil Damage during Liquefaction (modified from Rauch and Martin, 2000)

Another contributing factor to liquefaction-induced lateral spreading is hydraulic fracturing. The high pore-pressures in the liquefied sub-layer escape through weaknesses in the non-liquefiable cap material which separates the intact layer into blocks. Sand is ejected from between the cracks and sand boils develop, as seen in Figure 3-1.

3.3. DEVELOPMENT OF PREDICTIVE MODELS

Initial attempts to estimate lateral spreading displacements incorporated existing seismic slope stability analysis, i.e. Newmark (1965) sliding-block analysis. Unfortunately, the difficulty in defining precise post-liquefaction shear strength, combined with the low shear stresses associated with the mild slopes, limited the capacity for these techniques to model lateral spreading phenomena.

Due to these challenges, researchers began formulating empirical models calibrated from available earthquake records. Statistically based sensitivity studies were applied to the data sets in order to determine the parameters with the highest influence on lateral spreading displacements, and equations were fit to the data based on these factors. Hamada et al. (1986) presented the first empirical model to estimate lateral spreading displacements, and new models continue to become available as more earthquake data is collected.

With the emergence of computers, the ability to conduct complex numerical analysis in a realistic time-frame came to fruition. Researchers in geotechnical engineering have developed numerical models to simulate liquefaction-induced lateral spreading, but the difficulty in formulating appropriate constitutive soil models remains a challenge.

3.3.1. Empirical/Statistical Models. Empirical models are probably the most utilized lateral spreading analysis methods in today's engineering practice. They are easy to use and provide reasonable estimations (within a factor of two) considering our current capacity for defining soil parameters. Recent models are quite sophisticated compared to the initial model by Hamada et al. (1986), who only evaluated the impact of the liquefied thickness and the local ground slope. Current models have identified up to nine different variables that influence the extent of lateral spreading.

The study conducted for this thesis utilized two distinct empirical models, i.e. Rauch and Martin (2000) and Youd et al. (2002). Since California and Japan experience the most frequent seismic activity, both of these empirical models are calibrated for these regions.

3.3.1.1 Rauch and Martin (2000) EPOLLS Lateral Spreading Model. The Rauch and Martin empirical prediction of liquefaction-induced lateral spreading (EPOLLS) model incorporates three levels of sophistication. Each one requires progressively more information about the site being evaluated in order to determine the estimated displacement (D_H). The most basic equation represents the regional-EPOLLS (R-EPOLLS) model (eq. 3.1), which only requires information from the seismologic source.

$$D_H = (0.613M_w - 0.139R_f - 2.42A_{max} - 0.0114T_d - 2.21)^2 + 0.149 \quad (3.1)$$

By adding information regarding the topography and geometry, the Site-EPOLLS (S-EPOLLS) model (eq. 3.2) provides a more refined estimate of anticipated lateral

$$D_H = (0.613M_w - 0.139R_f - 2.42A_{max} - 0.0114T_d + 0.000523L_{slide} + 0.0423S_{top} + 0.01313H_{face} - 2.44)^2 + 0.111 \quad (3.2)$$

displacements, but the geotechnical-EPOLLS (G-EPOLLS) model is their most advanced. In the G-EPOLLS (eq. 3.3), nine variables that incorporate geotechnical subsurface data, topography, geometry, and seismology all contribute to defining the extent of lateral spreading.

$$D_H = (0.613M_w - 0.139R_f - 2.42A_{max} - 0.0114T_d + 0.000523L_{slide} + 0.0423S_{top} + 0.01313H_{face} + 0.0506Z_{FSmin} - 0.0861Z_{liq} - 2.49)^2 + 0.124 \quad (3.3)$$

The definitions of parameters and the limits provided by Rauch and Martin (2000) are given in Table 3-1.

Table 3-1: Limits and Descriptions for each variable in the EPOLLS model

Variables that influence lateral spreading evaluation			Minimum	Maximum
Regional	M_w	Earthquake magnitude	6.5	9.2
	R_f (km)	Distance from vertical projection of fault	0	119
	A_{max} (g)	Peak amplitude of horizontal acceleration	0.16	0.52
	T_d (s)	Duration of shaking with A>0.05g	4	88
Site	L_{slide} (m)	Max. horizontal length of lateral spread	20	1360
	S_{top} (%)	Slope of surface topography	-0.7	5.2
	H_{face} (m)	Height of free-face exposure	0	9
Geotech	Z_{FSmin} (m)	Depth to minimum factor of safety	2.4	12.4
	Z_{liq} (m)	Depth to the top of the liquefied layer	0.9	7.3

Due to the nature of the equation development, limits must be applied to many of the variables. For all empirical models, the extent of their capability is controlled by the range of recorded earthquakes and lateral spreading data that was incorporated into the linear regression of the model.

3.3.1.2 Youd et al. (2002) Lateral Spreading Model. The Youd et al. (2002) model is a revision of the previous Bartlett and Youd (1992, 1995) models that have been used in practice for over a decade. Due to their prolonged exposure, these models have gained popularity in the engineering community and will continue to see use until a drastic change in the approach to evaluating lateral spreading is available.

In this empirical model, it is assumed that one of two conditions controls the maximum displacement, free-face or ground slope, and that there is a transitional zone where the influence of the free-face becomes less significant than the ground slope. In

the transitional zone, both equations are evaluated and the largest estimated displacement (D_H) is assumed to control. Figure 3-2 illustrates a schematic of the ranges provided by Youd et al. (2002) for determining the appropriate condition.

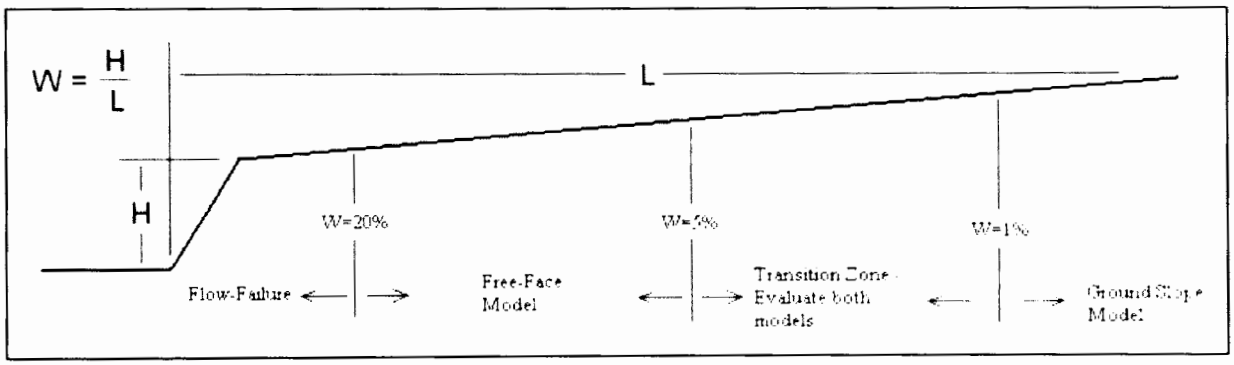

Figure 3-2: Schematic of appropriate model conditions (after Youd et al., 2002)

The equations for the free-face condition (eq. 3.4) and the ground slope condition (eq. 3.5) are quite similar, but they are considered independently. If the ground slope condition is evaluated, there is no free-face accounted for. If the free-face condition is evaluated, there is no way to account for the slope. However, by utilizing the suggested approach of evaluating both conditions in the transition zone, the most influential condition can be determined and utilized for the estimate.

$$\log(D_H) = -16.713 + 1.532M_w - 1.406\log(R^*) - 0.012R_f + 0.593\log(W) + 0.540\log(T_{15}) + 3.413\log(100 - F_{15}) - 0.795\log(D_{50} + 0.1) \quad (3.4)$$

$$\log(D_H) = -16.213 + 1.532M_w - 1.406\log(R^*) - 0.012R_f + 0.338\log(S) + 0.540\log(T_{15}) + 3.413\log(100 - F_{15}) - 0.795\log(D_{50} + 0.1) \quad (3.5)$$

This model is also based off of a data set containing a limited range of variables. Table 3-2 provides definitions and suggests limiting values for the variables, as provided by Youd et al. (2002).

Table 3-2: Limits of Variables for the Youd et al. (2002) Lateral Spreading Model

Variables that influence lateral spreading evaluation		Minimum	Maximum
D_H (m)	Estimated horizontal displacement	0.1 m	6 m
M_w	Earthquake moment magnitude	6	8
R_f (km)	Closest Distance to vertical projection of fault	0.5 km	
H (m)	Height of free-face exposure	Limits are provided by W (%), seen below	
L (m)	Distance from free-face		
W (%)	Ratio of free-face height (H) to Distance (L) = H/L*100	1%	20%
T_{15} (m)	Cumulative thickness of soil with $(N_1)_{60}$<15	1 m	15 m
F_{15} (%)	Average fines content of T_{15}	Combination should plot within bounds on Figure 3-3, below	
$(D_{50})15$ (mm)	Mean grain size for liquefiable (N<15) layer		
S (%)	Slope of the surface topography being analyzed	0.1%	6%
Z_T	Depth to top of liquefied layer	1 m	10 m

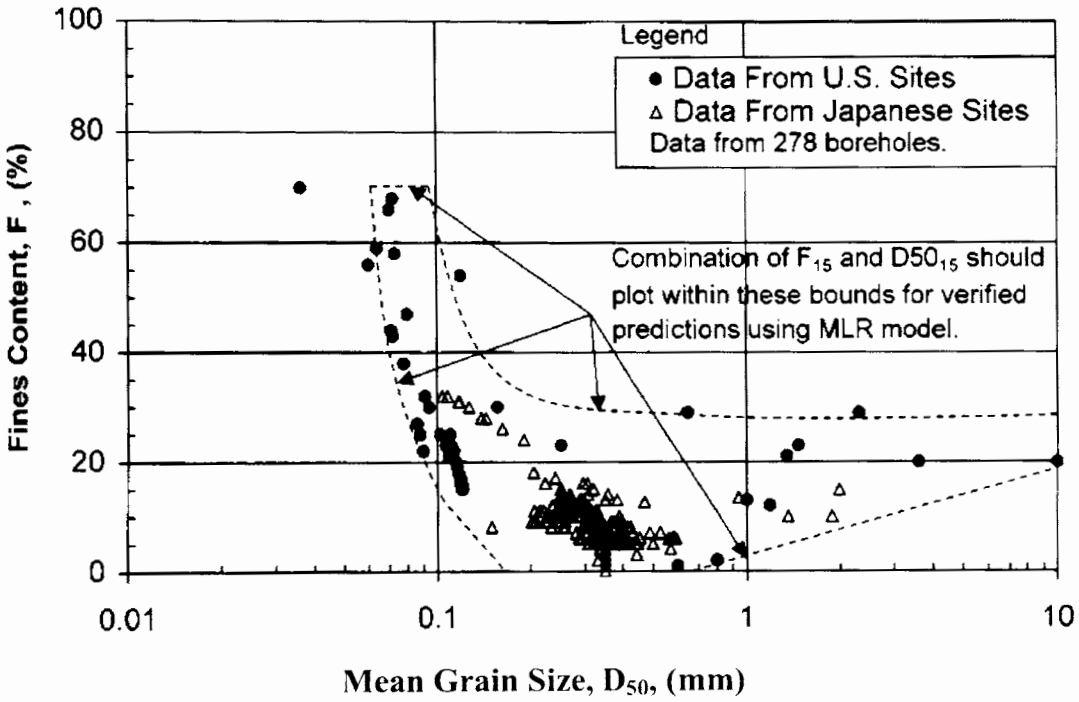

Figure 3-3: Range of Mean Grain Size and Fines Content for Evaluating Youd et al. (2002) Model

3.3.2. Shear Strain Potential Lateral Spreading Model. Since the introduction of lateral spreading theories, researchers have attempted to develop laboratory testing regimes to simulate the soil's response during seismic loading (see Seed et al., 1985 and Kuwano and Ishihara, 1988). These attempts were restricted in their applicability, because of the difficulties associated with sampling loose sand. Instead, reconstituted samples were utilized to determine trends in the cyclic response of clean sands. To incorporate these laboratory tests into contemporary practice, in-situ test correlations and laboratory test results fused to developed integrated lateral spreading models based on the shear strain potential of the soil.

The shear strain potential methods correlate standard penetration test (SPT) results or cone penetration test (CPT) results into a "clean sand equivalent" relative density. The corrected relative density correlates to a maximum cyclic shear strain based

on the compilation of laboratory tests. By integrating the maximum shear strains with depth, a lateral displacement index (LDI) is determined. The LDI represents the maximum possible deformation of the soil profile. For a more reasonable estimation, the LDI is usually calibrated by empirical methods to approximate the anticipated maximum deformation. Calibrations provided by Shamoto et al. (1998), Tokimatsu and Asaka (1998), and Zhang et al. (2004) utilize geometric considerations to calibrate the LDI, while Faris et al. (2006) utilize the static shear stress ratio and the earthquake magnitude to calibrate the LDI. The shear strain potential model evaluated in this thesis was developed by Zhang et al. (2004) and modified by Idriss and Boulanger (2008).

3.3.2.1 Zhang et al. (2004) Model. The Zhang et al. (2004) model is the most current geometrically-based shear strain potential approach for estimating lateral spreading displacement. They developed a five step method that correlates the factor of safety against liquefaction, in-situ test data, and laboratory test results to the maximum displacement of laterally spreading soil. Prior to evaluating this model, the factor of safety against liquefaction (FS_{liq}) must be determined to a depth that encompasses all soil layers with a factor of safety against liquefaction less than two. Once the factor of safety against liquefaction is calculated, CPT or SPT data is converted to an equivalent clean sand value (methods described in Youd et al. 2001), which is used to determine the relative density (D_r) of the soil. For the relative density conversion, the authors used a modified form of Meyerhof (1957) for SPT correlations and Tatsuoka et al. (1990) for CPT correlations, as shown in equation 3.6 and 3.7, respectively.

$$D_r = 14\sqrt{(N_1)_{60cs}} \qquad \text{for: } (N_1)_{60cs} \leq 42 \tag{3.6}$$

$$D_r = -85 + 76\log(q_{c1Ncs}) \qquad \text{for: } q_{c1Ncs} \leq 200 \text{ kPa} \tag{3.7}$$

With the relative densities and factor of safety against liquefaction established, Figure 3-4 can be used to interpolate the maximum cyclic shear strain's (γ_{max}) by plotting the factor of safety against liquefaction on the abscissa, moving up the plot to the appropriate relative density, and sliding left to the value of the maximum cyclic shear strain on the ordinate. For this model, "[the maximum cyclic shear strain] refers to the maximum amplitude of cyclic shear strains that are induced during cyclic loading for a saturated sandy soil without biased static shear stresses in the directions of the cyclic loading" (Zhang et al., 2004). Biased in-situ static shear stresses are generally induced by the local ground geometry, which is present at laterally spreading sites.

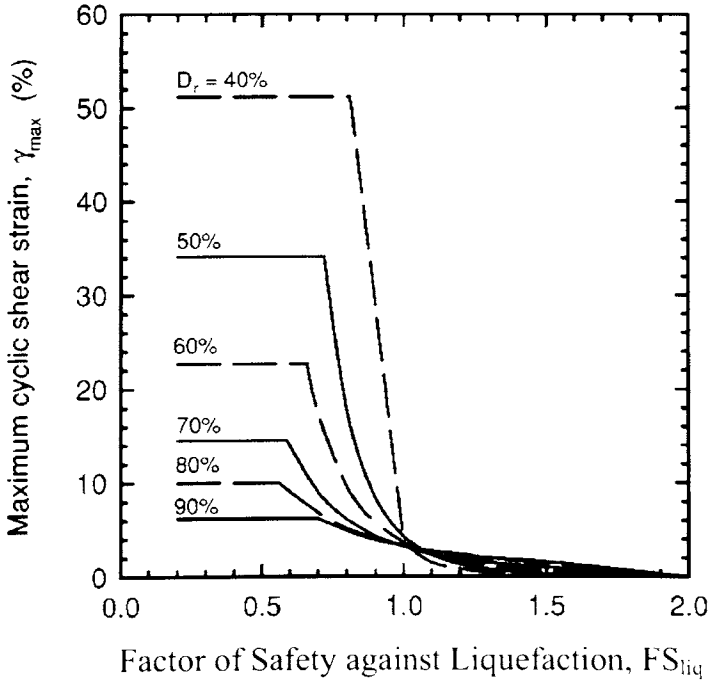

Figure 3-4: Plot for determining maximum cyclic shear strain (based on Ishihara and Yoshimine, 1992, and Seed, 1979)

Once the maximum cyclic shear strain is determined, it is integrated to a soil depth (Z_{max}) that contains all soil layers with a factor of safety against liquefaction less than two, as in equation 3.8.

$$LDI = \int_0^{Z_{max}} \gamma_{max}\, dz \tag{3.8}$$

At this point, an LDI has been determined based on correlations to laboratory tests, however the LDI represents a maximum possible deformation. Therefore, empirical calibration of the LDI must be conducted to account for local site geometry and topography. Similar to Youd et al. (2002), this method specifies either a free-face (eq. 3.9) or a ground slope (eq. 3.10) model to determine the anticipated maximum lateral displacement (LD).

$$LD = LDI\left[6\left(\frac{L}{H}\right)^{0.8}\right] \tag{3.9}$$

$$LD = LDI(S + 0.2) \tag{3.10}$$

Since this model is calibrated by a data set of real earthquakes, limitations apply to the calibration method. These limitations are shown in Table 3-3.

Table 3-3: Limits of Variables for Zhang et al. (2004) Lateral Spreading Model

Variables with specified limits		Minimum	Maximum
M_w	Earthquake moment magnitude	6.4	9.2
A_{max} (g)	Maximumum induced acceleration	0.19	0.6
H (m)	Height of free-face exposure	0	18

Idriss and Boulanger (2008) modified the Zhang et al. (2004) model for use with a spreadsheet evaluation and eliminated the necessity to interpolate a plot by incorporating fitted equations. In addition, the provided equations eliminate the need to calculate

relative density. A conversion to the clean sand value is still necessary, but the clean sand values can be used directly in the equations.

After completing a liquefaction analysis and correcting the in-situ values for fines content, the first step in the Idriss and Boulanger (2008) approach is to determine the limiting cyclic shear strain (γ_{lim}) by one of three methods: SPT, CPT, or relative density (eqs. 3.11, 3.12, 3.13, respectively). Notice that if this value is determined from a single borehole, the maximum applied value should be no greater than 50%.

$$\gamma_{lim} = 1.859\left(1.1 - \sqrt{\frac{(N_1)_{60cs}}{46}}\right)^3 \geq 0 \tag{3.11}$$

$$\gamma_{lim} = 1.859\left(2.163 - 0.478(q_{ciNcs})^{0.264}\right)^3 \geq 0 \tag{3.12}$$

$$\gamma_{lim} = 1.859(1.1 - D_r)^3 \geq 0 \tag{3.13}$$

The next step is to determine the alpha-factor (F_α) which is utilized to determine the maximum cyclic shear strain. The alpha-factor can also be determined by any one of the three mentioned in-situ tests. The alpha-factor equations for SPT, CPT, and relative density are eqns: 3.14, 3.15, and 3.16, respectively.

$$F_\alpha = 0.032 + 0.69\sqrt{(N_1)_{60cs}} - 0.13(N_1)_{60cs} \qquad [(N_1)_{60cs} \geq 7] \tag{3.14}$$

$$F_\alpha = -11.74 + 8.34(q_{1Ncs})^{0.264} - 1.371(q_{1Ncs})^{0.528} \qquad [q_{1Ncs} \geq 69 \text{ kPa}] \tag{3.15}$$

$$F_\alpha = 0.032 + 4.7D_r - 6.0(D_r)^2 \tag{3.16}$$

Once the factor of safety against liquefaction, the limiting cyclic shear strain and the alpha-factor are calculated, the maximum cyclic shear strain can be evaluated.

Depending on the relationship between FS_{liq} and F_α, one of the following three equations (eqns 3.17, 3.18, or 3.19) is used to determine the maximum cyclic shear strain.

$$\gamma_{max} = 0 \qquad \text{if, } FS_{liq} \geq 2.0 \qquad (3.17)$$

$$\gamma_{max} = \min\left[\gamma_{lim}, 0.035(2 - FS_{liq})\left(\frac{1 - F_\alpha}{FS_{liq} - F_\alpha}\right)\right] \qquad \text{if, } 2 > FS_{liq} > F_\alpha \qquad (3.18)$$

$$\gamma_{max} = \gamma_{lim} \qquad \text{if, } FS_{liq} \leq F_\alpha \qquad (3.19)$$

The remainder of the lateral spreading evaluation is identical to the Zhang et al. (2004) model. The maximum cyclic shear strain is integrated using equation 3.8 in order to determine an LDI. Since Idriss and Boulanger (2008) did not provide calibration equations for estimating maximum lateral displacement, the calibration implemented by Zhang et al. (2004), with equations 3.9 and 3.10, can be utilized as specified in section 3.3.2.1 of this thesis.

3.3.3. Mechanistic Lateral Spreading Models. Mechanistic models utilize a knowledge of the physics and the estimated failure mechanism to develop equations that describe the physical reactions within the soil mass. For lateral spreading, mechanistic models have been attempted in the form of Newmark sliding-block analysis, but the low levels of shear stress associated with shallow slopes and the sensitivity of the model to post-liquefaction, or residual, shear strengths has hindered its widespread utilization (Idriss and Boulanger, 2008). However, several recent models have been developed to estimate lateral displacement by the sliding-block method, e.g. Baziar et al. (1992) and Olson and Johnson (2008). The primary focus of these papers was directed towards determining the residual shear strength of liquefied soils. As the ability to model this strength progresses,

the accuracy of these models will increase. Eventually, this may be a viable option for evaluating liquefaction-induced lateral spreading.

3.3.4. Numerical Models. Numerical models utilize the fast processing speeds of computers to solve large systems of equations simultaneously. These equations combine to develop matrix based partial differential equations (PDE's) that incorporate mass, damping, and spring constants to simulate the response of the soil. Until the advent of the computer, this technique was too computationally demanding to be practical, but recent attempts have been made to model lateral spreading displacements by numerical techniques. In general, the finite element method (FEM) or finite difference method (FDM) are used to model lateral spreading numerically. These two methods utilize similar equations to model the deformation, but they solve the PDE's differently. The FDM derives the answer by solving discrete time steps, while the FEM uses an integration approach to obtain a "weak answer". For geotechnical applications, the distinction has little impact on the associated limitations.

In both the FEM and FDM, the structure (soil, in this case) is disctretized into elements with nodes at each corner. The nodes are shared by the adjacent elements, and the PDE's are solved by forcing compatibility at every node. As the elements distort towards large strains (as required in lateral spreading), some of the elements may collapse upon themselves creating an incompatibility. In addition to the strain limitations associated with the elements, large strains are difficult to simulate by constitutive soil models, because the soil behaves non-linearly at large strain levels.

Despite the difficulties associated with modeling large strain, the critical limitation for applying numerical techniques towards a Midwest lateral spreading

estimation corresponds to recorded acceleration strong ground time histories. Once the model is calibrated with the appropriate constitutive soil model, an accurate acceleration time history for the desired earthquake must be applied to the base. In the Midwest, only synthetic ground motions are available for analysis, so the results are controlled by the quality of the synthetic time history.

The techniques described in items 3.3.3 and 3.3.4 are beyond the scope of this thesis, considering the incompatibility and availability of quality data to conduct the analysis. Therefore, these methods will not be utilized in the sensitivity analysis or the Midwest bridge site evaluation (presented in chapter four).

4. APPLICATION OF LATERAL SPREADING MODELS

4.1. SELECTION OF APPLICABLE MODELS

Based on a preliminary assessment of each of these models, broad categories were developed to address the general techniques and assumptions used for estimating lateral spreading displacements, e.g. empirical, mechanical, or numerical, as outlined in chapter three. Conveniently, the technique used to develop the model strongly dictated the data necessary to complete the evaluation, so feasibility studies were conducted on general categories instead of individual models.

The feasibility study consisted of compiling a list of data that could be obtained from a standard geotechnical investigation (Table 4-1) and a list of necessary data for each technique (Table 4-2). The limitations associated with seismological records in the Midwest were also addressed. Based on a comparison of these lists, the models with data requirements not met were eliminated. Primarily, the eliminated models required acceleration strong ground motion time histories, which are not available in the Midwest (only synthetics).

Table 4-1: Obtainable Information for Midwest Sites

Obtainable Items	
Seismologic	M_w - Earthquake Magnitude
	R_f - Distance to fault
	A_{max} - Maximum ground acceleration (estimated)
	T_d - Duration of ground motion (estimated)
Topography/Geometry	S - Slope of ground surface
	H_f - Height of free-face
	L - Distance from toe of free-face
Subsurface	SPT - Standard penetration test
	CPT - Cone penetration test
	FC - Fines Content of soil
	D_{50} - Mean grain size of soil

Table 4-2: Data Requirements List for Various Lateral Spreading Models

Model	Required Items	
Empirical	Seismologic	M_w - Earthquake Magnitude
		R_f - Distance to fault
		A_{max} - Maximum ground acceleration
		T_d - Duration of ground motion
	Topography/Geometry	S - Slope of ground surface
		H_f - Height of free-face
		L – Distance from toe of free-face
	Subsurface	SPT - Standard penetration test
		FC - Fines Content of soil
		D_{50} - Mean grain size of soil
Shear Strain Potential	Topography/Geometry	S - Slope of ground surface
		H_f - Height of free-face
		L – Distance from toe of free-face
	Subsurface	SPT - Standard penetration test
		-or-
		CPT - Cone penetration test
		FC - Fines Content of soil
Mechanistic	Seismologic	Acceleration time history
	Topography/Geometry	Full Site Profile with subsurface stratigraphy
	Subsurface	SPT - Standard penetration test
		-or-
		CPT - Cone penetration test
		Residual strength of liquefied soil
		D_w - Depth to water table
Numerical	Seismologic	Acceleration time history
	Topography/Geometry	Full Site Profile with subsurface stratigraphy
	Subsurface	SPT - Standard penetration test
		-or-
		CPT - Cone penetration test
		Residual strength of liquefied soil
		D_w - Depth to water table
	Peripheral	Constitutive Soil Models
		Specialized Computer Program

Within each subset of feasible lateral spreading models, the particular requirements were assessed. For the empirical models, two distinct approaches were discovered. A majority of the models, like Youd et al. (2002), were compiled from

multiple lateral spreads in a single area. Therefore, the evaluation produces an estimate of lateral spreading displacement at a specific location along the sloping ground. The EPOLLS model, on the other hand, evaluated the average lateral spreading displacement within an entire region of deformation, so the evaluation only produces an average deformation. Since the Youd et al. (2002) model is the most popular and the EPOLLS model is the only average method, these were the models chosen to represent the subset of empirical models.

The only other evaluation technique that was considered appropriate for a Midwest study was the shear strain potential method, which incorporates laboratory data with in-situ tests and empirical calibration. This technique is relatively new, so there are few variations. Zhang et al. (2004) developed the most current shear strain potential method to utilize a geometrically based calibration similar to the existing empirical models, so this method was incorporated into the analysis. In addition to the Zhang et al. (2004) model, a modification of their method proposed by Idriss and Boulanger (2008) was analyzed.

4.2. DEVELOPMENT OF ANALYSIS METHODOLOGY

To expedite calculations, a spreadsheet incorporating each of the selected models was developed and verified against hand calculations. Based on an assessment of the required data and the treatment of that data, the models were arranged on a single spreadsheet separated by tabs. The complexity of the models increases from left to right following a chronological order and level of complexity. An instructions document and the spreadsheet are included in the Appendix of this thesis.

4.3. EVALUATION PROCESS

Since the evaluation process is slightly different for each model, some of them can estimate preliminary lateral spreading displacements at earlier stages than others (e.g. the R-EPOLLS and S-EPOLLS, described in section 3.3.1.1 of this thesis). However, the following process was developed to conduct and compare all the models simultaneously.

Prior to any lateral spreading investigation, the seismic parameters and subsurface data must be acquired for the site of interest, and the liquefaction potential must be evaluated. This ensures that lateral spreading is capable of occurring. Once it is determined that liquefaction will occur, the topography and geometry of the site should be measured to identify and quantify the ground slope and free-face height. Based on the above data, a lateral spreading calculation can be conducted using the prepared spreadsheet.

4.4. SENSITIVITY ANALYSIS

The only variables shared by all the empirical correlations are ground slope and free-face height, but the relative impact of these are not well understood. Therefore, a sensitivity analysis was conducted to determine the influence of ground slope grades and free-face height within each model. According to Saltelli et al. (1999), "a sensitivity analysis is the study of how the variation in the output of a mathematical model can be apportioned, qualitatively or quantitatively, to different sources of variation in the input of a model." To isolate the source of variation in the output, all the other variables were held constant while the input of interest was varied.

In order to prepare an analysis based on realistic variables, an actual site was chosen for the study, Cairo, IL. This site is host to two bridges (one built in the 1920's and one built in the 1950's). Since the author had already collected in-situ test data near this location during preliminary research, this site was selected for the sensitivity analysis.

4.4.1. Seismic Site Parameters. Based on the geographic location of this site, a deaggregation of the seismic hazards in the region was conducted using the United States Geological Survey (USGS) website. The deaggregation process, known as probabilistic hazard analysis, calculates the contribution of each seismic hazard within range of a particular location and develops statistically expected earthquake parameters resulting from all the seismic sources within range. The deaggregation produces the output illustrated in Figure 4-1.

The parameters of highest interest in Figure 4-1 are magnitude, acceleration, and source-to-site distance. However, the percent contribution of each hazard plays a pivotal role in determining the appropriateness of the results. In this figure, each column represents an individual seismic hazard, and the location within the plot indicates the distance and expected magnitude of that hazard. The height of the column represents the percent contribution of that hazard to the specified parameters. In this case, the M_w=7.7 earthquake at a distance of twelve kilometers was the primary contributor, and the anticipated acceleration at bedrock was 1.8g (located just below the geographic coordinates in the upper right corner of Figure 4-1).

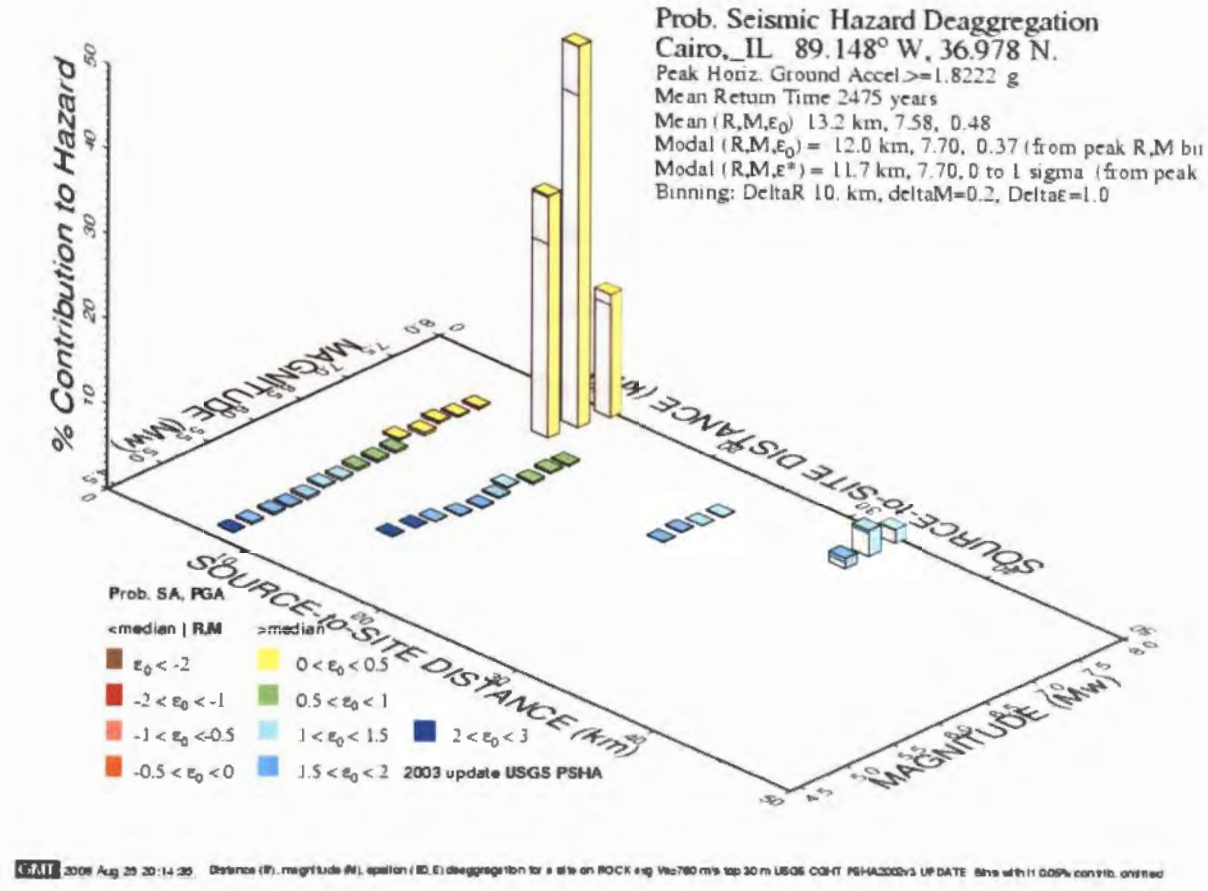

Figure 4-1: USGS Deaggregation for Cairo, IL (http://eqint.cr.usgs.gov/deaggint/2002/; conducted on 08/25/09)

Unfortunately, the anticipated accelerations were beyond the scope of every model, so attenuation relationships for the Midwest provided by Toro et al. (1997; equation 4-1) were used to back-calculate the largest earthquake that these models were capable of evaluating. The distance to the largest contributing fault (12 km) was taken from the deaggregation results, and the attenuation model specified an earthquake with a M_w=6.5 and a maximum acceleration of 0.41g.

$$\ln[PGA(g)] = 2.20 + 0.81(M_w - 6) - 1.27\ln(R_f) + 0.11\max(\ln\frac{R_f}{100}, 0) - 0.0021R_f \qquad (4\text{-}1)$$

The distance specified in the deaggregation process represents the closest horizontal distance to the ground projection of the fault, which is the requested value in the empirical models. However, the attenuation characteristics of the Midwest are distinct from the locations used to develop the empirical models, and the distance used in the empirical models is directly related to the attenuation characteristics of the region. Therefore, Youd et al. (2002) developed an equivalent distance conversion to compensate for unique attenuation environments. The conversion requires knowledge of anticipated acceleration and earthquake magnitude. With these values, Figure 4-2 can be utilized to determine an equivalent distance. In this case, the equivalent distance is approximately six kilometers.

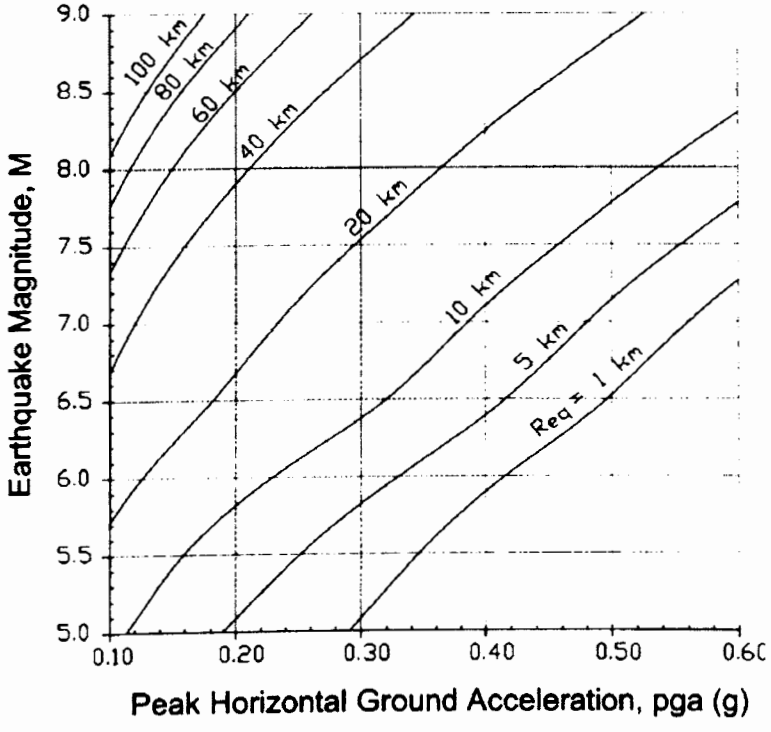

Figure 4-2: Equivalent Distance Plot (by Youd et al. (2002)

The additional required seismic data, i.e. earthquake duration, could not be calculated, so an assumed duration of 45 seconds was utilized in the analysis.

4.4.2. Site Subsurface Parameters. Several series of boreholes with SPT data were provided by Illinois Department of Transportation (IDOT) for the area north of Cairo, IL. At the Cairo interchange (where I-57 crosses Illinois route 51), eight boreholes collected in the year 2000 were provided, but this series contained no SPT data from fifteen to forty feet depth below the ground surface. To supplement this borehole data, two more series of boreholes from 1965 and 1966 provided forty-nine more boreholes with SPT data up to forty feet deep. The 1965 and 1966 series of boreholes were located nearly 4000 meters north of the Cairo interchange boreholes, but the top fifteen feet of soil corresponded fairly well. Therefore, a combination of the borehole data was used to define the subsurface conditions. The recorded N-values for every borehole analyzed versus elevation are provided in Figure 4-3. In this plot, a line labeled N=15 was placed to identify the N-value which the Youd et al. (2002) empirical model assumes is the threshold for liquefaction to occur.

Due to the different location and date between each borehole data set, a significant scatter was present. Therefore, an average N-value for each 2.5 feet interval was taken and plotted in Figure 4-4 with a shaded region identifying the range of possible values and an interpreted soil profile. The same N=15 line is displayed to illustrate the regions with a high potential for liquefaction.

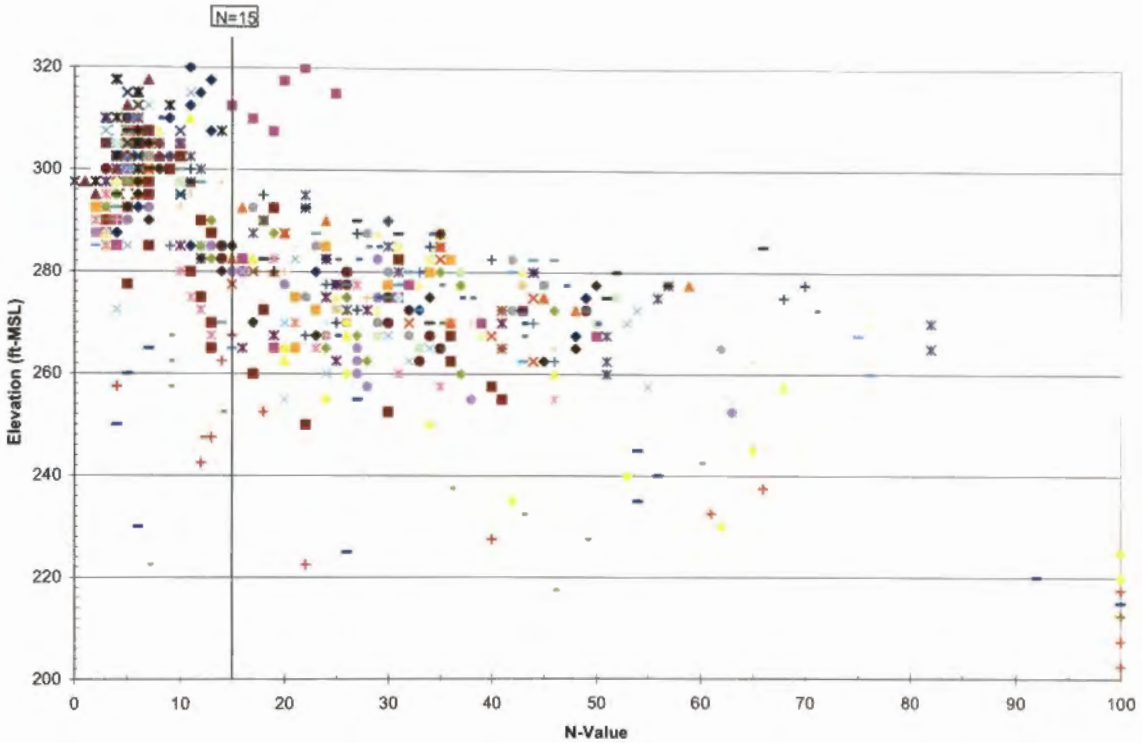

Figure 4-3: Compilation of N-values versus depth

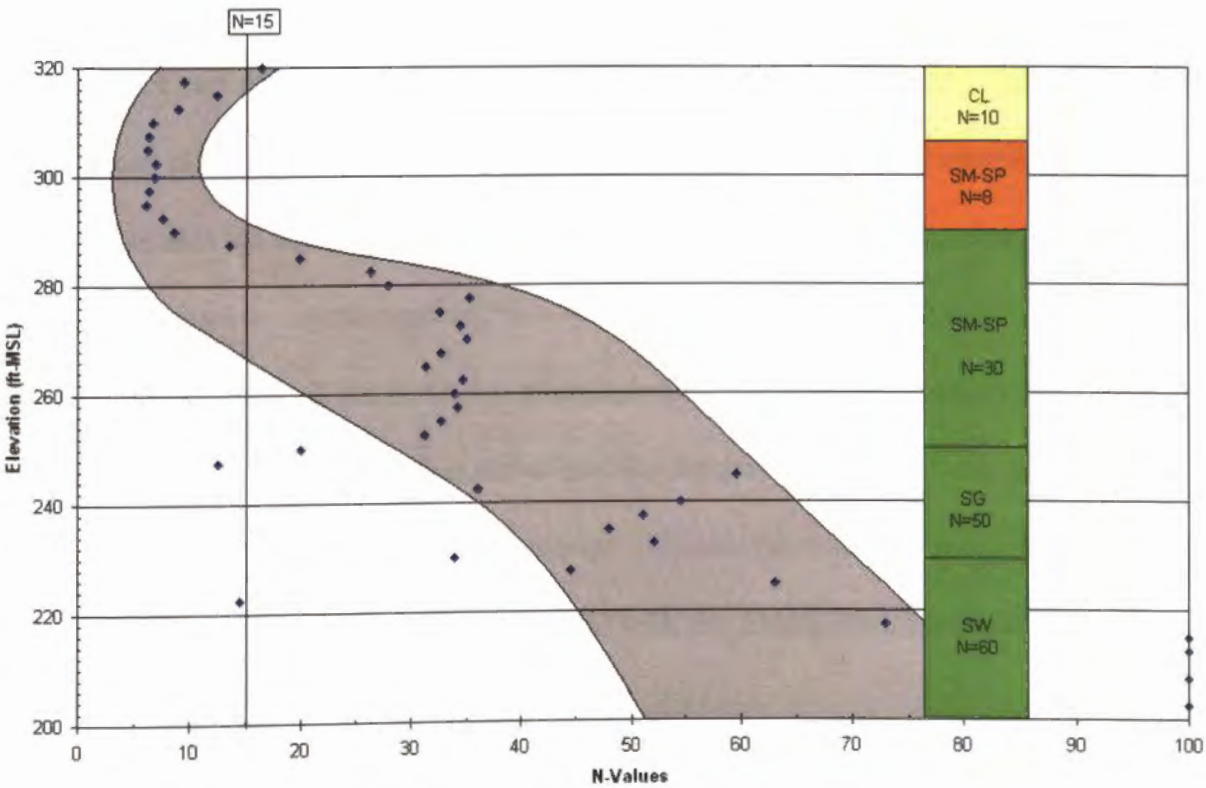

Figure 4-4: Average N-value verse elevation with idealized profile

4.4.3. Selection of Geometry and Topography. Since the focus of this sensitivity analysis was to address the impact of slope grades and free-face height, a majority of the geometry and topography was variable throughout the study. Slopes of 0%, 0.5%, and 2% were applied to profiles with free-face heights of 3m, 6m, and 9m to produce nine distinct results. The distance from the free-face was modeled in increments of 10 meters for the first 50 meters and increments of 50 meters up to 1000 meters.

The only deviation from this geometric application corresponds to the EPOLLS model, since this model uses different assumptions than the rest. The EPOLLS model takes an average displacement for the entire region, so the total length of the slide was the only distance applied. For this study, the largest applied distance (1000 meters) was used to evaluate the EPOLLS model.

4.4.4. Results of Sensitivity Analysis. In an effort to consolidate the results of the sensitivity analysis, plots were developed that contain only three curves, i.e. the G-EPOLLS, Youd et al. (2002), and the Idriss and Boulanger (2008) application of the shear strain potential model. Since all the EPOLLS models were developed from similar parameters and the shear strain potential models utilized the same calibration equations, their outputs were represented by two curves instead of five. The G-EPOLLS was selected to represent all the EPOLLS models, because it is the most sophisticated version of the EPOLLS evaluation. The Idriss and Boulanger (2008) approach was selected to represent the shear strain potential model, because it was the most current and it eliminated the interpolation errors associated with the Zhang et al. (2004) model.

The plots and associated discussion have been organized into sections that address the effects of free-face height on a single slope, while the effects of increasing slope are addressed through the progression of the sections.

4.4.4.1 Results of 0% Slope. The effects of free-face height are most pronounced near a location with negligible slope grades. However, even at a site with 0% slope, the ground slope model provided for the shear strain potential method managed to control the deformation at large distances from the free-face. This is due to the equation used for quantifying the deformation associated with slope gradation (LD=LDI*(S%+0.2)). The portion of the plots that are governed by the ground slope model can be identified by the horizontal portions of the shear strain potential and the Youd et al. (2002) model curves. On the other hand, the G-EPOLLS model maintains a horizontal line in all the plots. This is due to the single result produced by the EPOLLS models, not the presence of a ground slope model. Figures 4-6 to 4-8 illustrate the response of a site with 0% slope near a 3m, 6m, and 9m free-face, respectively.

As seen in Figures 4-6 to 4-8, the shear strain potential model experiences an estimate of constant deformation associated with the ground slope model. This flat portion initiates around 250 m from a free-face of 3m, Figure 4-6, and around 750 m from a free-face of 9m, Figure 4-8, which indicates that there is an increased distance of influence as the free-face increases.

The Youd et al. (2002) model was not influenced by the ground slope at any level of free-face height, so the curves present in Figures 4-6 to 4-8 represent the free-face model, solely. At great distances from the free-face, the Youd et al. (2002) model converges with the shear strain potential model (see 1000m mark in Figures 4-6 to 4-8).

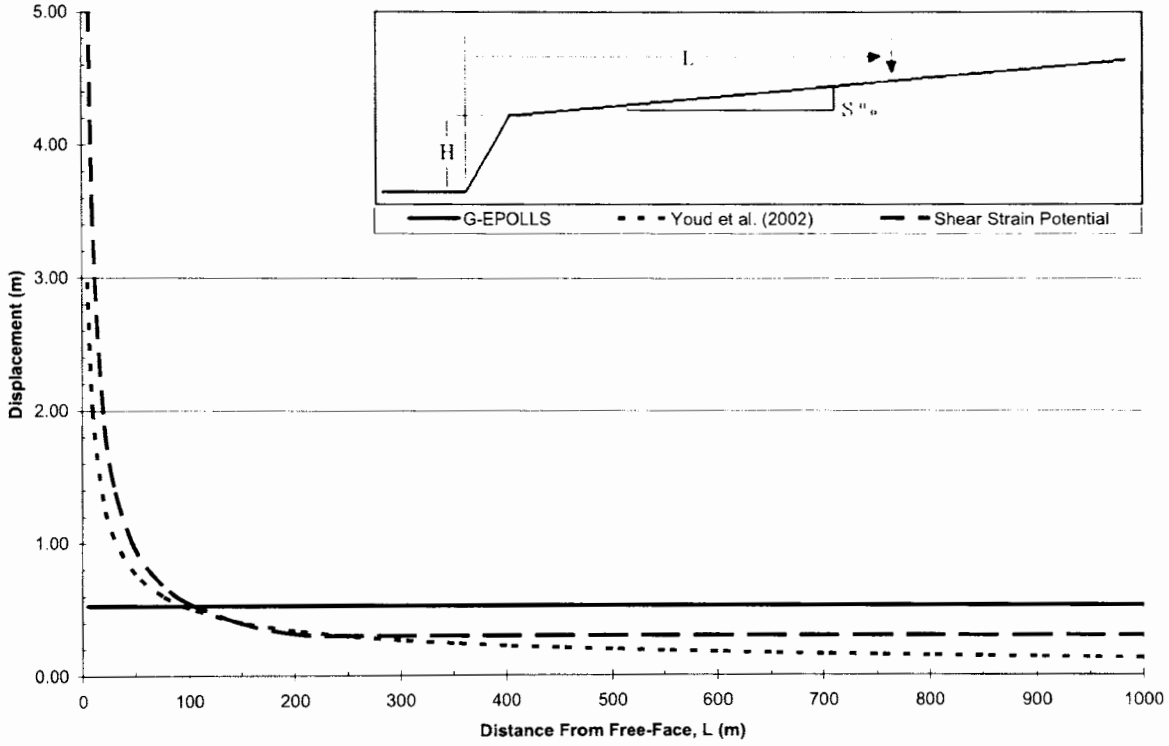

Figure 4-6: 3m Free-Face Height, H and 0% Slope, S

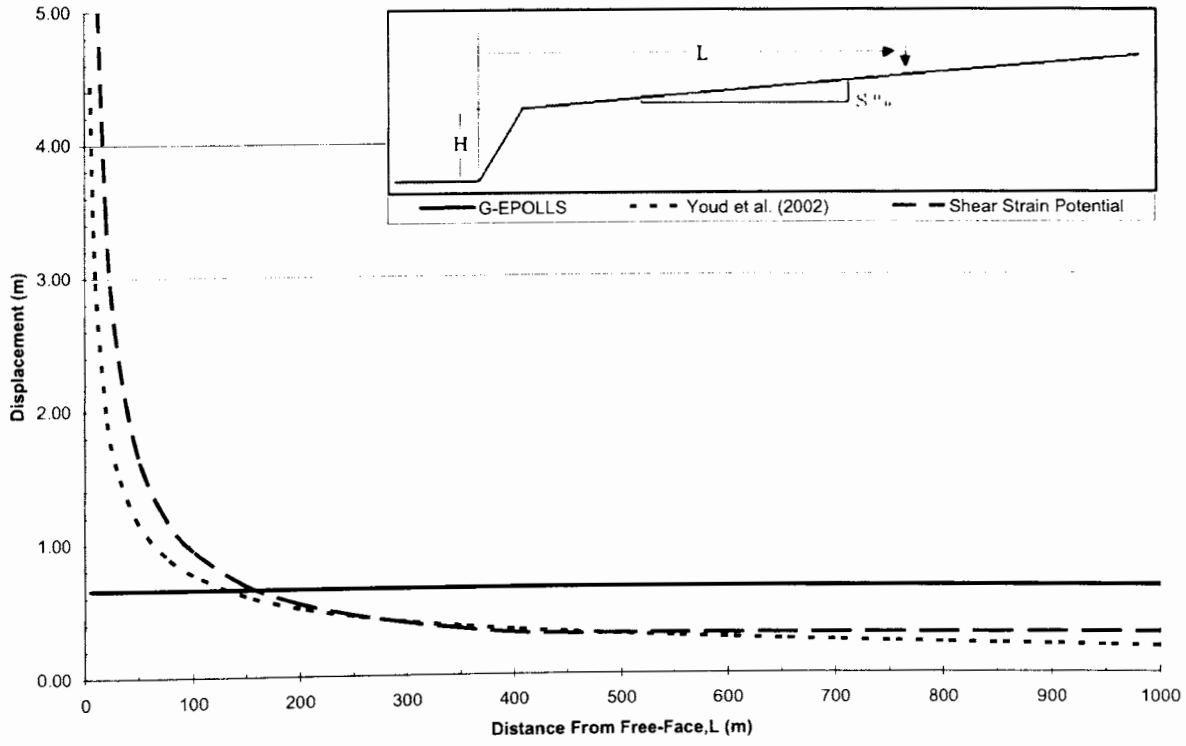

Figure 4-7: 6m Free-Face Height, H and 0% Slope, S

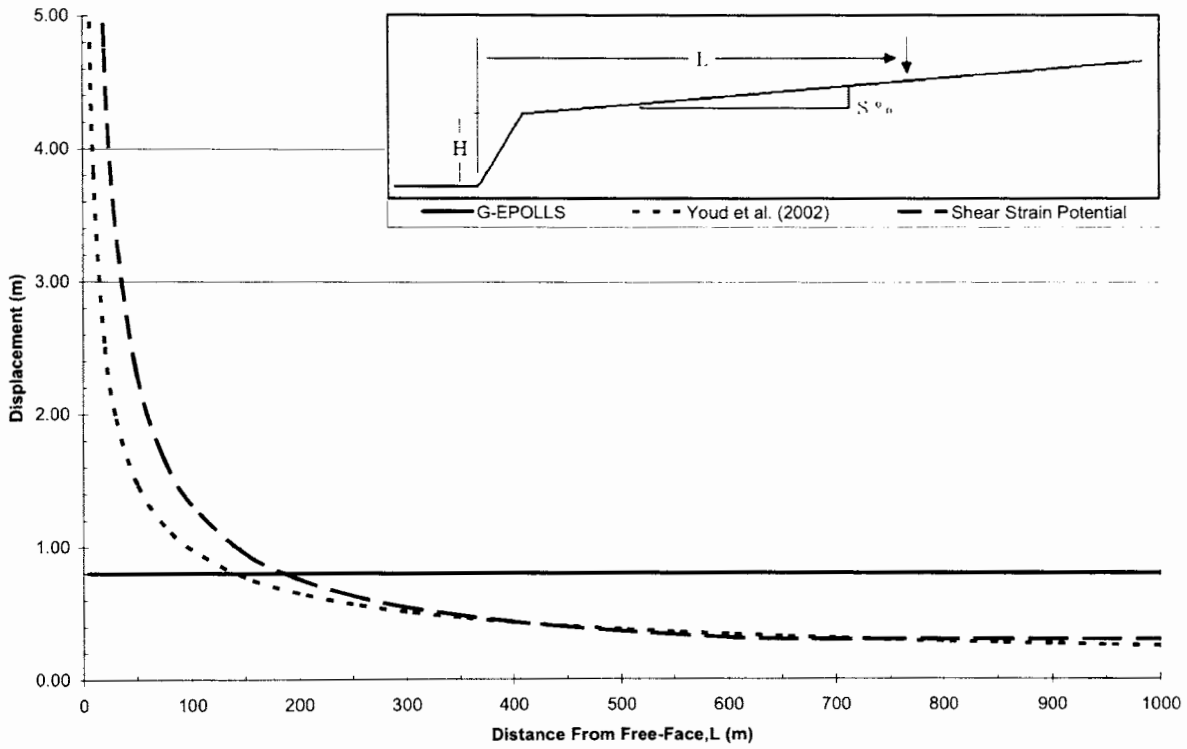

Figure 4-8: 9m Free-Face Height, H and 0% Slope, S

4.4.4.2 Results of 0.5% Slope. As expected, the application of a 0.5% slope resulted in an increase in anticipated lateral movement. Both the shear strain potential and Youd et al. (2002) models reach a constant value, which indicates the influence of the ground slope. In both of these models, the shear strain potential and the Youd et al. (2002), the ground slope controlled deformation remained constant despite the increases in free-face height, but the influence of the free-face extended farther distances from the free-face as its height increased, as seen in Figures 4-9 to 4-11. Despite the free-face height that was applied to the models, the Youd et al. (2002) model estimated a farther influence of the free-face height than the shear strain potential model, which may indicate a greater dependence on free-face height.

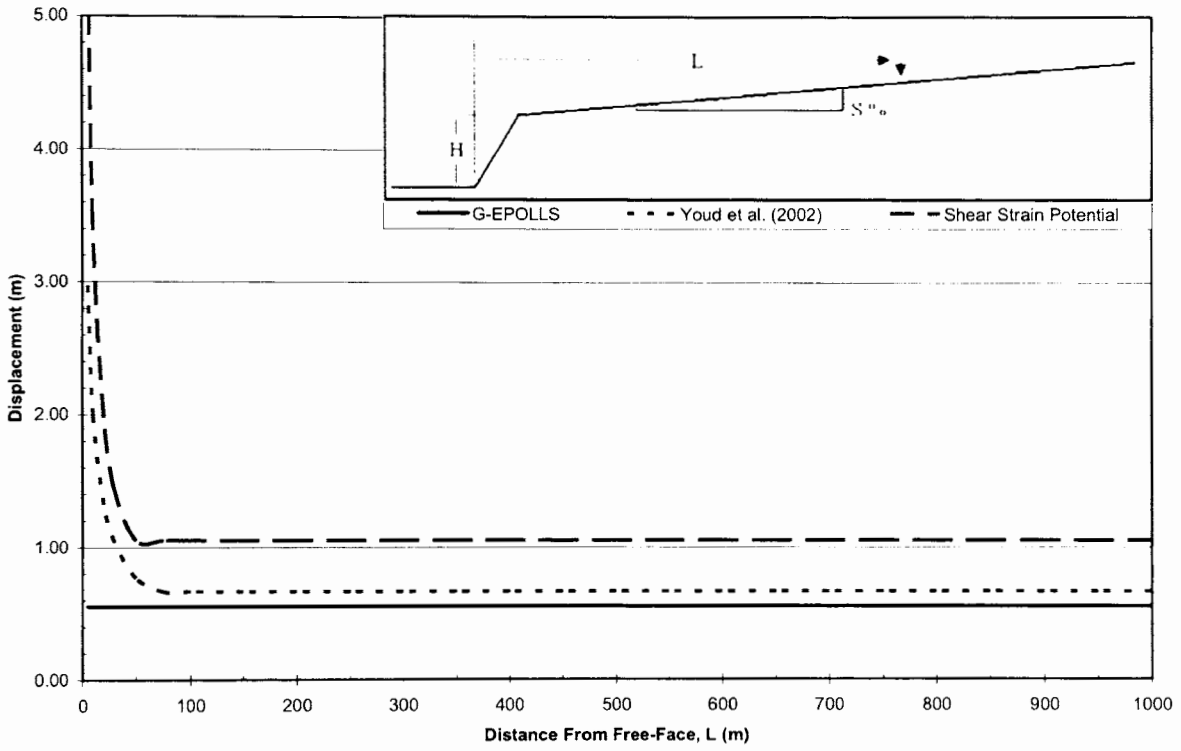

Figure 4-9: 3m Free-Face Height, H and 0.5% Slope, S

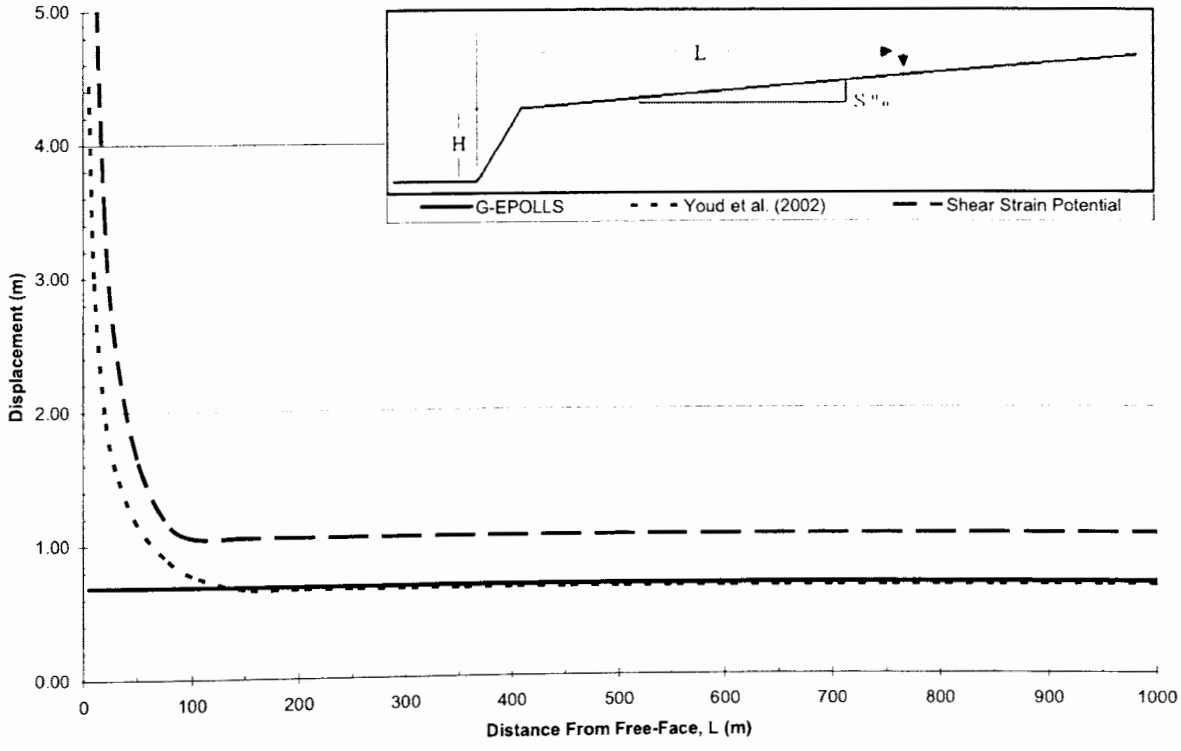

Figure 4-10: 6m Free-Face Height, H and 0.5% Slope, S

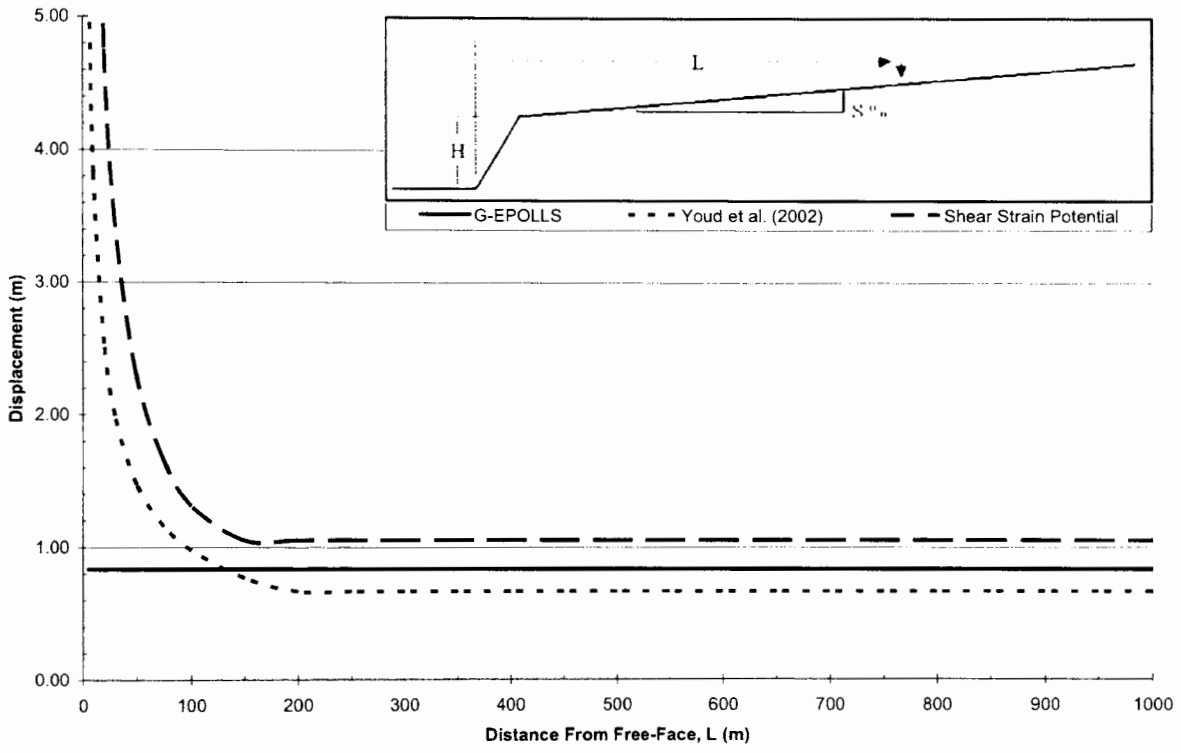

Figure 4-11: 9m Free-Face Height, H and 0.5% Slope, S

A comparison of the 3m, 6m, and 9m free-face heights near a 0.5% slope (Figures 4-9 to 4-11, respectively) against the corresponding plots for a 0% slope (Figures 4-6 to 4-8) indicates significant increases in the Youd et al. (2002) and the shear strain potential models with only slight increases in the EPOLLS model. The displacement estimated by the G-EPOLLS model was highly governed by the free-face height, but the presence of a slope had little effect. Since the EPOLLS model has no way of identifying the contribution of each case (ground slope or free-face), the relative increases must be examined. After application of a 0.5% slope, each free-face height evaluated produced an increased deformation estimate of less than 0.05m. However, the change in free-face height from 3m to 9m produced an increased estimate of nearly 0.3m. In addition, the presence of a 3m free-face resulted in the G-EPOLLS estimate being lower than the Youd

et al. (2002) estimate, but the presence of a 9m free-face produced larger estimates for the G-EPOLLS model than the Youd et al. (2002) model (see Figures 4-9 and 4-11).

4.4.4.3 Results of 2% Slope. When the slope was increased to 2%, every evaluation model experienced some level of increased lateral displacement. As seen in the plots for 3m, 6m, and 9m free-face heights near a 2% slope (Figures 4-12 to 4-14, respectively) compared to the previous plots for 0.5% slopes (Figures 4-9 to 4-11), the Youd et al. (2002) and shear strain potential models incurred large increases, while the G-EPOLLS model showed only mild increases.

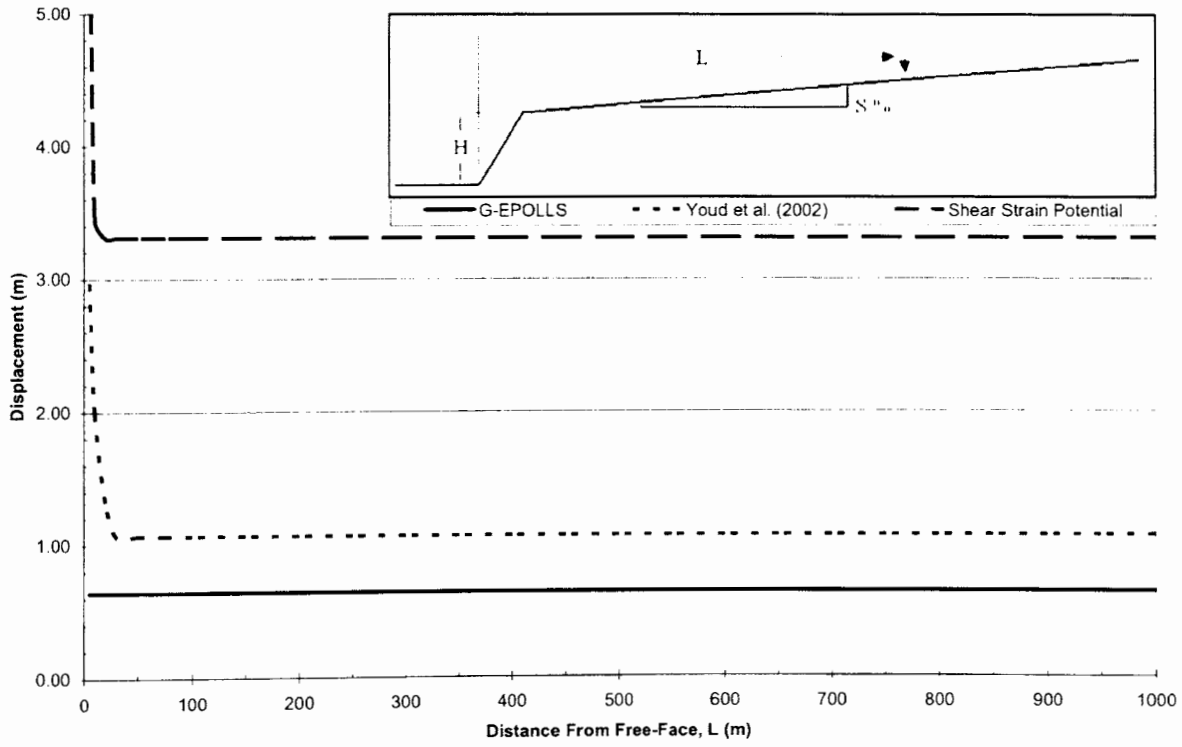

Figure 4-12: 3m Free-Face Height, H and 2% Slope, S

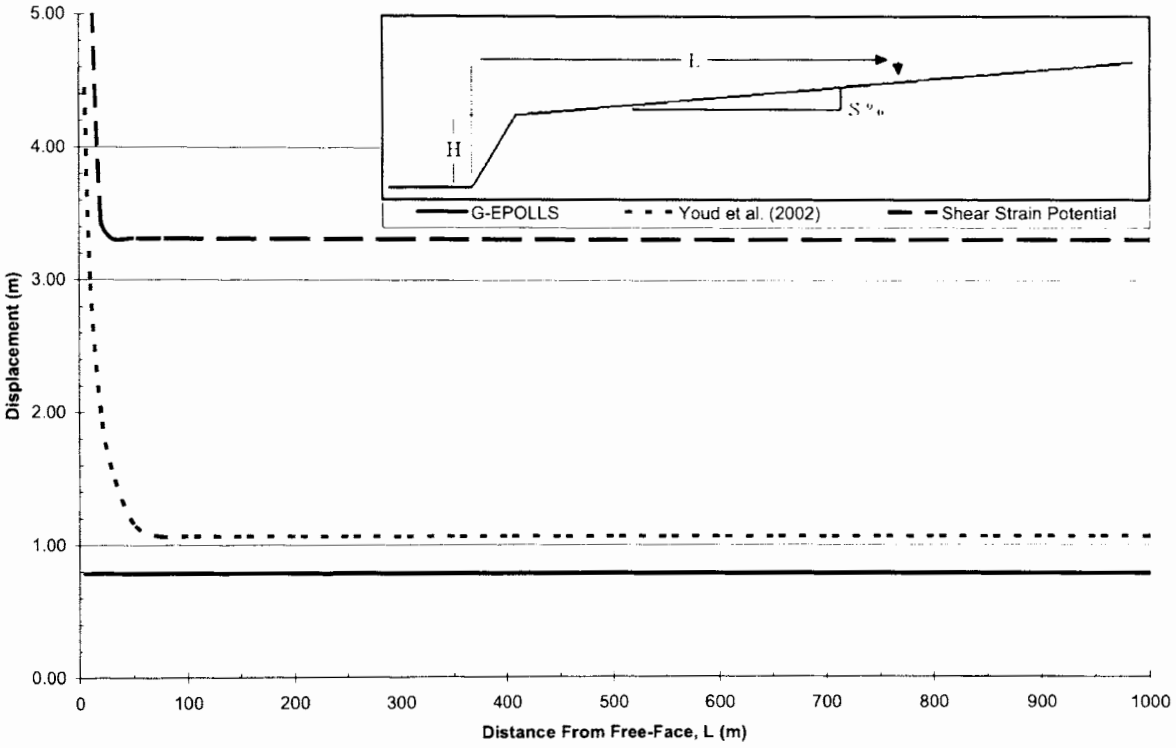

Figure 4-13: 6m Free-Face Height, H and 2% Slope, S

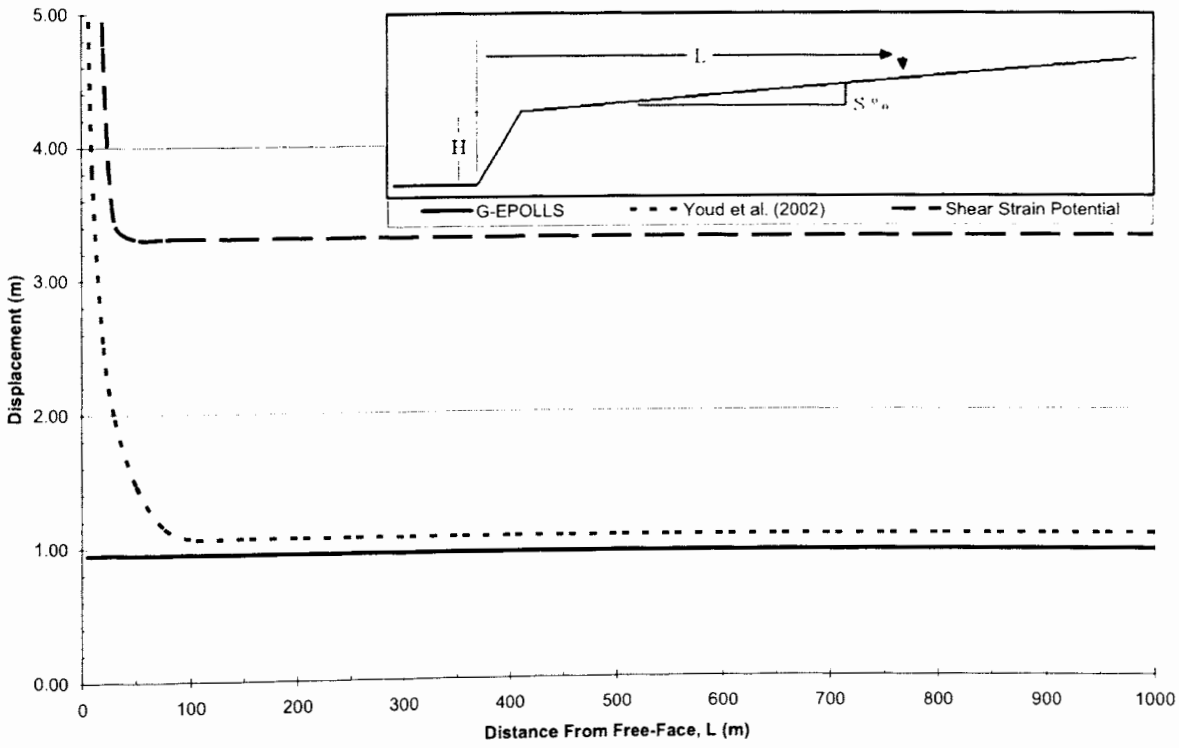

Figure 4-14: 9m Free-Face Height, H and 2% Slope, S

The results of the 2% slope analysis emphasized the high sensitivity of the Youd et al. (2002) and the shear strain potential models to increases in slope grade. Both the shear strain potential and Youd et al. (2002) models become predominantly controlled by the ground slope model (flat portion of the curve). At a 2% slope, the Youd et al. (2002) model estimates higher displacement than the G-EPOLLS, regardless of free-face height (see Figures 4-12 to 4-14); while at 0.5% slope, the G-EPOLLS estimated larger displacement with a 9m free-face. The G-EPOLLS model still produced larger increases due to free-face height than the Youd et al. (2002) or the shear strain potential models, which can be seen by the convergence of the EPOLLS and Youd et al. (2002) estimates at larger free-face heights in Figures 4-12 to 4-14. The most important aspect of this convergence corresponds to the continual increase of the G-EPOLLS model. Despite the estimated deformation associated with the ground slope, the EPOLLS model continues to feel the affects of the free-face. Unfortunately, the shear strain potential and Youd et al. (2002) models do not respond similarly.

4.4.5. Summary of Sensitivity Analysis. The results of the sensitivity analysis indicated that each lateral spreading model addresses the variation in local topography and geometry slightly different, and the relative magnitude of deformation associated with either a free-face or the ground slope was distinct in each model. The following relationships were found to be most influential:

- The Youd et al. (2002) and shear strain potential models were more sensitive to increases in ground slope, but the G-EPOLLS model was most susceptible to increases in free-face height.

- The shear strain potential model was the most sensitive to ground slope with ground slope deformation associated with even a 0% slope.
- The G-EPOLLS model continues to accrue deformation associated with the free-face height even when the slope is extremely high (other models do not).

4.5. BILL EMERSON MEMORIAL BRIDGE EVALUATION

The Bill Emerson Memorial Bridge (MO Bridge #: A-5076) has conveyed four lanes of traffic across the Mississippi River and connected MO Routes 74 and 34 in Cape Girardeau, MO to IL Route 146 in East Cape Girardeau, IL since December 13, 2003. The four-lane cable-stayed bridge spans 1150 feet of the river channel and approximately 2800 feet of Illinois flood plain. On the Missouri western bank, the bridge is planted into the shallow limestone bedrock with massive spread footings, but the Illinois approach rests on drilled shaft piers that penetrate over eighty feet of alluvial soil and socket into limestone (Hitt, 2001).

The fluvial deposition patterns of the Mississippi River flood plain produce varying layers of poorly sorted sand with sporadic silt and clay layers on top. These alluvial soil deposits are notoriously loose, and their close proximity to the river promotes elevated water tables. The loose structure combined with the elevated phreatic surface provides an increased risk of liquefaction susceptibility, and the presence of a non-liquefiable soil cap may produce a lateral spreading condition.

The most intriguing engineering aspect of the Bill Emerson Memorial Bridge is not the liquefiable foundation soils or the deep foundation elements. It is the presence of

an extensive seismic instrumentation array within the structure and around the structure. The monitoring system consists of 84 Kinemetrics EpiSensor accelerometers installed throughout the bridge structure and the adjacent free-field sites (Wang et al., 2007). These accelerometers were deployed to capture the response of the cable-stayed bridge, including translational, torsional, rocking, and translational soil-structure interactions.

The instrumentation within the adjacent soil deposits was emplaced to record free-field motions at the surface and within the soil stratigraphy in response to large ground motions. Each geotechnical array incorporated a MEMS-based (micro electrical mechanical system) ShapeAccelArray (SAA) from Measurand, Inc. and two strain gage piezometers from Geokon, Inc (Olson, 2008). The SAA is comprised of an array of rope like sensors that are placed into a casing to measure its deformation. The deformation is then correlated to horizontal and vertical acceleration data. The strain gage piezometers were placed at depths approximately 1/3 and 2/3 into the liquefiable soil layer to monitor increases in pore pressure.

The geotechnical monitoring system consists of three sets of these arrays. One set was adjacent to pier 8 (identified in Figure 4-16), which will represent the first measurement of soil-foundation-structure interaction in the Central United States (Olson, 2008). A second set of arrays was placed adjacent to the Illinois abutment to evaluate the soil remediation techniques that were used during its construction. A third set of arrays and piezometers was placed at a site to the east of the abutment in order to provide a metric for comparing the response of the remediated soil near the abutment to the existing in-situ soil conditions. Additional sensors are still being placed and replaced as flood waters recede.

4.5.1. Parameter Determination. There were many difficulties associated with the parameter selection process, and several assumptions were necessary to produce a lateral spreading estimate. The most problematic variables were: acceleration at the ground surface, expected magnitude of the earthquake, equivalent distance to the fault, fines content of the different soil layers, and mean grain size of the soil layers. The additional parameters of interest consisted of: length of the slide, slope of the ground surface, and SPT N-values of the different soil layers.

The soil variability at the site was summarized by two possible profiles, one with fine-grained cap material and one without. The three boring logs located in the vicinity of the analyzed slope were evaluated to determine the soil profile. Based on these boring logs, it was determined that approximately 90 ft of soil rests upon the limestone bedrock, and the bedrock had an elevation ranging from 240 ft to 245 ft. The groundwater level at the site is pragmatic due to the flux within the Mississippi River system, so the ground water table was assigned at the elevation of the mean river flow (el 320 ft). The following sub-sections detail the parameter determination process.

4.5.1.1 Seismic Site Parameters. As with any site in the NMSZ, the paucity of strong ground motion leads to a difficult interpretation of the ground motion necessary to induce liquefaction. Probabilistic hazard analysis methods, like the one available through the USGS website, produce estimates of maximum acceleration well beyond the capacity of the lateral spreading evaluation models (as discussed in section 4.4.1 of this thesis), and deterministic hazard analysis methods require detailed information about the fault, which is not available in this region.

Since the techniques used for estimating earthquake ground motions can not be directly applied, the maximum acceleration used in the Missouri Department of Transportation (MoDOT) bridge design, 0.36g, was selected to maintain consistency with the original design (Hitt, 2001). Based on this acceleration and the Midwest attenuation model developed by Toro et al. (1997), an earthquake moment magnitude of M_w=6.7 was determined. In addition to the acceleration and magnitude assumption, the duration of ground shaking had to be estimated. Historical accounts vary significantly, but most of them assume durations of approximately one minute for the magnitude $M_w \approx 8.0$ earthquakes of 1811-1812. For this study, a duration of 45 seconds was assumed.

The final seismic parameter necessary for evaluating the lateral spreading models was the distance from the fault. Based on USGS fault maps, the distance was approximately 17 km, but all the empirical models and calibrations were developed from west coast attenuation relationships. Therefore, an equivalent distance had to be determined. This was conducted by the method proposed by Youd et al. (2002; as described in section 4.4.1 of this thesis), and the equivalent distance was determined to be approximately 10 km.

4.5.1.2 Subsurface Profile. The difficulties developing the soil stratigraphy can be summarized into two categories, soil variability and lack of shallow soil properties. The variability occurs due to the depositional process of an alluvium deposit, and the lack of shallow soil properties was due to the pre-design determination that the foundation elements were to be socketed into bedrock as end-bearing piers.

It is useful to obtain index tests, i.e. grain size distribution and Atteberg limits, for the shallow soil layers at the site in order to use the available correlations for estimating

the strength and settlement characteristics of these soil types. Despite the inexpensive insight available through these tests, no Atterberg limits were determined along the Illinois approach and grain size distribution was only evaluated in the deep soil deposits.

The only information available for the soils below the bridge approach structure were: SPT N-values and visual soil classification. This lack of shallow soil tests made it necessary to interpret the geologic descriptions provided in the boring logs. Since these were logged by a geologist or geotechnical engineer, the descriptions indicate approximate particle diameters and fines content (FC) for the various depths. These interpretations indicated an increase in grain size with depth, so this was applied to the simplified profiles in Figure 4-15.

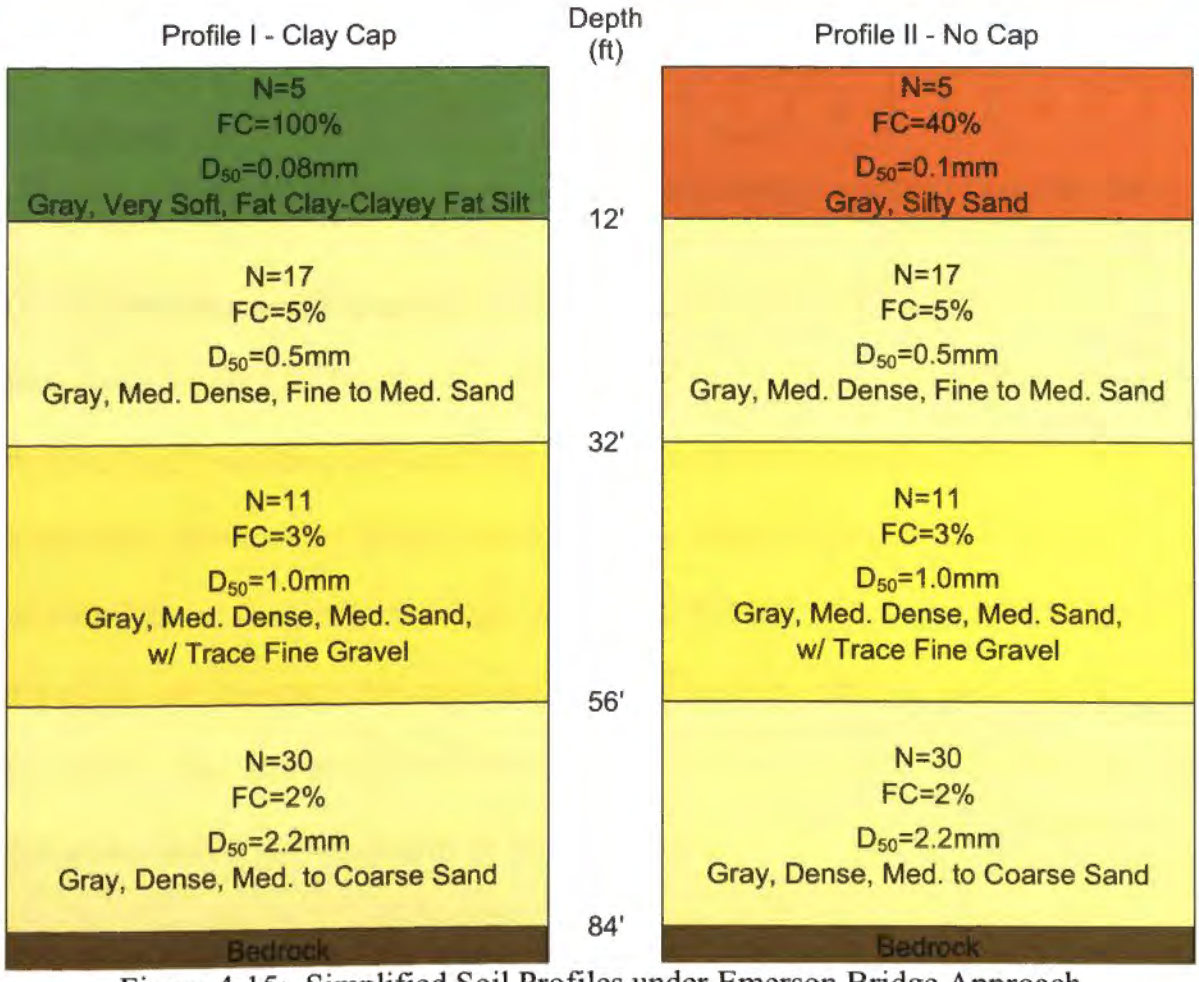

Figure 4-15: Simplified Soil Profiles under Emerson Bridge Approach

The variability in soil strength with depth and amongst each soil layer resulted in a difficult interpretation of the strength profile. Initially, all the borings within the area of interest were collected and compared. An examination of parameters versus depth had little indication of patterns, so an evaluation of the parameters versus elevation was attempted. Again, no patterns were identified. The conglomerate of N-values for every borehole, as well as the average, was plotted versus elevation to try to find a trend, but no trend was found. Therefore, the three boreholes encompassing the two piers within the zone of anticipated lateral spreading (piers 8 and 9 in Figure 4-16) were isolated and averaged to develop the simplified soil profiles, as seen in Figure 4-15.

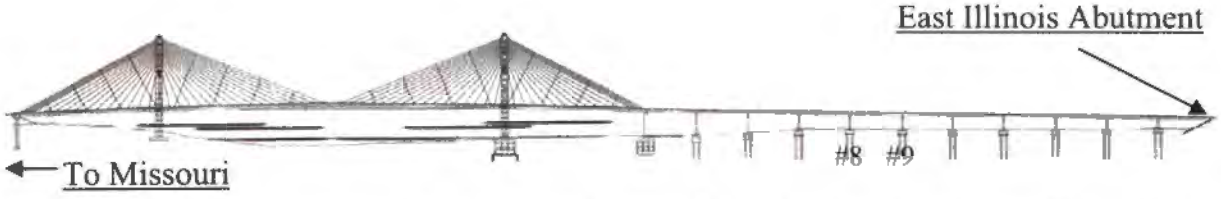

Figure 4-16: Schematic of Bill Emerson Memorial Bridge (modified from Hitt, 2001)

4.5.1.3 Geometry and Topography. The case study for the Bill Emerson Memorial Bridge was afforded the luxury of a LIDAR (Light Detection and Ranging) survey, which provided high resolution elevation data. LIDAR represents an advanced light reflection system that calculates the distance to an object by using the recorded time lapse between the emission and reception of the light beam. The LIDAR unit is attached to the bottom of a plane, and the plane flies over the region of interest collecting numerous elevation data points. The data points are plotted with a software program (Global Mapper 7) to analyze and define the topography of the region.

The LIDAR data for this thesis was provided by Conor Watkins, of the USGS, from a program called USGS SAST (Scientific Assessment and Strategy Team), which combined the efforts of the USGS and others to collect data along the Mississippi River after the 1993 flooding. The data was collected before the bridge construction (sometime between 1995 and 1998), so it is dated for current standards. Its horizontal resolution is only 4-5 meters, while modern data is better than 1.5m resolution (Watkins, 2009). However, this data is still richer than a conventional survey, and the vertical precision can provide elevation contours within +/- 0.15m (6 inches).

The LIDAR data was interpreted at several locations near the bridge site to determine the existence of sloping ground or a free-face to evaluate lateral spreading. Figure 4-17 illustrates the LIDAR data, which produces an image of the Cape Girardeau flood plain and levee system.

Using the LIDAR data in conjunction with Google Earth imagery, the placement of the bridge was determined, and then a profile was developed for that location. The bridge was placed by identifying the geographic coordinates of the left-most pedestal's base. The resulting profile indicated a slope of 1.6% near the waters edge. The apparent free-face had a slope of only10.5%, so the ground slope case was considered. Figure 4-18 shows the Google Earth image next to the LIDAR image with the new and old bridge locations identified, and Figure 4-19 illustrates the surface profile with the slope of interest identified.

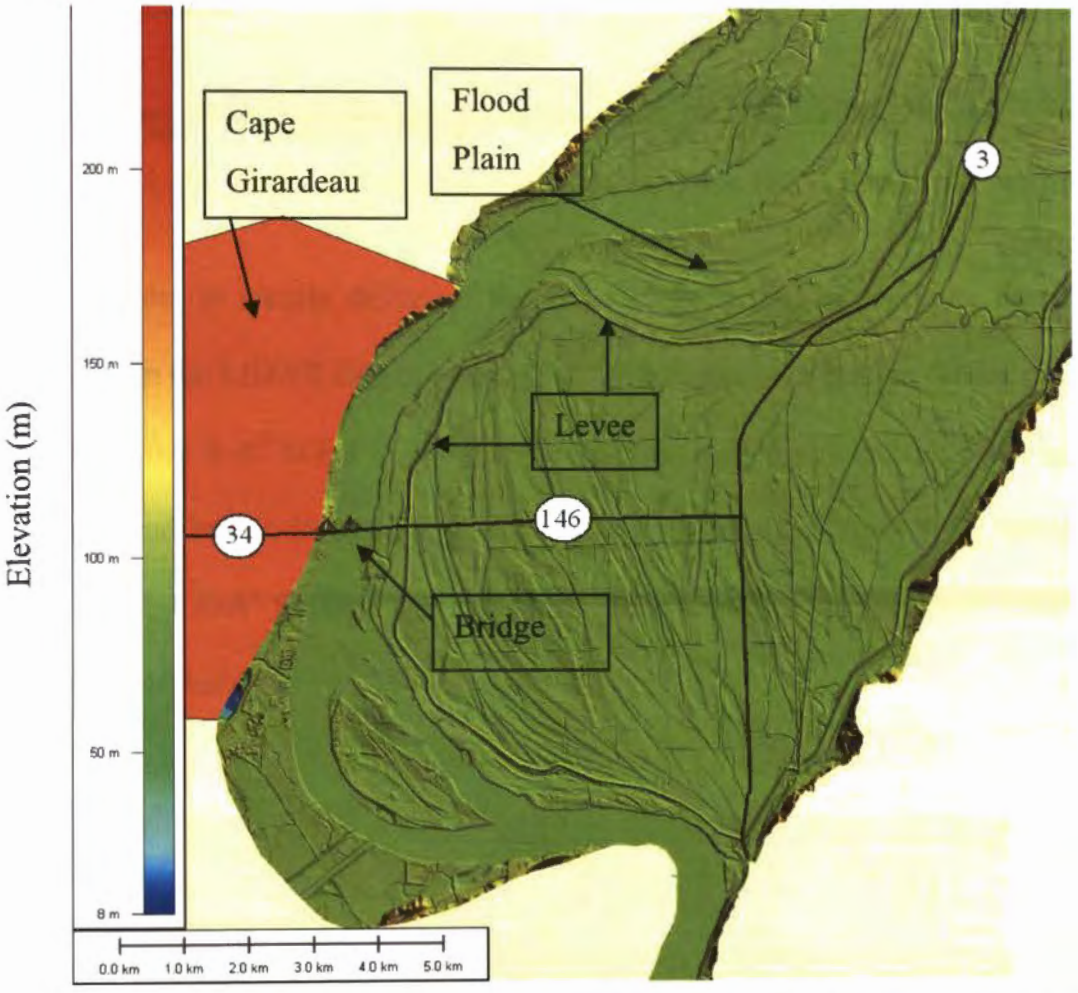

Figure 4-17: Cape Girardeau LIDAR survey (from USGS SAST program)

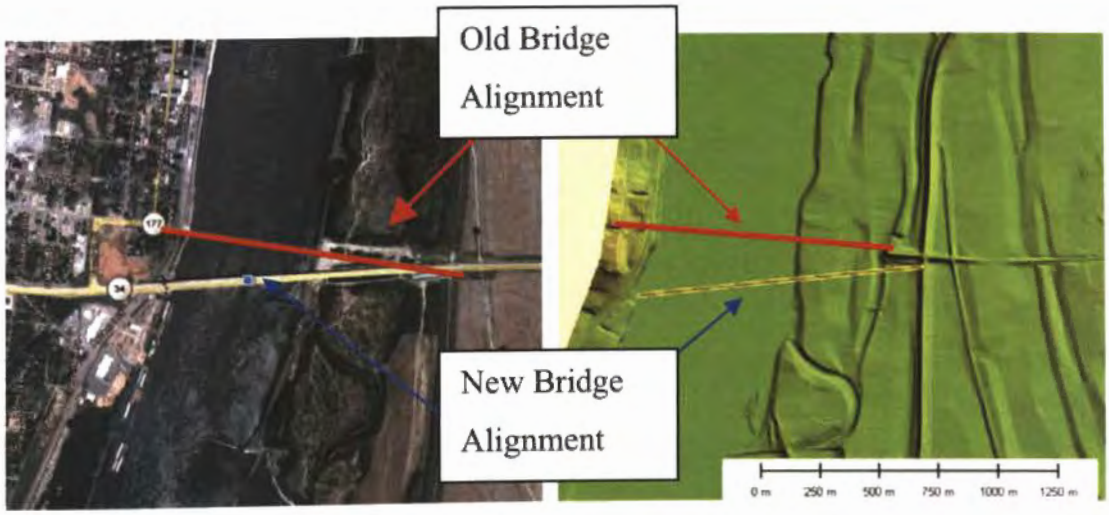

Figure 4-18: Bridge Placement in LIDAR

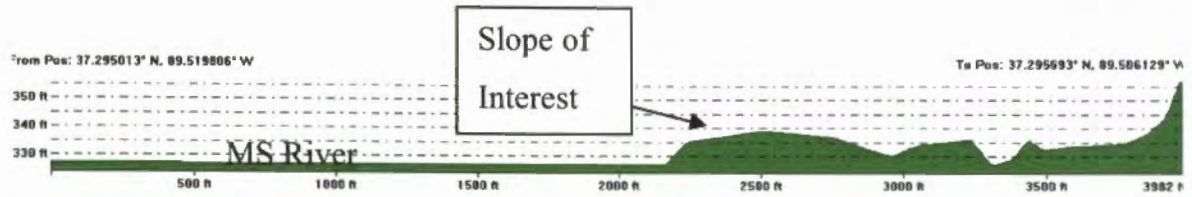

Figure 4-19: Surface Profile under Bridge Location (10:1, horizontal:vertical)

In order to clearly define of the flood plain terrain, a series of profiles were prepared from the LIDAR data to encompass the area near the bridge. These profiles are listed as profiles A-A' to F-F'. The placement of each profile is indicated in Figure 4-20 with the actual bridge location and other ground features. Figures 4-21 through 4-26 display profiles A-A' through F-F', respectively, drawn at an exaggerated scale of 10:1 (horizontal:vertical).

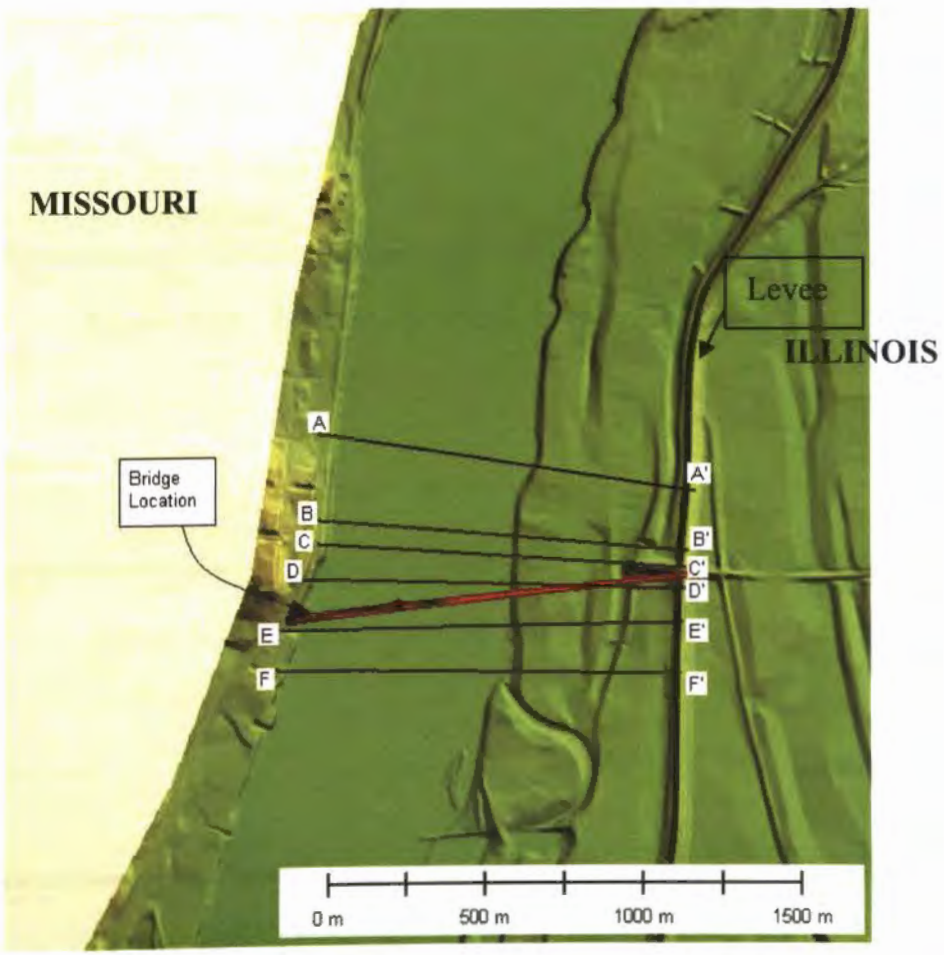

Figure 4-20: Profile A-A' through F-F' Locations

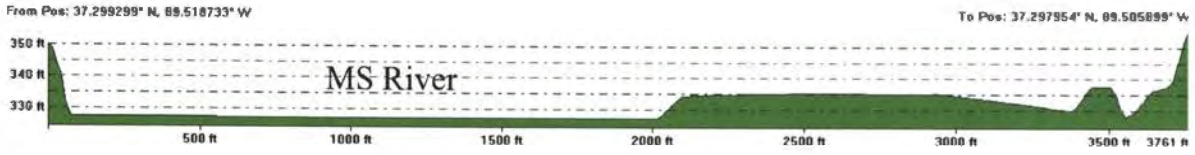

Figure 4-21: Profile A-A' (10:1, horizontal:vertical)

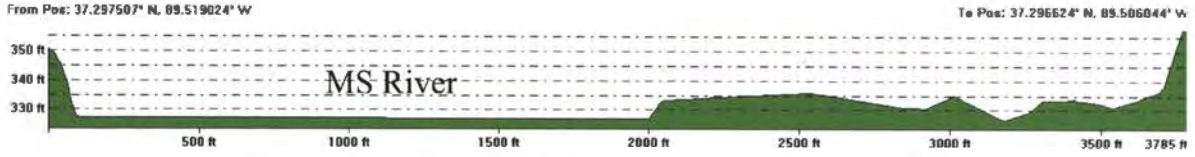

Figure 4-22: Profile B-B' (10:1, horizontal:vertical)

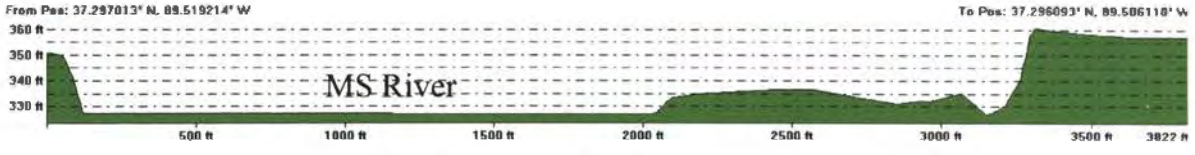

Figure 4-23: Profile C-C' (10:1, horizontal:vertical)

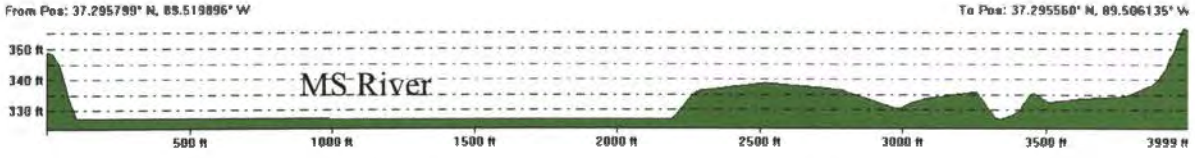

Figure 4-24: Profile D-D' (10:1, horizontal:vertical)

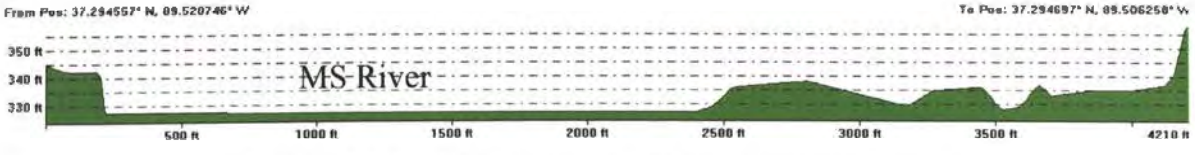

Figure 4-25: Profile E-E' (10:1, horizontal:vertical)

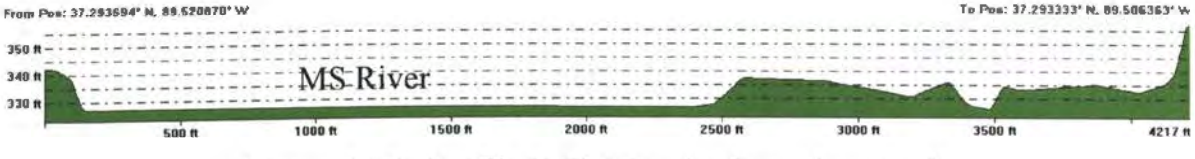

Figure 4-26: Profile F-F' (10:1, horizontal:vertical)

4.5.2. Results of Evaluation. The selected parameters were used to evaluate the liquefaction susceptibility of the site based on the Idriss and Boulanger (2004) method. It was determined that the entire submerged soil profile was susceptible to liquefaction, and that the top 60 feet contained very low factors of safety against liquefaction. Figure 4-27 illustrates the factor of safety against liquefaction for the selected profile and identifies the factor of safety against liquefaction of one with a dashed line.

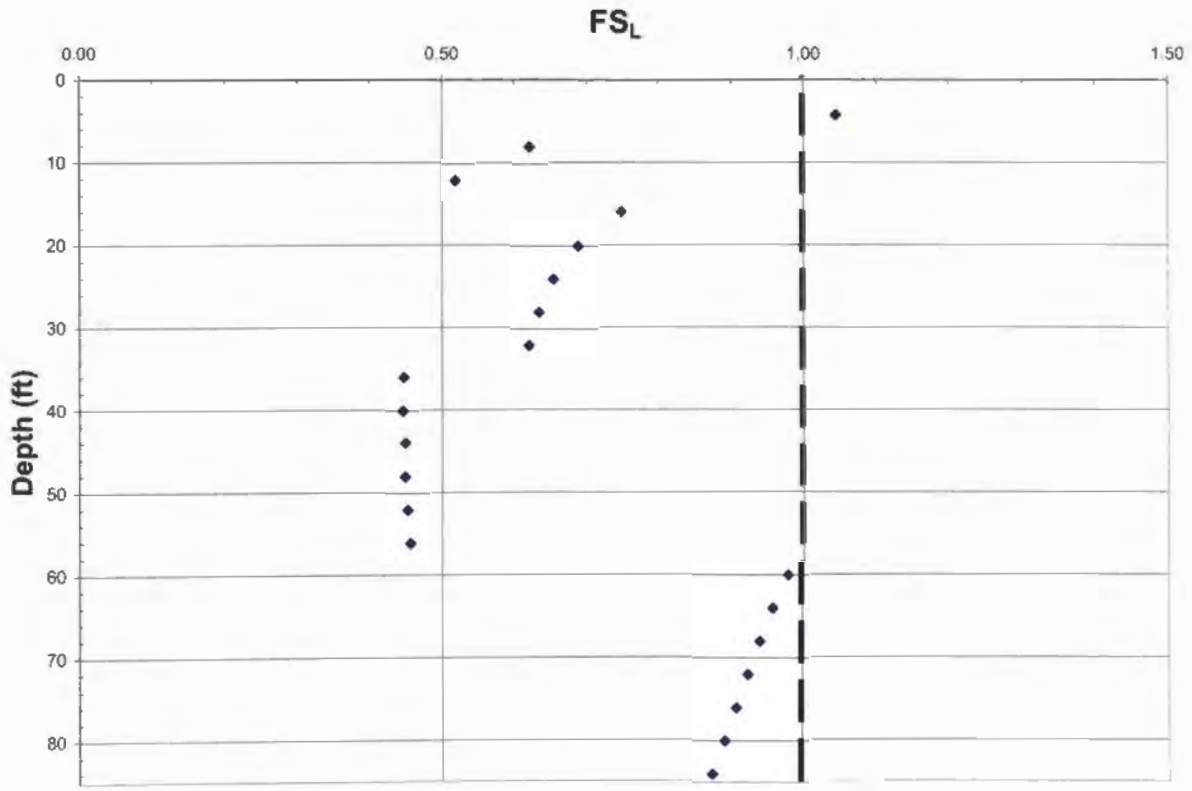

Figure 4-27: Factor of Safety against Liquefaction

Since liquefaction was anticipated, the lateral spreading models were evaluated in accordance with the procedure defined in the appendix of this thesis. The results indicated a displacement of 0.5 to 1.4 m (1.5 to 4 ft) for the slope identified in Figure 4-19. The presence of the fine grained cap material in soil profile I, of Figure 4-16, should increase the thickness of laterally spreading soil and allow larger blocks to move during

the spreading process. The larger mass associated with these larger blocks of soil would cause an increased force to be induced onto the foundation elements. However, the presence of the cap only affected the results of the Youd et al. (2002) model. The other models were not sensitive to the existence of a cap, as seen by comparing the two rows of data in Table 4-3.

Table 4-3: Comparison of Results for the Two Profiles

	Empirical Models				Shear Strain Potential Models			
	G-EPOLLS		Youd et al. (2002)		Zhang et al. (2004)		Idriss and Boulanger (2008)	
Profile Type	D_H (m)	D_H (ft)	D_H (m)	D_H (ft)	D_H (m)	D_H (ft)	D_H (m)	D_H (ft)
Cap Present	0.55	1.65	0.21	0.63	1.37	4.11	1.34	4.01
No Cap	0.55	1.65	0.53	1.62	1.32	3.97	1.34	4.03

The influence of the fine-grained cap, or lack of influence, corresponds to the evaluation process associated with each model. The EPOLLS model requires a parameter defining the depth to the top of the liquefiable layer (Z_{liq}) which in both cases was equal to the depth of the water table. The shear strain potential models utilize the factor of safety against liquefaction for the entire depth of the soil profile, so the thin top layer had little effect on the overall result (a maximum difference of 0.14 ft as seen in Table 4-3). However, the Youd et al. (2002) model relies on the average fines content of all the layers with an N-value less than 15. The presence of the fine-grained cap increased the average fines content of this layer from 15% to 35%, causing a large reduction in the anticipated displacement.

The anticipated displacement of 1 to 4 feet will impose additional lateral force on the upper-portion of the foundation elements, and the liquefied soil layer will reduce the lateral confinement available for the drilled shafts. Due to the 5.5 ft of embedment into

limestone and the reduced lateral support within the liquefied soil, the pier tips will remain stationary, and the pier group will be forced to bend within the liquefied region. This phenomenon is illustrated in the exaggerated deformation schematic drawing of Figure 4-28.

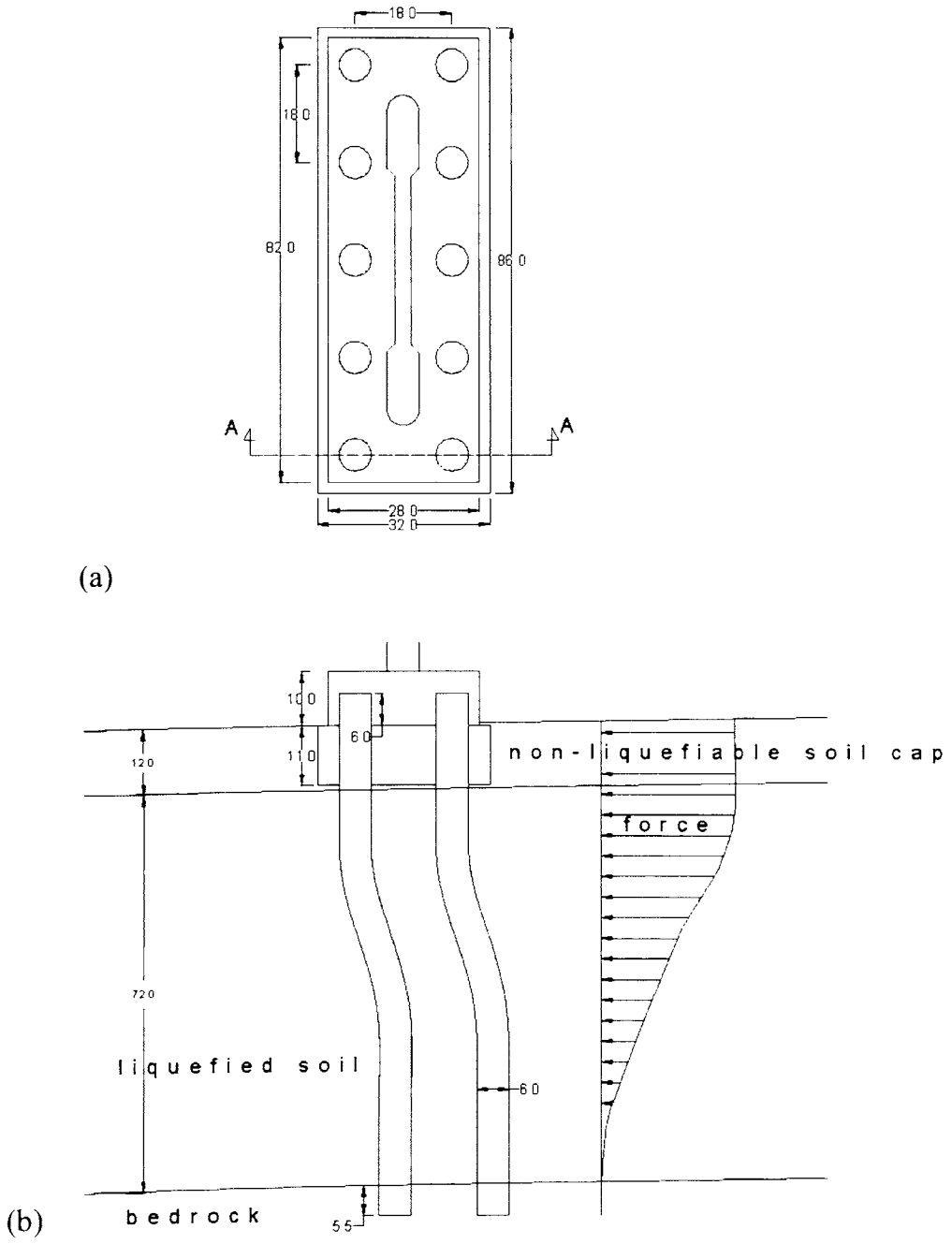

Figure 4-28: Exaggerated Schematic of Pile Bending for a Typical Foundation Element
(a) Top View of Pile Cap (b) Typical Profile View of Pile Bending
(all measurements in feet; Hitt, 2001)

In blasting studies conducted at University of California–San Diego (UCSD), the liquefaction-induced lateral spreading displacement of a pile cap was approximately 50% of the free-field displacement (Ashford et al., 2006). Therefore, the anticipated lateral displacement of the pile cap could be estimated at 0.5 ft to 2 ft for a M_w=6.7 earthquake.

4.5.3. Woodward – Clyde Consultants' Evaluation Results. The 1994 report conducted by Woodward-Clyde Consultants (WCC, now URS) was made available late during these studies which allowed an unbiased prediction to be performed at the site. In comparing the results of the author's and WCC's predictions, it was discovered that the deformation recorded in this thesis (approximately 4 ft) was much less than the 10 ft predicted by WCC. Therefore, an effort was made to identify the source(s) of the discrepancy in the results of the lateral spreading analysis.

As anticipated, the largest distinction between the two evaluations was the site response analysis conducted by WCC that increased the bedrock acceleration values by a factor of 2.5 to 3 (Woodward-Clyde Consultants, 1994). This increase is consistent with analyses conducted by the author in other locations along alluvial plains, but the amplified bedrock motion produces peak ground accelerations greater than 1g at the bridge site. Since none of the empirically-based models evaluated in this thesis can accommodate these accelerations, a site response analysis was not conducted. There is no doubt that estimates of lateral displacement would increase due to site amplification affects. However, using these relationships outside the limits stated by the original developers may render the results less reliable.

Regardless of site amplification, fifteen years of research in geotechnical earthquake engineering since 1994 have produced improved lateral spreading evaluation

models. WCC utilized the Bartlett and Youd (1992) and the Hamada et al. (1986) lateral spreading models, which are the predecessors to the models used within this thesis. As discussed in chapter three of this thesis, Hamada et al. (1986) was the first empirically based lateral spreading model, and the Bartlett and Youd (1992) model was revised by the Bartlett and Youd (1995) model which was further revised by the Youd et al. (2002) model. However, all the revisions applied to the Bartlett and Youd (1992) model only decreased the anticipated deformation by an average of 8%, so this does not account for the noted discrepancy.

Since the models used by WCC did not incorporate the ground acceleration to determine the lateral displacement, the source of distinction between the results must be attributed to something other than the lateral spreading model or the site response analysis. It was determined that the fault location had the largest impact on the results of the analysis. For this thesis, the fault location was taken from the USGS hazard deaggregation map which showed the closest distance to the NMSZ as 17km, while the work done by WCC uses 50km. Based on the attenuation relationship provided by Toro et al. (1994), the bedrock acceleration used in the analysis (0.36g) corresponds to an earthquake magnitude of approximately M_w=8.0 and M_w=6.7 for distances of 50km and 17km, respectively. The analysis completed in this thesis maintained the 0.36g bedrock acceleration provided in the bridge plans and back-attenuated it 17km to the fault location for M_w=6.7. The work completed by WCC used the 0.36g bedrock acceleration with M_s=8.5 (approximately M_w=8.0). Using M_w=8.0 in the prepared spreadsheet returns an anticipated deformation of over 18 ft for the Youd et al. (2002) model, but M_w=7.7

(USGS estimate of a large NMSZ earthquake) returns an anticipated lateral deformation of about 10 ft, as suggested by the WCC's report.

Regardless, the anticipated lateral deformation presented in the analysis of this thesis underestimates the affects of a 2% in 50yr design earthquake, but it presents consistent results for a M_w=6.7 event.

5. THE HONDURAS EXPERIENCE

5.1. INCEPTION OF THE EXCURSION

It was a relaxing Tuesday afternoon as the author lay in his Austin hotel room dwelling on the success of his first conference presentation, when the buzz of a phone call from his graduate advisor, Ronaldo Luna, stirred him to his feet. The anticipated conversation would have addressed details of the presentation, but two looming questions came instead, "Do you have a passport?" and after an affirmative response, "Do you want to go to Honduras?" It was quickly realized that a flight to San Pedro Sula, Honduras was scheduled for 5 AM Friday morning (19 June 2009), and it was a fourteen hour drive from Austin, TX to Rolla, MO.

In the author's short absence from Missouri S&T, the Earthquake Engineering Research Institute (EERI) and Geoengineering Extreme Events Reconnaissance (GEER) had collaborated to sponsor a team of experts in structural engineering, geotechnical engineering, and disaster response and recovery to investigate the damage fomented by an earthquake off the coast of Honduras. The EERI-GEER team was chosen from Missouri S&T and consisted of Abdedjelil Belarbi (supported by EERI), Ronaldo Luna and the author (both supported by GEER). The team was invited by Mr. Marco Sandoval, Executive Director of the Comisión Ejecutiva Valle de Sula (CEVS), whom is responsible for the construction and maintenance of the Sula Valley levee system. Mr. Sandoval also provided a team of CEVS engineers in charge of recovery and reconstruction (Humberto Calderon, Oswaldo Rivera, and Luis Alonso Lopez) to help facilitate the investigations by escorting the team to sites hosting significant damage.

5.2. THE EARTHQUAKE EVENT

On May 28, 2009, residents in several Central American countries were rocked out of their beds by a M_w 7.3 earthquake that struck off the Atlantic coast of Honduras. The epicenter was located 63 km North of Roatán (Bahía Islands) and 125 km NNE of La Ceiba (USGS, 2009). Figure 5-1 locates the epicenter (star) and identifies the tectonic setting for this region.

Figure 5-1: Tectonic Setting (USGS 2009)

It was the strongest earthquake to strike Honduras in over three decades. In addition to Honduras . . . Belize, Nicaragua, El Salvador, and Guatemala felt the primary event, as well as several aftershocks. The earthquake event was of a significant magnitude (M_w 7.3), but there were limited consequences and loss of life that resulted. At least seven people were killed, and forty more were injured. Over one thousand

buildings and residences were damaged during the event. In addition, major infrastructure elements, like port terminals, bridges, and levee networks, were crippled as a result of the event.

5.3. REGIONAL TECTONICS AND SEISMOLOGICAL RECORDS

According to the USGS interpretation of the seismological data, the location and focal mechanism of the Honduras earthquake of May 28, 2009, imply that the shock occurred as the result of left-lateral, strike-slip faulting. This event was located on the Swan Islands Transform Fault, a segment of the boundary between the North American and Caribbean plates. It has been estimated that in this region the plate boundary has a 20 mm/yr slip. (USGS, 2009)

5.3.1. Historical Event of Significance. The North American/Carribean plate boundary has generated strong earthquakes before. Thirty three years ago the 1976 Guatemala earthquake, Mw 7.5, produced more than 23,000 fatalities (Luna et al., 2009). The 1976 earthquake occurred on the Motagua fault, a segment of the plate boundary that lies about 400 kilometers Southwest of the 2009 Honduras offshore hypocenter. Figure 5-2 illustrates the fault system and identifies the 1976 Guatemala earthquake.

5.3.2. Seismologic Records. Seismological records in Honduras are scarce. A recent station was installed by the USGS in Tegucigalpa, the capital city. The record from this station is more than 310 km away from the epicenter. Another seismograph has been in operation for some time now at the El Cajon dam site about 260 km away from the epicenter. Additionally, three accelerographs are also installed at the dam, one at the base and two within the concrete structure. The few stations that have been installed are

monitored and supported by the Instituto Nicaragüense de Estudios Territoriales (INETER) from Nicaragua (Luna et al., 2009).

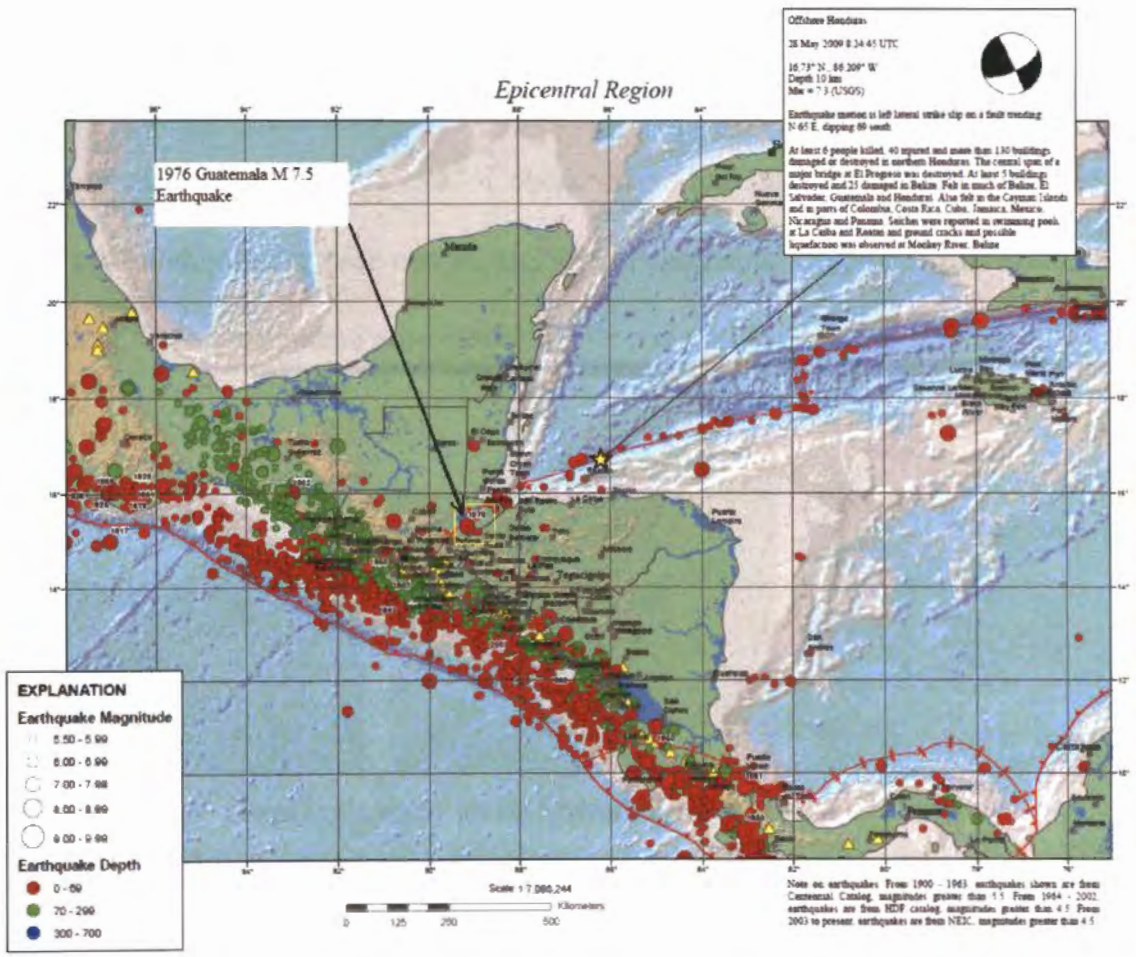

Figure 5-2: Epicentral Region and Historic Earthquake (USGS 2009)

5.4. GEOTECHNICAL PHENOMENA

Though the seismic event incited strong ground motions throughout the region, relatively isolated areas sustained heavy damage. The amplification effects of soft alluvial soil deposits resulted in devastating ground motions along the Ulua, Chamelecon, and Humuya River valleys. Local residences and some important structures, i.e. the Supreme Court Building, experienced similar ground motion amplification affects due to

poorly engineered fill material and soft foundation soils. The Supreme Court Building, for instance, was constructed on a site that was initially considered by a private enterprise. Several meters of fill were emplaced by this private firm to overlay the residual marsh material, but the site was abandoned due to poor soil conditions.

5.4.1. Liquefaction. Many regions underlain by saturated granular sediments showed widespread evidence of liquefaction. Coastal cities, like Puerto Cortes and Omoa, wore the scars of sand boils, surface cracks, and lateral spreading. Figure 5-3 illustrates a few instances of these phenomena near Puerto Cortes and Omoa.

Figure 5-3: Sand boils and Lateral Spreading near Puerto Cortes and Omoa

Similarly, bridge abutments near local riverbeds were accompanied by Allochthonous, or foreign, sand ejecta and liquefaction induced settlement (ten inches or more) along the river banks. Figure 5-4 shows evidence of liquefaction near a local bridge abutment and pier along the Ulua River, which had to contribute to the main span collapse. At this bridge site, a settlement crack running parallel to the river indicated at least 0.75 ft of differential settlement near the southern bridge abutment, and sand boils covering vegetation all the way from the abutment to the river indicated severe liquefaction.

Figure 5-4: Sand boils and settlement near a bridge abutment on the Ulua River

5.4.2. Lateral Spreading. Many coastal and riverine environments throughout Honduras experienced some level of lateral spreading, but the most pronounced regions of lateral spreading were along the network of levees that protect the plantations within the Sula Valley, between the Chamelecon and Ulua Rivers. Figure 5-5 shows a map of the Sula Valley which hosts acres of banana, plantain, and sugar cane plantations. Each number on the map highlights a location of seismic damage (mostly lateral spreading related phenomena), and the white area represents the Sula Valley. The main cities of interest are also identified.

Near the edge of the Ulua River, in the unprotected zone of the levee system, gaping fissures, up to five meters wide and two meters deep, indelibly altered the landscape. Figure 5-6 illustrates these shifting land masses. Sites hosting more severe damages had already been reconstructed prior to the EERI-GEER team deployment, and sites with less extreme failures are not illustrated. In total, nearly 60 km of the levee network were damaged to a level that required repairs by earthwork construction crews.

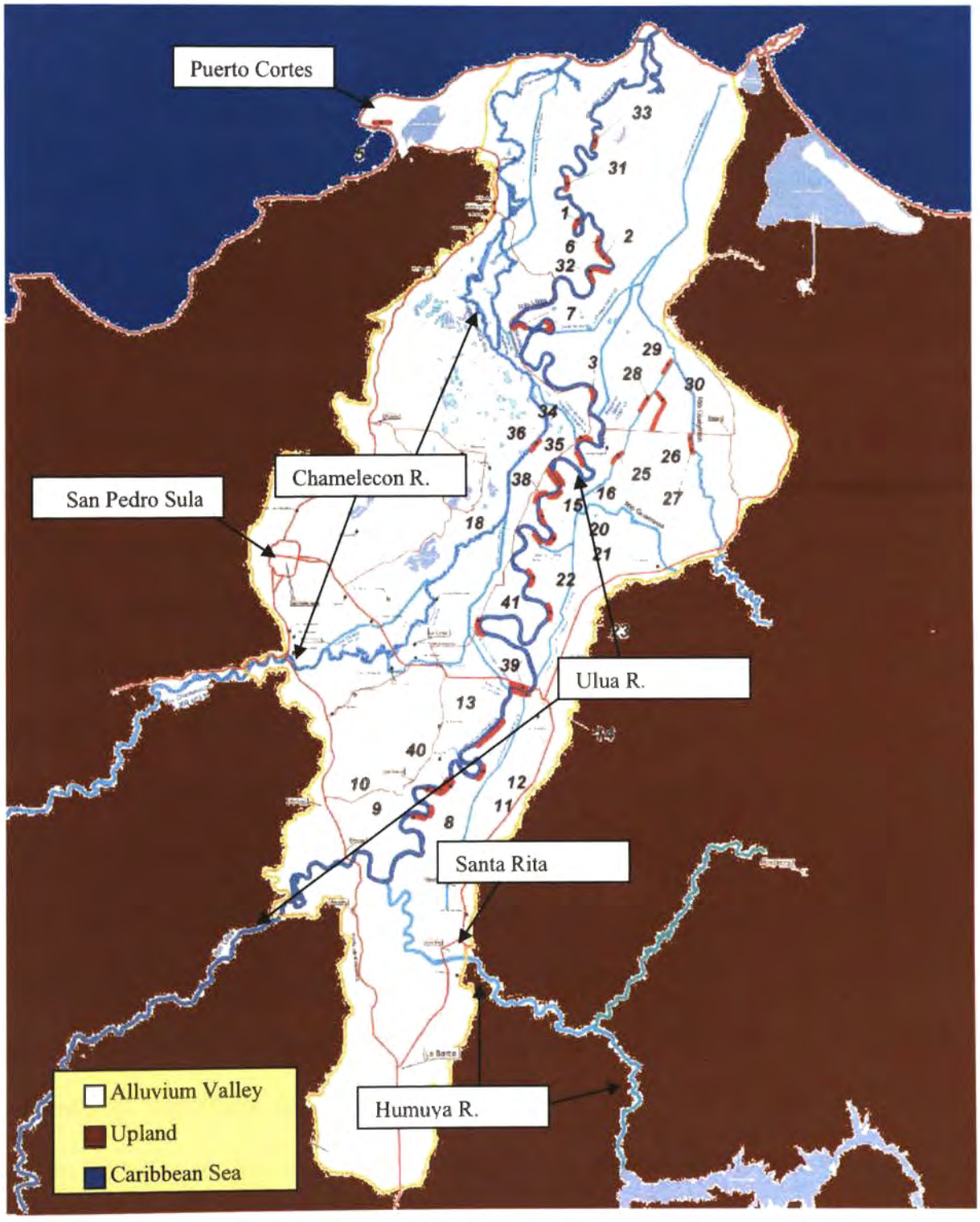

Figure 5-5: Map of the Sula Valley, Honduras (courtesy of CEVS)

Figure 5-6: Lateral Spreading along the Ulua River

For the agriculturally based economy of Honduras, the integrity of the levees and vitality of the plantations are critical. According to Humberto Calderon, a former banana plantation engineer and current civil engineer for CEVS, any flooding of the plantations will destroy one rotation of bananas, and any 24 hour period of inundation will decimate the entire crop of bananas. At the time of the EERI-GEER visit, there were less than three months left to repair the levee network before the September flood season.

5.4.3. Differential Settlement. The subsidence associated with liquefaction, or the combined affects of liquefaction and lateral spreading, was retarded by the presence of deep foundation elements. Structures supported on foundation systems that incorporated a combination of shallow and deep members, like bridge abutments and port facilities, experienced significant differential settlement. The most important port in Honduras, Puerto Cortes, was reported to have pile foundations uplifted during the event, but global subsidence allowed only relative displacements to be measured. Figure 5-7 illustrates the suspected uplift and points of extreme subsidence at Puerto Cortes. Figure 5-8 illustrates Differential Settlement at a bridge over the Ulua River where the abutment contacts the

bridge. In this case, the deep foundation elements of the bridge experienced significantly less settlement than the adjacent abutment.

Figure 5-7: Subsidence and Differential Settlement at Puerto Cortes

Figure 5-8: Differential Settlement at La Democracia Bridge on the Ulua River

5.5. IMPACT OF LIQUEFACTION ON BRIDGES

The relative infrequency of large magnitude earthquakes in the region has allowed designers and engineers to become complacent towards the demands of large seismic events. Especially in aged infrastructure, aseismic design can posit catastrophic results during a large earthquake. Luckily, the locations of extreme lateral spreading, near the

Ulua River's levee system (as seen in figure 5-6, above), were not host to a bridge crossing, where bridge piers could have failed due to the applied loads of these lateral spreads.

Despite the lack of extreme lateral spreading near major river crossings, bridges still succumbed to the dynamic forces of the 2009 seismic event. The La Democracia Bridge, that crosses the Ulua River towards El Progreso, lost its middle span to the river bottom. Along the bank of the river, sand boils, surface cracks, and subsidence were prevalent (indicative of possible lateral spreading, see Figure 5-4). The approach to the abutment experienced significant subsidence compared to the abutment itself (see Figure 5-8). This differential settlement, associated with dissimilar foundations, would have rendered the bridge temporarily impassible, regardless of the middle span collapse.

As a testament to better design practice, the twin bridge to La Democracia is still being utilized. This bridge was built in 2005 by Japanese designers, and incorporates neoprene elastomeric bearing points and shear keys for each pier (Luna et al., 2009). The shear keys were cracked but kept the bridge on its bearings, which proved their necessity during this event. Figure 5-9 illustrates the collapsed span of La Democracia Bridge with the new Japanese twin bridge accommodating traffic in the background.

In contrast to the 2005 design, the La Democracia Bridge (built in 1965 by a team of French engineers) did not incorporate shear key restraint, so larger lateral movements were allowed. The extreme lateral movement coupled with the simply supported middle span (four simply supported T-beams on metal plate bearings) did not supply adequate seismic support for the middle span of La Democracia Bridge.

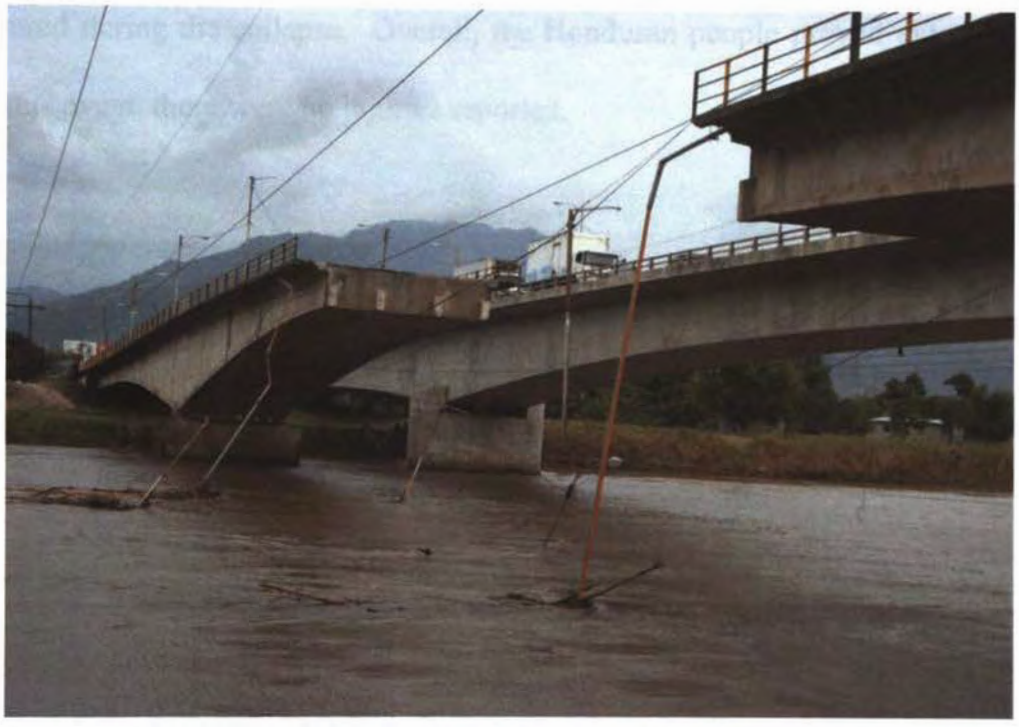

Figure 5-9: Collapsed Span of La Democracia and Surviving Sister Bridge

A bridge crossing the Humuya River near Santa Rita also sustained critical damage during the earthquake. Historically, scour during flood events had weakened the foundation piers which exacerbated the impact of the seismic loading. After the earthquake, several of the supports experienced significant movement. One of the supports was tilted and rotated which resulted in merely two to three inches of bearing for one of the middle spans. Figure 5-10 illustrates the severity of damage. Look closely at the circumscribed region, and the loss of bearing of the girder on the bent.

Since this bridge was the only river crossing for miles, it was still fully operational with heavy truck traffic during the EERI-GEER team's visit. One week after the investigation on the June 28, 2009 night, the minimally supported span and the span adjacent to it collapsed into the river. Figure 5-11 shows the collapsed sections. It is assumed that the bridge deck with limited bearing area collapsed first, followed by a progressive collapse of the other span. Despite the maintained use of this bridge, no one

was injured during the collapse. Overall, the Honduran people proved extremely lucky during this event, there were no injuries reported.

Figure 5-10: Bridge Pier Tilted and Rotated During Earthquake

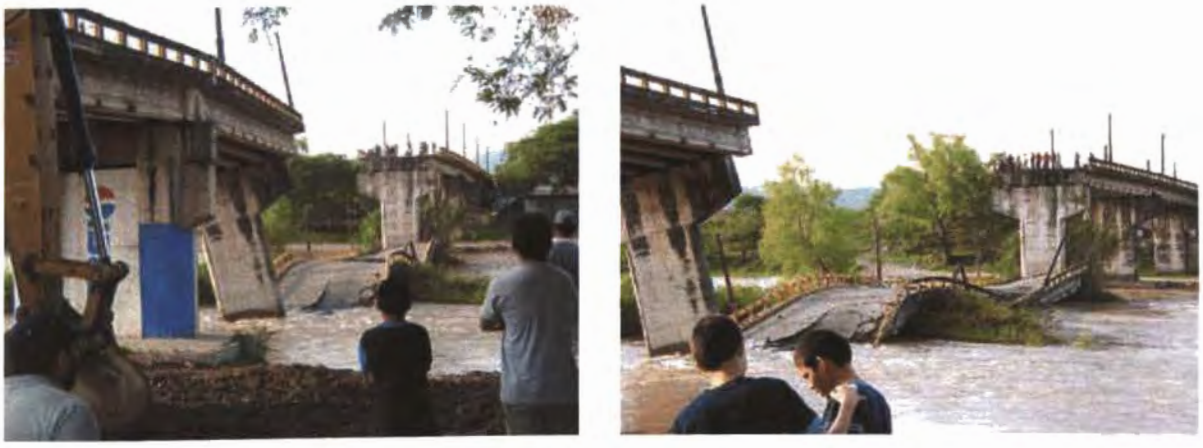

Figure 5-11: Collapsed Sections of the Humuya River Crossing (La Prensa, 2009)

5.6. COMPARISONS TO THE NEW MADRID SEISMIC ZONE

It is useful to draw a comparison between the experiences gained in Honduras and the possible effects of a New Madrid event. At the most basic level, the presence of

alluvial valleys represents the key link between Honduras and the NMSZ. The amplification affects of soft unconsolidated alluvial soils presents an increased seismic risk within river valleys that host recently deposited material. In addition, the relatively loose state of the soil within these recent deposits, and their close proximity to the water table, makes them more susceptible to liquefaction based ground failures.

The greatest impact of seismic ground failure occurs near critical infrastructure. For small communities within the Sula Valley, the Humuya River crossing (Figure 5-10 and 5-11) represents the only bridge for several miles. Upon its collapse, the ability of the emergency response system around Santa Rita was severely hindered, and many of the residents were stranded between home and work. The nearest secondary bridge lies sixteen miles to the north, past where the Humuya River converges with the Ulua River.

This alternate bridge site is host to the twin bridges depicted in Figure 5-9, above. If it were not for the advanced technology implemented by the Japanese in their 2005 design (over 30 years after the other two bridges), it is possible that neither route would be passable. Due to the closure of these two bridges, severe traffic delays were incurred, and many people had to increase their commuting distances by over thirty miles.

Properly replacing the damaged river crossings by constructing new bridges would require funds beyond the government's budget, so the remedial action will utilize as many of the old parts as is feasible. For the Humuya River crossing, the repair may consist of lifting and reinforcing the collapsed pier (as demonstrated by the previous reconstruction habits on the bent adjacent to the collapsed pier in Figure 5-12; also seen in Figure 5-11). The road slabs will most likely need to be replaced, but as much material will be salvaged as possible.

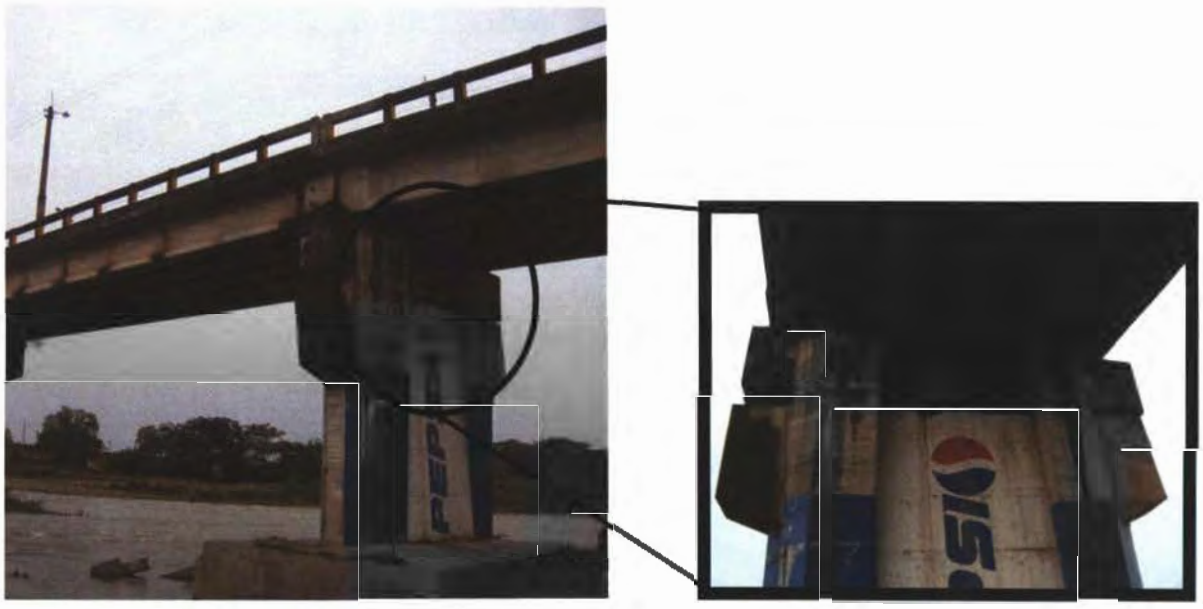

Figure 5-12: Possible Reconstruction Method for the Humuya River Crossing

The NMSZ, like Honduras, hosts several aged infrastructure elements within an alluvial valley. Most of the bridges in the NMSZ were erected prior to the implementation of recent seismic codes and do not account for seismic considerations. If a repeat of the great earthquake series from the NMSZ occurred, many of these structures would be subject to temporary, if not permanent, closure. The presence of a fractured transportation system during post-earthquake response and recovery would drastically hinder their effectiveness, and residents within isolated regions of the Midwest may become marooned within small communities.

Unlike Honduras' relatively distant interplate fault boundary, which was 230km+/-15km from the investigated damage; the intraplate faulting of the NMSZ lies in close proximity to major infrastructure and populated areas. This near field condition of the NMSZ combined with its larger anticipated earthquake magnitude will induce more dramatic displays of seismic failure.

The NMSZ and Honduras also differ in their distribution of ground motion records. The NMSZ has hundreds of recorded earthquakes, but no records of strong ground motion. On the other hand, Honduras' seismological records contain very few earthquakes, but they have recorded strong ground motion acceleration time histories from recent earthquakes.

6. DISCUSSION AND CONCLUSIONS

6.1. DISCUSSION

6.1.1. Compare and Contrast Models. The current state-of-practice for lateral spreading evaluation provides limited variability within the available approaches. As discussed in Chapter three of this thesis, there are only four basic approaches used to evaluate the anticipated deformation of laterally spreading ground. In the Midwest, two of these approaches are nearly impossible, i.e. mechanistic and numerical approaches, due to the availability of data in the Midwest. The feasibility issues associated with these two models further limits the variation within the addressed lateral spreading evaluation methods.

The primary link between every model that was evaluated in this thesis is empiricism. The empirical models, of course, are based solely on empirical relationships observed in real case histories, and the shear strain potential models incorporate an empirical calibration based on recorded case histories. This similarity produces limitations for each model, because the use of empiricism creates upper and lower threshold values where the linear regression was fit to data. Any extrapolation beyond these limits produces solutions of unknown reliability and should only be conducted with extreme caution.

When identifying the distinctions between each model, the stark contrast between the purely empirical models and the shear strain potential models must be addressed first. In the shear strain potential models, the results of laboratory tests are utilized to determine a lateral displacement index. Since this index is independent of the empirical correlations, the strength tests used to determine them do not have to be consistent with

the recorded case histories. This opens the possibility of evaluating the lateral spreading displacement based on SPT or CPT in-situ tests.

6.1.1.1 Distinction within Shear Strain Potential Approaches. The shear strain potential approaches are based on similar research, so the resulting estimations are quite comparable. The main difference between the two approaches lies in their treatment of the in-situ strength to maximum shear strain conversion. The Zhang et al. (2004) model requires an interpolation of a plot which significantly reduces repeatability and hinders its applicability to spreadsheet calculations. The Idriss and Boulanger (2008) approach, on the other hand, incorporated an equation-based process, so the result will be identical despite the operator. The equation-based process also lends itself to easy spreadsheet implementation.

6.1.1.2 Distinction within Empirical Models. Since there is limited availability of recorded earthquakes with lateral spreading displacements, the current empirical models utilize nearly identical data sets for the multi-linear regression of their models. Therefore, the distinction in each model can only be attributed to the selection and treatment of influencing variables or the measurement of the lateral spread. For the evaluation process presented in this thesis, two extremely distinct models were selected.

The EPOLLS model, of Rauch and Martin (2000), is one of the most unique approaches to evaluating lateral spreading using empirical correlations. In an attempt to eliminate the need for evaluating free-face and ground slope conditions independently, Rauch and Martin (2000) incorporated all the variables into a single equation. However, they developed three levels of sophistication (R-EPOLLS, S-EPOLLS, and G-EPOLLS)

that allow the lateral spreading displacement to be estimated with limited data at the initial stage while maintaining refinement capability as additional data is obtained.

The other unique aspect of the EPOLLS model is how the lateral spreading displacement was measured. Rauch and Martin (2000) decided to account for the average displacement associated with a single lateral spreading event. This process produces a single value for the region of interest and appears to be more of a qualitative measure. It is recommended that for an isolated location (e.g. a bridge pier) that this model is used in conjunction with another evaluation model.

The Youd et al. (2002) model uses a different approach, and it is the most widely used method for estimating lateral spreading displacement (Kramer, 2008). In this model, two equations that represent two distinct conditions, i.e. free-face and ground slope, are evaluated, and the maximum prediction from each of these conditions determines the anticipated displacement. In contrast to the EPOLLS model, Youd et al. (2002) documented the case histories of lateral spreading by measuring the displacements in vector form, so each location along the laterally spreading ground is associated with a particular value of displacement.

The following table, Table 6-1, itemizes the advantages and disadvantages attributed to each model used in this thesis.

Table 6-1: Advantages and Disadvantages of Lateral Spreading Evaluation Models

Model	Advantages	Disadvantages
EPOLLS Rauch and Martin (2000)	• Contains multiple levels of sophistication • Can obtain an estimate of displacement with only seismological data • Accounts for a non-liquefiable cap material • Simple to use once the values are determined	• Requires redundant parameters that are difficult to obtain in the Midwest, i.e. T_d and a_{max} when M_w and R_f are already incorporated • Only estimates the average displacement for an entire slide. If evaluating a particular structure, then it needs to be used in conjunction with another model • Requires an FS_{liq} to be evaluated • Developed from a limited region of earthquakes
Youd et al. (2002)	• Most widely used empirical model • Fixed distance and grain size limitations of their previous models • Incorporates a process for determining the equivalent distance • Can determine where the ground slope model begins to supersede the free-face model • Simple to use – only requires N-values	• Must evaluate both the free-face and ground slope models • Developed from a limited region of earthquakes
Zhang et al. (2004)	• Incorporates laboratory data into the model • Can use either SPT or CPT in-situ strength tests	• Requires interpolation of a plot to determine γ_{max} – difficult to apply in a spreadsheet • Requires FS_{liq} to be determined at every depth • Requires a clean sand conversion • Requires a correlation to D_r • Must evaluate the free-face and ground slope models • Slope had little to no affect on the result, if a free-face was present • Only estimates upper-limit of deformation
Idriss and Boulanger (2008)	• Incorporates laboratory data into the model • Can use either SPT or CPT in-situ strength tests • Well-suited for spreadsheet analysis	• No empirical correlation is provided – use another model's correlation • Requires FS_{liq} to be determined at every depth • Requires a clean sand conversion • Only estimates upper-limit of deformation

6.1.2. Unique Midwest Conditions. The local seismic and geological setting within the Midwest limits the application of advanced lateral spreading models. On the West Coast and in Japan, researchers are utilizing knowledge of the fault systems to develop mechanistic models that simulate the actual response of the soil, but the lack of data in the Midwest impedes this research.

6.1.2.1 Seismic. The most critical knowledge gap is within the realm of seismology. Since there have been no strong motion earthquakes (M_w>6.5) recorded from the New Madrid Fault, there are no acceleration time histories. This one information deficiency eliminates the possibility of mechanistic and numerical approaches. The paucity of strong ground seismicity also introduces an unclear depiction of the fault structure and slip mechanisms, so deterministic hazard analysis is difficult to apply. For the empirical models used in this thesis, which are based on actual recorded data, a probabilistic hazard analysis is inappropriate. The probabilistic hazard analysis uses a fusion of multiple earthquake threats to create a mean hazard, but the acceleration and magnitude do not coincide with a particular earthquake. Since the deterministic hazard analysis can not be used and the probabilistic hazard analysis should not be used, it is difficult to select appropriate seismic parameters for the evaluation.

6.1.2.2 Geologic. The geologic conditions associated with the NMSZ are directed towards attenuation evaluation, rather than lateral spreading. The deep soil profiles of the Mississippi Embayment introduce significant problems for attenuating earthquake shear waves from rock to the ground surface. In addition to eliminating the effectiveness of linear-equivalent ground response analysis, the contrast between the shear wave velocities in rock and within the deep alluvial soil deposits increases the low frequency

ground motion amplitudes. Therefore, the acceleration to apply within the lateral spreading evaluation models is quite ambiguous.

6.1.3. Honduras Experience and Midwest Infrastructure. The accounts of damage incurred during the Honduras earthquake (presented in chapter five) should inspire reflection upon the susceptibility of our own infrastructure to seismic failure. With the increase in the anticipated earthquake magnitude and the closer proximity to the fault, stronger ground motions are expected. In the case of the Bill Emerson Memorial Bridge, the seismic design of the superstructure will probably withstand the estimated deformation. However, many older bridges in the NMSZ were built with aseismic designs, and they may not be able to accommodate the anticipated levels of deformation.

The system of levees that failed along the Humuya and Ulua Rivers (Figure 5-11) resemble the flood plain and levees near the Bill Emerson Memorial Bridge, as seen in the LIDAR of Figure 4-17. However, the embankments near the Bill Emerson Bridge approach received ground improvement during the bridge construction. Regardless of the improved embankment, the higher ground motions expected in the NMSZ and the similar soil conditions within the flood plains of each location may produce more severe lateral spreading in the NMSZ than was observed in Honduras.

A comparison of the tectonic settings, known soil conditions, ground features, and local infrastructure for Honduras and the NMSZ are consolidated into Table 6-2.

Table 6-2: Comparison of Local Conditions for Honduras and the Bill Emerson Bridge

	Honduras Investigation	Emerson Bridge Location
Tectonic Setting	• Interplate boundary • Left-lateral strike-slip fault • M_w=7.3 • ≈20mm/yr slip • Fault was over 200 km from the recorded damage	• Intraplate faulting • Right-lateral strike-slip fault • M_w≈7.7 • ≈3mm/yr slip • Intrastructure exists within close proximity to the fault • Recurrence interval of 500+/-300yrs
Soil Conditions	• Alluvium soil deposits • Evidence of liquefied soil	• Alluvium soil deposits • Low SPT blow count material • Nearly 100 ft of potentially liquefiable soil • FS_{liq}<0.5 for most of profile • Thick saturated sand layers that get coarser with depth • Accelerometer arrays are distributed throughout the soil profile
Site Features	• Flood control levees protect areas beyond the flood plain • Gradual slope exists between the levee and the river • Lateral spreading was observed at the levee locations	• Flood control levees isolate the flood plain • Gradual slope exists between the levee and the river • Soil mitigation was conducted under the Illinois abutment
Infrastructure	• Failed structures were aseismically designed • Seismically designed bridge withstood induced ground motion	• Massive structure • Seismically designed • Ten 6 ft diameter drilled shafts per pier on the Illinois approach • Accelerometers are located throughout the structure

6.2. CONCLUSIONS

The conclusion with the largest impact on lateral spreading evaluations in the Midwest region relates to the limitations of the empirical models' parameters. The anticipated peak ground acceleration produced by a design earthquake in the Midwest is significantly higher than the largest peak ground acceleration in the dataset of recorded lateral spreads used for developing the empirical models. Therefore, the reliability of the estimated displacement is unknown. The Youd et al. (2002) model was the only empirical model to suggest limits beyond the design earthquake, but it did not account for

peak ground acceleration. However, the same dataset was applied to the Youd et al. (2002) model as the other empirical methods, so identical limitations should apply to all the models.

In a broader look at lateral spreading evaluation, this thesis addressed the implementation of laboratory data with empirical calibration to estimate lateral spreading displacement (called shear strain potential models in this thesis). The results of these models were consistently higher than the purely empirical models, so it is concluded that the shear strain potential models are more conservative than the purely empirical models in a Midwest lateral spreading evaluation.

For the particular case of the Bill Emerson Memorial Bridge evaluation, the most profound conclusion corresponds to the factor of safety against liquefaction. Even with an earthquake of M_w=6.7 (one less than the design M_w=7.7), the entire soil profile was found to be susceptible to liquefaction, and extremely low factors of safety ($\approx$0.5) were present between ten and sixty feet depth. The anticipated liquefied state of the soil in conjunction with the topography and geometry of the flood plain may produce significant lateral spreading displacement at the Bill Emerson Bridge site.

7. RECOMMENDATIONS FOR FUTURE RESEARCH

7.1. FUTURE EVALUATIONS

The contents of this thesis investigates a broad spectrum of available techniques for evaluating lateral spreading displacements and isolates the methods that are compatible with a Midwest application (i.e. empirical and shear strain potential models). However, it did not exhaust the pool of developed models, so further research could compare the results of other models with the results of the models presented in this thesis. In particular, there are several more shear strain potential models which utilize alternate calibration techniques (e.g. Shamato et al. (1998), Tokimatsu and Asaka (1998), and Faris et al. (2006)).

In addition to evaluating additional models, the analysis approach presented in this thesis could be extended to other locations within the NMSZ. The author had planned on evaluating additional bridge locations (e.g. I-57 near Cairo, IL), but time constraints eliminated that option. It would also be advantageous to conduct a site response analysis prior to estimating lateral spreading displacement. The site response analysis should produce more realistic peak ground accelerations (PGA's), but the anticipated PGA's in the NMSZ are beyond the range of contemporary techniques.

7.2. MODEL DEVELOPMENT

Within the empirical models evaluated for this thesis, there were several variables presented as influencing factors for lateral spreading displacement. Future research associated with the improvement of these models would incorporate:

- a full parametric study of each model to identify the contribution of each variable within the model
- a comparison of each variables contribution against theoretical values
- development of a model that combines the influence of the ground slope and the free-face (like the EPOLLS models) while maintaining the ability to evaluate the contribution of each condition

7.3. RELATED RESEARCH

There are many advances that can be achieved outside the realm of model evaluation and development that would assist in a Midwest lateral spreading evaluation, but none are more critical than improving the seismic data for the Midwest. To directly increase the number of lateral spreading evaluation models that are compatible with the Midwest setting, one of the following should be developed:

- development of a synthetic ground history that emulates a NMSZ event
- development of a deterministic acceleration time history for the NMSZ

APPENDIX
SPREADSHEET DEVELOPMENT GUIDE

The purpose of this appendix is to describe the spreadsheet-based evaluation process and define the equations used to develop the individual tabs. Each figure indicates a distinct tab within the spreadsheet, and the order they are presented reflects the appropriate location (from left to right) within the spreadsheet. Once the spreadsheet is established, the evaluation process can be conducted by the following six (6) steps.

Step 1: Conduct a liquefaction analysis by filling in any blank cell on the liquefaction tab (Figure A-1) with the appropriate data. The necessary inputs include: elevation at the top of the boring, depth to the water table, maximum horizontal acceleration, earthquake magnitude, hammer efficiency, soil type (sandy or clayey), depth to sample, N-value for sample, fines content of sandy soil, and pre-consolidation stress of clayey soil. The remainder of the cells are automatically calculated (automatically calculated cells are indicated by shading within the cell). The equations for the automatically filled cells are presented below, but some cells require IF statements due to their dependence on the soil type and minimum or maximum allotted values. The values that require IF statements due to the soil type are: the effective unit weight (γ'), the cyclic resistance ratio ($CRR_{M=7.5}$), and magnitude scaling factor (MSF). Therefore, two equations (labeled a and b) will be provided for each of these values (a simplified spreadsheet would minimize the applicability to sandy soil and eliminate the required IF statements). The necessary equations are provided below.

Idriss & Boulanger (2004) - SPT Based Liquefaction Potential

Elevation at the Top of Boring ==========	327	feet
Depth to Groundwater Table ==========	6	feet
Max. Horizontal Surface Acceleration =====	0.36	(g)
Design Earthquake Magnitude ==========	6.7	
Hammer Efficiency ==========	60	(%)

Soil Type C=Clayey S=Sandy (PI<7?)	Depth (feet)	Elevation (feet)	N - Value (blows/ft)	Sand FC (%)	Clay σ_p' (ksf)	(1) γ' (pcf)	(2) σ_v' (ksf)	(3) σ_v (ksf)	(4) $(N_1)_{60}$	(5) $\Delta(N_1)_{60}$	(6) $(N_1)_{60cs}$	(7) D_R (%)	(8) C_σ	(9) K_σ	(10) OCR	(11) $CRR_{M=7.5}$	(12) α	(13) β	(14) r_d	(15) MSF	(16) $CSR_{M=7.5}$	(17) FS
C	4	323	5	100	0.5	111	0.4	0.3	8	6	13	0.4	0.08	1	1.13	0.20	-0	0	0.99	1.04	0.16	1.24
C	8	319	5	100	0.8	55	0.7	0.8	7	6	12	0.39	0.08	1	1.21	0.21	-0	0	0.97	1.04	0.26	0.80
C	12	315	5	100	1	55	0.9	1.3	6	6	12	0.37	0.08	1	1.13	0.20	-0	0	0.95	1.04	0.30	0.65
S	16	311	17	5		66	1.1	1.8	20	0	21	0.66	0.13	1	Sand	0.20	-0	0	0.92	1.23	0.27	0.75
S	20	307	17	5		66	1.4	2.3	19	0	19	0.64	0.13	1	Sand	0.19	-0	0	0.89	1.23	0.27	0.69
S	24	303	17	5		66	1.7	2.8	18	0	18	0.63	0.12	1	Sand	0.18	-1	0.1	0.86	1.23	0.27	0.66
S	28	299	17	5		66	1.9	3.3	17	0	18	0.61	0.12	1	Sand	0.17	-1	0.1	0.83	1.23	0.27	0.64
S	32	295	17	5		66	2.2	3.8	16	0	17	0.6	0.12	1	Sand	0.17	-1	0.1	0.80	1.23	0.27	0.62
S	36	291	11	3		62	2.4	4.3	10	0	10	0.47	0.09	1	Sand	0.12	-1	0.1	0.77	1.23	0.26	0.45
S	40	287	11	3		62	2.7	4.8	10	0	10	0.46	0.09	1	Sand	0.12	-1	0.1	0.75	1.23	0.26	0.45
S	44	283	11	3		62	2.9	5.3	10	0	10	0.46	0.09	1	Sand	0.11	-1	0.1	0.72	1.23	0.25	0.45
S	48	279	11	3		62	3.2	5.8	9	0	9	0.45	0.09	1	Sand	0.11	-1	0.1	0.69	1.23	0.25	0.45
S	52	275	11	3		62	3.4	6.3	9	0	9	0.44	0.09	1	Sand	0.11	-1	0.1	0.67	1.23	0.24	0.46
S	56	271	11	3		62	3.7	6.8	9	0	9	0.44	0.09	1	Sand	0.11	-2	0.2	0.64	1.23	0.24	0.46
S	60	267	30	2		71	4.0	7.3	23	0	23	0.71	0.15	0.9	Sand	0.24	-2	0.2	0.62	1.23	0.24	0.98
S	64	263	30	2		71	4.2	7.9	23	0	23	0.7	0.15	0.9	Sand	0.23	-2	0.2	0.60	1.23	0.24	0.96
S	68	259	30	2		71	4.5	8.4	22	0	22	0.69	0.14	0.9	Sand	0.22	-2	0.2	0.58	1.23	0.23	0.94
S	72	255	30	2		71	4.8	8.9	21	0	21	0.68	0.14	0.9	Sand	0.21	-2	0.2	0.57	1.23	0.23	0.93
S	76	251	30	2		71	5.1	9.5	21	0	21	0.67	0.14	0.9	Sand	0.20	-2	0.2	0.56	1.23	0.22	0.91
S	80	247	30	2		71	5.4	10.0	20	0	20	0.66	0.13	0.9	Sand	0.20	-2	0.2	0.55	1.23	0.22	0.89
S	84	243	30	2		71	5.7	10.5	20	0	20	0.65	0.13	0.9	Sand	0.19	-2	0.2	0.54	1.23	0.22	0.88

Figure A-1: Liquefaction Spreadsheet

Key to Column Equations

Col (1) Effective Unit Weight (γ') (pcf):

$$\gamma' = 95(N)^{0.095} \quad \text{(above water table)} \qquad \text{A-1a}$$

$$\gamma' = 105(N)^{0.07} - 62.4 \quad \text{(below water table)} \qquad \text{A-1b}$$

Col (2) Effective Vertical Stress (σ_v') (psf):

$$\sigma_v' = \gamma' * h \qquad \text{A-2}$$

Col (3) Total Vertical Stress (σ_v) (psf):

$$\sigma_v = \sigma_v' + 62.4(h_w) \qquad \text{A-3}$$

Col (4) Normalized SPT Blow-Counts ($(N_1)_{60}$):

$$(N_1)_{60} = [0.77 \log(\frac{40}{\sigma_v'(ksf)})] * N \qquad \text{A-4}$$

Col (5) Fines Content Correction for SPT Blow-Counts ($\Delta(N_1)_{60}$):

$$\Delta(N_1)_{60} = e^{[1.63 + \frac{9.7}{FC} - (\frac{15.7}{FC})^2]} \qquad \text{A-5}$$

Col (6) Clean Sand Equivelant SPT Blow-Counts ($(N_1)_{60cs}$):

$$(N_1)_{60cs} = (N_1)_{60} + \Delta(N_1)_{60} \qquad \text{A-6}$$

Col (7) Relative Density (D_r):

$$D_r = \sqrt{\frac{(N_1)_{60cs}}{46}} \qquad \text{A-7}$$

Col (8) Sigma Coefficient (C_σ):

$$C_\sigma = \frac{1}{18.9 - 17.3 D_r} \leq 0.3 \qquad \text{A-8}$$

Col (9) Sigma Coefficient II (K_σ):

$$K_\sigma = 1 - C_\sigma \ln(\frac{\sigma_{vo}'}{P_a}) \leq 1.0 \qquad \text{A-9}$$

Col (10) Over-Consolidation Ratio (OCR):

$$OCR = \frac{\sigma_p'}{\sigma_v'} \qquad \text{A-10}$$

Col (11) Cyclic Resistance Ratio ($CRR_{M=7.5}$) of Soil:

$$CRR_{M=7.5} = e^{[\frac{(N_1)_{60cs}}{14.1} - (\frac{(N_1)_{60cs}}{12.6})^2 - (\frac{(N_1)_{60cs}}{23.6})^3 + (\frac{(N_1)_{60cs}}{25.4})^4 - 2.8]} \quad \text{(Granular)} \qquad \text{A-11a}$$

$$CRR_{M=7.5} = 0.18 * OCR^{0.8} \quad \text{(Cohesive)} \qquad \text{A-11b}$$

Col (12) Alpha Factor (α):

$$\alpha = -1.012 - 1.126 \sin(\frac{z}{11.63} + 5.133) \qquad \text{A-12}$$

Col (13) Beta Factor (β):

$$\beta = 0.106 + 0.118 \sin(\frac{z}{11.63} + 5.142) \qquad \text{A-13}$$

Col (14) Depth Reduction Factor (r_d):

$$r_d = e^{(\alpha + \beta * M_w)} \qquad \text{A-14}$$

Col (15) Magnitude Scaling Factor (MSF) for Granular Soil:

$$MSF = 6.9e^{(\frac{-M_w}{4})} - 0.058 \leq 1.8 \quad \text{(Granular)} \qquad \text{A-15a}$$

$$MSF = 1.12e^{(\frac{-M_w}{4})} + 0.828 \leq 1.13 \quad \text{(Cohesive)} \qquad \text{A-15b}$$

Cyclic Stress Ratio ($CSR_{M=7.5}$):

$$CSR_{M=7.5} = 0.65(\frac{\sigma_v * a_{\max}}{\sigma_v'})(\frac{r_d}{MSF})(\frac{1}{K_\sigma}) \quad \text{A-16}$$

Factor of Safety against Liquefaction (FS_{liq}):

$$FS_{liq} = \frac{CRR_{M=7.5}}{CSR_{M=7.5}} \quad \text{A-17}$$

Based on the results of the liquefaction analysis, a plot for the FS_{liq} versus depth can be developed to illustrate the liquefaction potential of the site. The plot, as seen in Figure A-2, can be placed within the liquefaction tab or as a new tab.

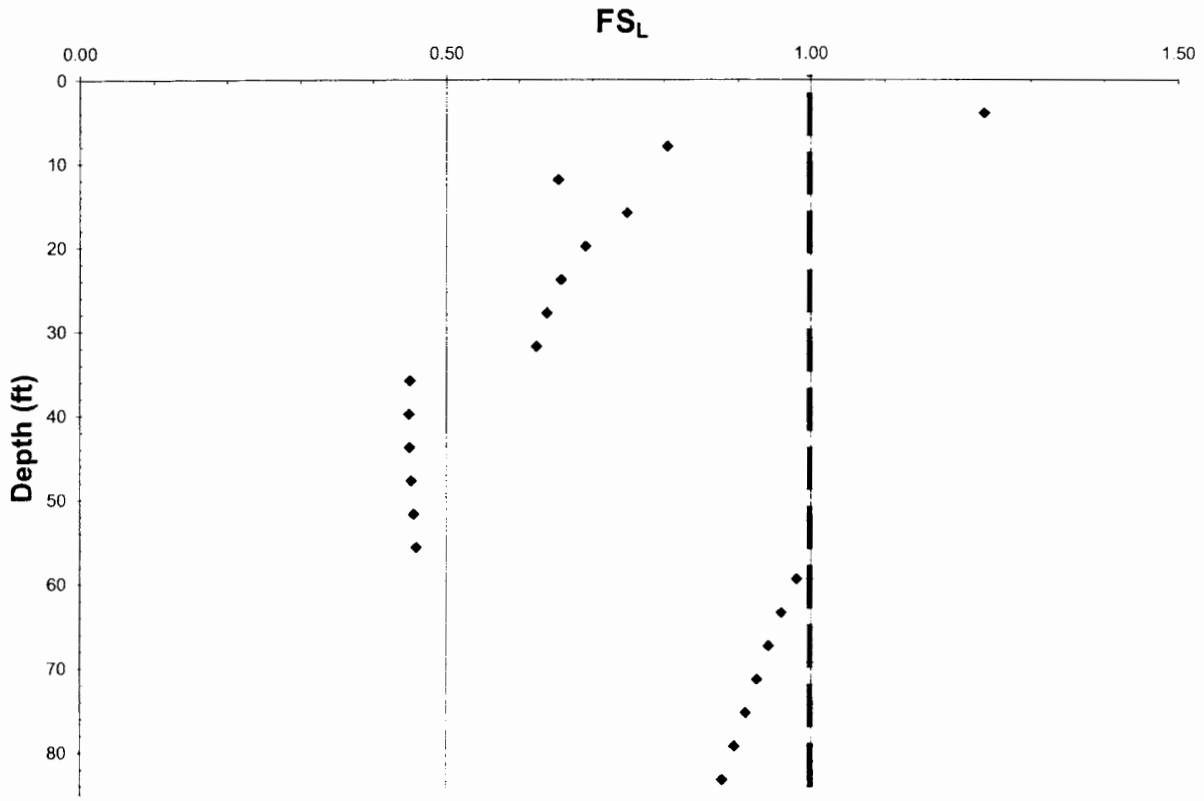

Figure A-2: Plot of Factor of Safety against Liquefaction versus Depth

Step 2: If liquefaction is determined to be likely at the site, continue to the start analysis tab (Figure A-3).

EPOLLS Model						
Variables that influence lateral spreading evaluation			Minimum	Maximum	Evaluation Value	
Regional	M_w	Earthquake magnitude	6.5	9.2	M_w	6.7
	R_f (km)	Distance from vertical projection of fault	0	119	R_f (km)	10
	A_{max} (g)	Peak amplitude of horizontal acceleration	0.16	0.52	A_{max} (g)	0.36
	T_d (s)	Duration of earthquake shaking (with A>0.05g)	4	88	T_d (s)	45
Site	L_{slide} (m)	Maximum horizontal length of lateral spread	20	1360	L_{slide} (m)	107
	S_{top} (%)	Slope of surface topography being analyzed	-0.7	5.2	S_{top} (%)	1.60
	H_{face} (m)	Height of free-face exposure	0	9	H_{face} (m)	0.0
Geo-tech	Z_{FSmin} (m)	Average depth to the point of minimum factor of safety	2.4	12.4	Z_{FSmin} (m)	12
	Z_{liq} (m)	Average depth to the top of the liquefied layer	0.9	7.3	Z_{liq} (m)	2

Youd et al. 2002 Model					
Variables that influence lateral spreading evaluation		Minimum	Maximum	Evaluation Value	
D_H (m)	Estimated horizontal displacement	0.1 m	6 m	D_H (m)	
M_w	Earthquake moment magnitude	6	8	M_w	6.7
R_f (km)	Distance to vertical projection of fault	0.5 km		R_f (km)	10
H (m)	Height of free-face exposure			H (m)	0.0
L (m)	Distance from free-face			L (m)	
W (%)	Ratio of free-face height (H) to Distance (L) = H/L*100	1%	20%	W (%)	
T_{15} (m)	Cumulative thickness of soil with $(N_1)_{60}$<15	1 m	15 m	T_{15} (m)	12
F_{15} (%)	Average fines content of T_{15}	The combination should plot within bounds on figure below		F_{15} (%)	35
$(D_{50})_{15}$ (mm)	Mean grain size for liquefiable (N<15) layer			$(D_{50})_{15}$ (mm)	0.7
S (%)	Slope of the surface topography being analyzed	0.1%	6%	S (%)	1.60
Z_T	Depth to top of liquefied layer	1 m	10 m	Z_T	2

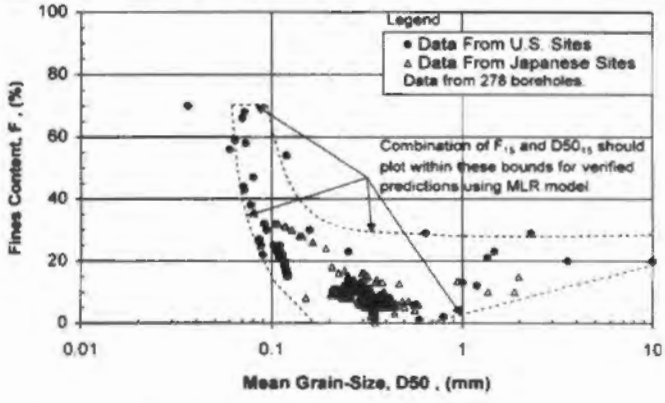

Figure A-3: Start Page for Lateral Spreading Spreadsheet

In this tab, the different variables needed for the analysis and their appropriate limits are defined. The values entered into the column labeled "evaluation value" are linked to the remainder of the spreadsheet for evaluation.

Step 3: The spreadsheet will progress towards the right as the complexity of the models is increased. As discussed in chapter three, the complexity of the models coincides with the year of development, so the evaluation models are organized in the spreadsheet from left to right as: Rauch and Martin (2000) EPOLLS model, Youd et al. (2002) model, Zhang et al. (2004) model, and Idriss and Boulanger (2008) model.

EPOLLS Model for Lateral Spreading (2000)

Variables that influence lateral spreading evaluation			Minimum	Maximum
Regional	M_w	Earthquake magnitude	6.5	9.2
	R_f (km)	Distance from vertical projection of fault	0	119
	A_{max} (g)	Peak amplitude of horizontal acceleration	0.16	0.52
	T_d (s)	Duration of earthquake shaking (with A>0.05g)	4	88
Site	L_{slide} (m)	Maximum horizontal length of lateral spread	20	1360
	S_{top} (%)	Slope of surface topography being analyzed	-0.7	5.2
	H_{face} (m)	Height of free-face exposure	0	9
Geo-tech	Z_{FSmin} (m)	Average depth to the point of minimum factor of safety	2.4	12.4
	Z_{liq} (m)	Average depth to the top of the liquefied layer	0.9	7.3

Notes: Liquefaction Susceptibility must be determined prior to evaluation
Designed to predict average displacement over entire area
When evaluating a single structure, use in conjunction with another model
Reliability outside of W. US and Japan is unkown

M_w	R_f (km)	A_{max} (g)	T_d (s)	L_{slide} (m)	S_{top} (%)	H_{face} (m)	Z_{FSmin} (m)	Z_{liq} (m)	D_H (m) R-EPOLLS	D_H (m) S-EPOLLS	D_H (m) G-EPOLLS
6.7	10	0.36	45	107	1.60	0.001	12	2	0.29	0.18	0.55
6.7	10	0.36	45	107	1.60	0.001	12	2	0.29	0.18	0.55
6.7	10	0.36	45	107	1.60	0.001	12	2	0.29	0.18	0.55
6.7	10	0.36	45	107	1.60	0.001	12	2	0.29	0.18	0.55
6.7	10	0.36	45	107	1.60	0.001	12	2	0.29	0.18	0.55
6.7	10	0.36	45	107	1.60	0.001	12	2	0.29	0.18	0.55
6.7	10	0.36	45	107	1.60	0.001	12	2	0.29	0.18	0.55
6.7	10	0.36	45	107	1.60	0.001	12	2	0.29	0.18	0.55
6.7	10	0.36	45	107	1.60	0.001	12	2	0.29	0.18	0.55
6.7	10	0.36	45	107	1.60	0.001	12	2	0.29	0.18	0.55

$\text{R-EPOLLS}=(0.613M_w-0.0139R_f-2.42A_{max}-0.0114T_d-2.21)^2+0.149$

$\text{S-EPOLLS}=(0.613M_w-0.0139R_f-2.42A_{max}-0.0114T_d+0.000523L_{slide}+0.0423S_{top}+0.0313H_{face}-2.44)^2+0.111$

$\text{G-EPOLLS}=(0.613M_w-0.0139R_f-2.42A_{max}-0.0114T_d+0.000523L_{slide}+0.0423S_{top}+0.0313H_{face}+0.0506Z_{FSmin}-0.0861Z_{liq}-2.49)^2+0.124$

Figure A-4: Spreadsheet for EPOLLS Model

Figure A-4 illustrates the EPOLLS tab in the spreadsheet. In this tab, all of the necessary columns are automatically filled, so there is no need to enter any new data. The data in most of these cells are linked to the start tab (Figure A-3), but the cells indicating the estimated horizontal displacement (D_H) for each model are filled with the following equations:

Regional EPOLLS Model (R-EPOLLS):

$$D_H = (0.613M_w - 0.0139R_f - 2.42a_{\max} - 0.0114T_d - 2.21)^2 + 0.149 \quad \text{A-18}$$

Site EPOLLS Model (S-EPOLLS):

$$D_H = (0.613M_w - 0.139R_f - 2.42a_{max} - 0.0114T_d + 0.000523L_{slide} + 0.0423S_{top} + 0.01313H_{face} - 2.44)^2 + 0.111 \quad \text{A-19}$$

Geotechnical EPOLLS (G-EPOLLS):

$$D_H = (0.613M_w - 0.139R_f - 2.42a_{max} - 0.0114T_d + 0.000523L_{slide} + 0.0423S_{top} + 0.01313H_{face} + 0.0506Z_{FSmin} - 0.0861Z_{liq} - 2.49)^2 + 0.124 \quad \text{A-20}$$

Step 4: Continuing to move towards the right through the tabs, the Youd et al. (2002) tab (Figure A-5) is the first model to require extra input. The column labeled "L (m)" represents the distance from the free-face for the calculation. This column should be filled with the distances of interest for the project. If a bridge is being evaluated, the locations of the pier bents may be selected. The remainder of the cells in this tab are either linked to the start tab (Figure A-3) or filled with equations. As in the EPOLLS tab, the cells requiring an equation correspond to the estimated displacement (D_H).

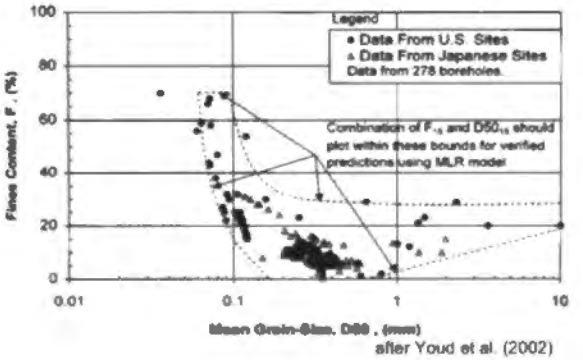

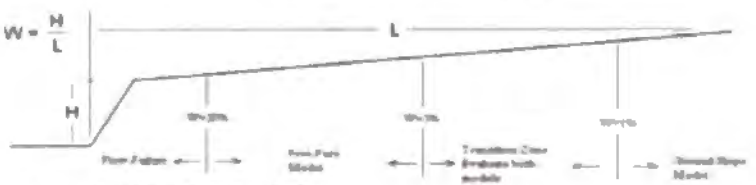

Youd et al. (2002) - Lateral Spreading Analysis

Variables that influence lateral spreading evaluation		Minimum	Maximum
D_H (m)	Estimated horizontal displacement	0.1 m	6 m
M_w	Earthquake moment magnitude	6	8
R_f (km)	Distance to vertical projection of fault	0.5 km	
H (m)	Height of free-face exposure		
L (m)	Distance from free-face		
W (%)	Ratio of free-face height (H) to Distance (L) = H/L*100	1%	20%
T_{15} (m)	Cumulative thickness of soil with $(N_1)_{60}$<15	1 m	15 m
F_{15} (%)	Average fines content of T_{15}	The combination should plot within bounds on figure to the right	
$(D_{50})_{15}$ (mm)	Mean grain size for liquefiable (N<15) layer		
S (%)	Slope of the surface topography being analyzed	0.1%	6%
Z_1	Depth to top of liquefied layer	1 m	10 m

Notes: Estimates are for stiff soil (W. US & Japan), other areas use correction for attenuation (see tab B)

If D_H>10m, relationship is innaccurate but anticipate large displacement

if $(D_{50})_{15}$ > 1mm, then sufficiently impeded drainage is necessary

after Youd et al. (2002)

$\log D_H = -16.713 + 1.532 M_w - 1.406 \log(R + 10^{(0.89M-5.64)}) - 0.012R + 0.592 \log W + 0.540 \log T_{15} + 3.413 \log(100 - F_{15}) - 0.795 \log((D_{50})_{15} + 0.1\text{mm})$

Free-Face Component

M_w	R_f (km)	H (m)	L (m)	W (%)	T_{15} (m)	F_{15} (%)	$(D_{50})_{15}$ (mm)	S (%)	FF - D_H (m)
6.7	10	0.001	107	0.00	12	35	0.7		0.00
6.7	10	0.001	100	0.00	12	35	0.7		0.00
6.7	10	0.001	95	0.00	12	35	0.7		0.00
6.7	10	0.001	90	0.00	12	35	0.7		0.00
6.7	10	0.001	85	0.00	12	35	0.7		0.00
6.7	10	0.001	80	0.00	12	35	0.7		0.00
6.7	10	0.001	75	0.00	12	35	0.7		0.00
6.7	10	0.001	70	0.00	12	35	0.7		0.00
6.7	10	0.001	65	0.00	12	35	0.7		0.00
6.7	10	0.001	60	0.00	12	35	0.7		0.00
6.7	10	0.001	55	0.00	12	35	0.7		0.00
6.7	10	0.001	50	0.00	12	35	0.7		0.00
6.7	10	0.001	45	0.00	12	35	0.7		0.00
6.7	10	0.001	40	0.00	12	35	0.7		0.00
6.7	10	0.001	35	0.00	12	35	0.7		0.00
6.7	10	0.001	30	0.00	12	35	0.7		0.00

$\log D_H = -16.213 + 1.532 M_w - 1.406 \log(R + 10^{(0.89M-5.64)}) - 0.012R + 0.338 \log S + 0.540 \log T_{15} + 3.413 \log(100 - F_{15}) - 0.795 \log((D_{50})_{15} + 0.1\text{mm})$

Ground Slope Component

M_w	R_f (km)	H (m)	L (m)	W (%)	T_{15} (m)	F_{15} (%)	$(D_{50})_{15}$ (mm)	S (%)	GS - D_H (m)
6.7	10				12	35	0.7	1.60	0.21
6.7	10				12	35	0.7	1.60	0.21
6.7	10				12	35	0.7	1.60	0.21
6.7	10				12	35	0.7	1.60	0.21
6.7	10				12	35	0.7	1.60	0.21
6.7	10				12	35	0.7	1.60	0.21
6.7	10				12	35	0.7	1.60	0.21
6.7	10				12	35	0.7	1.60	0.21
6.7	10				12	35	0.7	1.60	0.21
6.7	10				12	35	0.7	1.60	0.21
6.7	10				12	35	0.7	1.60	0.21
6.7	10				12	35	0.7	1.60	0.21
6.7	10				12	35	0.7	1.60	0.21
6.7	10				12	35	0.7	1.60	0.21
6.7	10				12	35	0.7	1.60	0.21
6.7	10				12	35	0.7	1.60	0.21

L (m)	D_H (m)
107	0.21
100	0.21
95	0.21
90	0.21
85	0.21
80	0.21
75	0.21
70	0.21
65	0.21
60	0.21
55	0.21
50	0.21
45	0.21
40	0.21
35	0.21
30	0.21

Figure A-5: Spreadsheet for Youd et al. (2002) Model

The equations used to evaluate the horizontal displacement depend on the geometry of the site. For the Youd et al. (2002) tab (Figure A-5), the Free-face model and the ground slope model are evaluated separately, and the estimated displacement (the last column in Figure A-5) is equal to the maximum value produced after evaluating both models. The equations for the different models are:

Free-Face Geometry Condition:

$$\log(D_H) = -16.713 + 1.532M_w - 1.406\log(R^*) - 0.012R_f + 0.593\log(W) + 0.540\log(T_{15}) + 3.413\log(100 - F_{15}) - 0.795\log(D_{50} + 0.1) \quad \text{A-21}$$

Ground Slope Geometry Condition:

$$\log(D_H) = -16.213 + 1.532M_w - 1.406\log(R^*) - 0.012R_f + 0.338\log(S) + 0.540\log(T_{15}) + 3.413\log(100 - F_{15}) - 0.795\log(D_{50} + 0.1) \quad \text{A-22}$$

Step 5: The last tab to require manual input corresponds to the Zhang et al. (2004) model (Figure A-6) which requires a graphical interpolation to determine the maximum cyclic shear strain. The maximum cyclic shear strain is estimated by plotting the factor of safety against liquefaction on the abscissa, moving up the plot to the appropriate relative density, and sliding left to the value of the maximum cyclic shear strain on the ordinate. The maximum cyclic shear strain values are then input into the appropriate cells on the Zhang et al. (2004) tab (Figure A-6). The remainder of the cells are linked to the results of previous tabs or filled with an appropriate equation. The required equations are:

Lateral Displacement Index (LDI):

$$LDI = \int_0^{z_{max}} \gamma_{max} * dz \quad \text{A-23}$$

Zhang et al. (2004) - Estimating Liquefaction-Induced Lateral Displacement

D_r (%)	Relative density of soil
$(N_1)_{60cs}$	Equivelant clean sand normalized SPT blow-count
FS_{liq}	Factor of Safety against liquefaction
γ_{max} (%)	Maximum cyclic shear strain
LDI_i (ft)	Lateral Displacement Index
S (%)	Slope of the surface topography being analyzed
L	Distance from the free-face
H	Height of free-face exposure
D_H	Estimated lateral displacement

$FF\text{-}D_H = LDI * 6(L/H)^{-0.8}$

$GS\text{-}D_H = LDI * (S+0.2)$

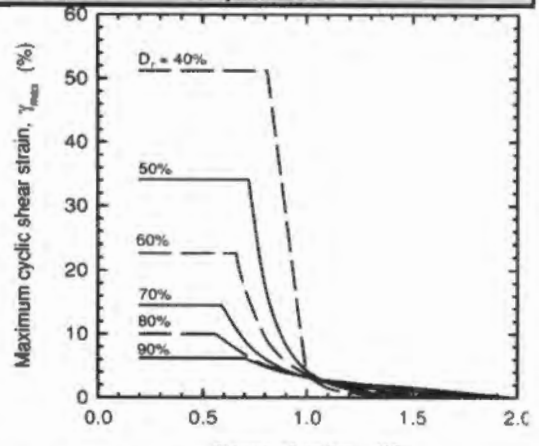

Depth (ft)	$(N_1)_{60cs}$	D_r (%)	FS_{liq}	γ_{max} (%)	LDI_i (ft)
4	13	51	1.24	2	0.08
8	12	49	0.80	26	1.04
12	12	48	0.65	38	1.52
16	21	63	0.75	12	0.48
20	19	62	0.69	18	0.72
24	18	60	0.66	22	0.88
28	18	59	0.64	24	0.96
32	17	57	0.62	25	1
36	10	45	0.45	44	1.76
40	10	44	0.45	44	1.76
44	10	43	0.45	44	1.76
48	9	43	0.45	44	1.76
52	9	42	0.46	44	1.76
56	9	41	0.46	44	1.76
60	23	67	0.98	4	0.16
64	23	66	0.96	4	0.16
68	22	65	0.94	4	0.16
72	21	65	0.93	4	0.16
76	21	64	0.91	4	0.16
80	20	63	0.89	4	0.16
84	20	62	0.88	4	0.16
				LDI =	18.36

L (m)	H (m)	S (%)	LDI (ft)	$FF\text{-}D_H$ (ft)	$GS\text{-}D_H$ (ft)	D_H (m)
107	0	1.60	18.36	0.01	3.97	1.32
100	0	1.60	18.36	0.01	3.97	1.32
95	0	1.60	18.36	0.01	3.97	1.32
90	0	1.60	18.36	0.01	3.97	1.32
85	0	1.60	18.36	0.01	3.97	1.32
80	0	1.60	18.36	0.01	3.97	1.32
75	0	1.60	18.36	0.01	3.97	1.32
70	0	1.60	18.36	0.01	3.97	1.32
65	0	1.60	18.36	0.02	3.97	1.32
60	0	1.60	18.36	0.02	3.97	1.32
55	0	1.60	18.36	0.02	3.97	1.32
50	0	1.60	18.36	0.02	3.97	1.32
45	0	1.60	18.36	0.02	3.97	1.32
40	0	1.60	18.36	0.02	3.97	1.32
35	0	1.60	18.36	0.03	3.97	1.32
30	0	1.60	18.36	0.03	3.97	1.32

Figure A-6: Spreadsheet for Zhang et al. (2004) Model

Displacement in Ground Slope Geometry Condition:

$$LD = LDI(S + 0.2) \qquad \text{A-24}$$

Displacement in Free-Face Geometry Condition:

$$LD = LDI[6(\frac{L}{H})^{-0.8}] \qquad \text{A-25}$$

The last lateral spreading model (Idriss and Boulanger, 2008; Figure A-7), requires no additional input. All the values in this tab are linked or filled with equations.

Idriss and Boulanger (2008) - Estimating Liquefaction-Induced Lateral Displacement

$(N_1)_{60}$	Normalizeed Standard Penetration Test (SPT) blow-count (for overburden and energy efficiency)
$(N_1)_{60cs}$	Equivelant clean sand normalized SPT blow-count
FS_{liq}	Factor of Safety against liquefaction
γ_{lim} (%)	Maximum cyclic shear strain
γ_{max} (%)	Maximum cyclic shear strain
F_α	Factor for determining the valid γ_{max} equation
Z_{max}	Depth to the point where all layers have FS>2
LDI	Lateral Displacement Index
S (%)	Slope of the surface topography being analyzed
L	Distance from the free-face
H	Height of free-face exposure
LD	Estimated lateral displacement

If $FS_{liq}>2$	γ_{max} (used) = 0
If $2>FS_{liq}>F_\alpha$	γ_{max} (used) = minimum of γ_{lim} and γ_{max} (calculated)
If $FS_{liq}>F_\alpha$	γ_{max} (used) = γ_{lim}

$\gamma_{lim}=1.859[1.1-\sqrt{((N_1)_{60cs}/46)}]^3$
$\gamma_{max}=0.35(2-FS_{liq})[(1-F_\alpha)/(FS_{liq}-F_\alpha)]$
$F_\alpha=0.032+0.69\sqrt{((N_1)_{60cs}})-0.13(N_1)_{60cs}$

Depth (ft)	$(N_1)_{60cs}$	F_α	FS_{liq}	γ_{lim}	γ_{max} (calculated)	γ_{max} (used)	LDI_i (ft)
4	13.09	0.83	1.24	0.34	0.01	0.01	0.05
8	12.41	0.85	0.80	0.36	-0.14	0.36	1.45
12	11.93	0.86	0.65	0.38	-0.03	0.38	1.53
16	20.56	0.49	0.75	0.15	0.09	0.09	0.34
20	19.39	0.55	0.69	0.17	0.15	0.15	0.59
24	18.42	0.60	0.66	0.19	0.32	0.19	0.76
28	17.59	0.64	0.64	0.21	-17.62	0.21	0.83
32	16.86	0.67	0.62	0.22	-0.32	0.22	0.90
36	10.28	0.91	0.45	0.46	-0.01	0.46	1.83
40	9.93	0.92	0.45	0.48	-0.01	0.48	1.91
44	9.61	0.92	0.45	0.49	-0.01	0.49	1.98
48	9.31	0.93	0.45	0.51	-0.01	0.51	2.04
52	9.03	0.93	0.46	0.53	-0.01	0.53	2.11
56	8.78	0.94	0.46	0.54	-0.01	0.54	2.17
60	23.19	0.34	0.98	0.11	0.04	0.04	0.15
64	22.50	0.38	0.96	0.12	0.04	0.04	0.16
68	21.85	0.42	0.94	0.13	0.04	0.04	0.16
72	21.24	0.45	0.93	0.14	0.04	0.04	0.17
76	20.67	0.48	0.91	0.15	0.05	0.05	0.18
80	20.13	0.51	0.89	0.16	0.05	0.05	0.20
84	19.61	0.54	0.88	0.17	0.05	0.05	0.21
						LDI =	18.64

L (m)	H (m)	S (%)	LDI (ft)	FF-D_H (ft)	GS-D_H (ft)	D_H (m)
107	0	1.60	18.64	0.01	4.03	1.34
100	0	1.60	18.64	0.01	4.03	1.34
95	0	1.60	18.64	0.01	4.03	1.34
90	0	1.60	18.64	0.01	4.03	1.34
85	0	1.60	18.64	0.01	4.03	1.34
80	0	1.60	18.64	0.01	4.03	1.34
75	0	1.60	18.64	0.01	4.03	1.34
70	0	1.60	18.64	0.01	4.03	1.34
65	0	1.60	18.64	0.02	4.03	1.34
60	0	1.60	18.64	0.02	4.03	1.34
55	0	1.60	18.64	0.02	4.03	1.34
50	0	1.60	18.64	0.02	4.03	1.34
45	0	1.60	18.64	0.02	4.03	1.34
40	0	1.60	18.64	0.02	4.03	1.34
35	0	1.60	18.64	0.03	4.03	1.34
30	0	1.60	18.64	0.03	4.03	1.34

After Zhang (2004) Calibartion Model

Figure A-7: Spreadsheet for Idriss and Boulanger (2008) Model

The Idriss and Boulanger (2008) approach eliminates the necessity to interpolate a plot, but added programming is required. The value for the maximum potential shear strain (γ_{max}) requires a triple IF statement in order to operate properly, but once it is applied, this model runs much smoother than the Zhang et al. (2004). The equations required for the Idriss and Boulanger (2008) tab are:

Limiting Shear Strain (γ_{lim}):

$$\gamma_{lim} = 1.859(1.1 - \sqrt{\frac{(N_1)_{60cs}}{46}}) \qquad \text{A-26}$$

Alpha Factor (F_α):

$$F_\alpha = 0.032 + 0.69\sqrt{(N_1)_{60cs}} - 0.13(N_1)_{60cs} \qquad (\text{for } (N_1)_{60cs} \geq 7) \qquad \text{A-27}$$

Maximum Potential Shear Strain (γ_{max}):

$$\gamma_{max} = 0 \qquad (\text{if } FS_{liq} \geq 2) \qquad \text{A-28a}$$

$$\gamma_{max} = \min[\gamma_{lim}, 0.035(2 - FS_{liq})(\frac{1 - F_\alpha}{FS_{liq} - F_\alpha})] \qquad (\text{if } 2 > FS_{liq} > F_\alpha) \qquad \text{A-28b}$$

$$\gamma_{max} = \gamma_{lim}\ b \qquad (\text{if } FS_{liq} \leq FS_\alpha) \qquad \text{A-28c}$$

The Idriss and Boulanger (2008) model also requires calibration equations, but they did not provide independent equations. Therefore, the calibration suggested by Zhang et al. (2004) was used. These equations are presented as A-23 to A-25.

Step 6: The final step is to compare the results of all four models in the comparison tab (Figure A-8), which can also be illustrated graphically by plotting the results of each model versus distance (graphical comparisons can be seen in the sensitivity study of this thesis, Figures 4-6 to 4-14. All these columns are linked to the results of the previous tabs.

L (m)	Empirical Models				Shear Strain Potential Models	
	R-EPOLLS D_H (m)	S-EPOLLS D_H (m)	G-EPOLLS D_H (m)	Youd (02) D_H (m)	Zhang (04) D_H (m)	I + D (08) D_H (m)
107	0.29	0.18	0.55	0.21	1.32	1.34
100	0.29	0.18	0.55	0.21	1.32	1.34
95	0.29	0.18	0.55	0.21	1.32	1.34
90	0.29	0.18	0.55	0.21	1.32	1.34
85	0.29	0.18	0.55	0.21	1.32	1.34
80	0.29	0.18	0.55	0.21	1.32	1.34
75	0.29	0.18	0.55	0.21	1.32	1.34
70	0.29	0.18	0.55	0.21	1.32	1.34
65	0.29	0.18	0.55	0.21	1.32	1.34
60	0.29	0.18	0.55	0.21	1.32	1.34
55	0.29	0.18	0.55	0.21	1.32	1.34
50	0.29	0.18	0.55	0.21	1.32	1.34
45	0.29	0.18	0.55	0.21	1.32	1.34
40	0.29	0.18	0.55	0.21	1.32	1.34
35	0.29	0.18	0.55	0.21	1.32	1.34
30	0.29	0.18	0.55	0.21	1.32	1.34
			Average =	0.21		

Figure A-8: Tabular Comparison Sheet for Lateral Spreading Methods

REFERENCES

Ambraseys, N. N. and Sarma, S., (1969) "Liquefaction of Soils Induced by Earthquakes," *Bulletin*, Seismological Society of America, 59(2), 651-664.

Ashford, S.A., Juirnarongrit, T., Sugano, T., and Hamada, M. (2006), "Soil-Pile Response to Blast-Induced Lateral Spreading I: Field Test," *J. Geotech. And Geoenviron. Eng.*, 132(2), 152-162

Bartlett, S. M. and Youd, T. L. (1992), "Empirical Analysis of Horizontal Ground Displacement Generated by Liquefaction-Induced Lateral Spread," *Technical Report NCEER-92-0021*, National Center for Earthquake Engineering Research, Buffalo, New York.

Bartlett, S. M. and Youd, T. L. (1995), "Empirical Prediction of Liquefaction-Induced Lateral Spread," *J. Geotech. Eng.*, 121(4), 316-329.

Baziar, M. H., Dobry, R., and Elgamel, A. W. M. (1992), "Engineering Evaluation of Permanent Ground Deformations Due to Seismically-Induced Liquefaction," *Technical Rprot NCEER-92-0007*, National Center for Earthquake Engineering Research, State University of New York, Buffalo.

Braile et al. (1986), "Tectonic Development of the New Madrid Rift Complex, Mississippi Embayment, North America," *Tectonophysics,* 131 (1986) 1-21, Elsevier Science Publishers B.V., Amsterdam.

Boulanger, R. W. and Idriss, I. M. (2004) "Evaluating the Potential for Liquefaction or Cyclic Failure of Silts and Clays," Report No. UCD/CGM-04101, UC-Davis.

Casagrande, A. (1936) "Characteristics of Cohesionless Soils Affecting the Stability of Earth Fills," *Journal of the Boston Society of Civil Engineers,* Jan., 1936 (reprinted in "Contributions to Soil Mechanics, 1925-1960," Boston Society of Civil Engineers, Oct., 1940)

Castro, G., (1969), "Liquefaction of Sands," *Harvard Soil Mechanics Series*, No. 81, HarvardUniversity, Cambridge, Mass.

Chen, G., Anderson, N., Luna, R., Stephenson, R., El-Engebawy, M., Silva, P., and Zoughi, R. (2005), "Earthquake hazards Assessment and Mitigation: A Pilot Study in the New Madrid Seismic Zone" *FHWA, Contract Number: DTFH61-02-X-00009.*

Doyle, B. and Rogers, J. D. (2005), "Seismically Induced Lateral Spread Features in the Western New Madrid Seismic Zone" *Environmental and Engineering Science,* vol. XI, no. 3, pp 251-258.

Ervin, P. C. and McGinnis, L. D. (1975), "Reelfoot Rift: Reactivated Precursor to the Mississippi Embayment," *Geological Society of America Bulletin*, v. 86, p. 1287-1295.

Faris, A., Seed, R., Kayen, R. and Wu, J., (2006) "A Semi-Empirical Model for the Estimation of Maximum Horizontal Displacement due to Liquefaction Induced Lateral Spreading" *8th National Conference on Earthquake Engineering*, EERI, San Francisco, CA.

Fuller, M. L. (1912), "The New Madrid Earthquake" *U.S. Geological Survey Bulletin 494*.

Grohskopf, J. G. (1955), Subsurface Geology of the Mississippi Embayment of Southeast Missouri, *State of Missouri Department of Business and Administration*, Von Hoffman Press, Jefferson City, MO.

Hamada, M., Yasuda, S., Isoyama, R., and Emoto, K. (1986), "Study on Liquefaction Induced Permanent Ground Displacements," *Report for the Association for the Development of Earthquake Prediction.*

Hashash, Y. and Park, D. (2001), "Non-linear One-dimensional Seismic Ground Motion Propagation in the Mississippi Embayment," *Engineering Geology*, 62 (2001) 185-206.

Hitt, R. (2001), "Missouri Highway and Transportation Commission Plans for State Highway: Approach Spans Cape Girardeau County, Missouri to Alexander County, Illinois" Missouri Department of Transportation, Project No. ACBRF-BRF-74-1(11), Job No. JOUO321B.

Idriss, I. M. and Boulanger, R. W. (2004), "Semi-Empirical Proceedures for Evaluating Liquefaction Potential during Earthquakes," Proceedings of the 11th International Conference on Soil Dynamics and Earthquake Engineering and the 3rd International Conference on Earthquake Geotechnical Engineering, Jan. 2004, pp32-56.

Idriss, I. M. and Boulanger, R. W. (2008), "Soil Liquefaction During Earthquakes," *Earthquake Engineering Research Institute*, MNO-12.

Ishihara, K. and Yoshimine, M., (1992) "Evaluation of Settlements in Sand Deposits Following Liquefaction during Earthquakes" *Soils and Foundations*, 32(1), pp 173-88.

Johnston, A. C. and Schweig, E. S. (1996), "The Enigma of the New Madrid Earthquakes of 1811-1812" *Annual Rev. Earth Planet SCI*, vol. 24, 339-384.

Kolata, D. R., Treworgy, J. D., and Masters J. M. (1980), "Structural Framework of the Mississippi Embayment of Southern Illinois" *Illinois State Geological Survey, NUREG/CR-1877,* March 1981.

Kramer, S., (1996) Geotechnical Earthquake Engineering, Prentice Hall, Upper Saddle River, NJ 07458.

Kramer, S., (2008) "Evaluation of Liquefaction Hazards in Washington State" *Washington State Department of Transportion,* Report No. WA-RD 668.1.

LaPrensa (2009), "Puento sobre el río Humuya se desploma", http://www.laprensahn.com/Pa%C3%ADs/Ediciones/2009/06/29/Noticias/Puente-sobre-el-rio-Humuya-se-desploma, (July 7, 2009).

Luna, R., Belarbi, A., Applegate, K., Rodriguez, R., and Calderon, H (2009), "Reconnaissance Report of the May 28, 2009 Honduras Earthquake, M 7.3", http://www.geerassociation.org/Post_EQ_Reports.html, (August 5, 2009).

McKeown, F. A. (1982), "Investigations of the New Madrid Earthquake Region: Overview and Discussion" *Geological Survey Professional Paper 1236,* pp 1-14.

Meyerhof, G. G. (1957), "Discussion on Research on Determining the Density of Sand," *Proc., 4th Int. Conf. of Soil Mechanics and Foundation Engineering*, London, Vol. 3, No. 110.

Mooney, W., Andrews, M., Ginzburg, A., Peters, D. and Hamilton, R. (1983), "Crustal Structure of the Northern Mississippi Embayment and a Comparison with other Continental Rift Zones," *Tectonophysics,* 94 (1983) 327-348, Elsevier Science Publishers B.V., Amsterdam.

Newmark, N.M., (1965) "Effects of Earthquakes on Dams and Embankments," *Geotechnique*, London, England, 15(2) June 1965, pp139-160

Nuttli, O. W. (1982) "Investigations of the New Madrid Earthquake Region: Damaging Earthquakes of the Central Mississippi Valley" *Geological Survey Professional Paper 1236,* pp 15-20.

Obermeier, S. F. (1988), "Liquefaction Potential in the Central Mississippi Valley" *U.S. Geological Survey Bulletin 1832.*

Obermeier, S. F., Olson, Scott M., and Green, Russell A. (2005), "Field Occurrences of Liquefaction-Induced Features: A Primer for Engineering Geological Analysis of Paleoseismic Shaking" *Engineering Geology 76,* 209-234.

Olson, S. M., Cooling, T. L., and Hague, S. T. (2004), "Geotechnical Earthquake Engineering for the Great River Bridge" *Proceedings: Fifth International Conference on Case Histories in Geotechnical Engineering*, New York, NY April 13-17, 2004.

Olson, S. M. and Johnson, C. I. (2008), "Analyzing Liquefaction-Induced lateral Spreads Using Strength Ratios," *J. Geotech. And Geoenviron. Eng.*, 134(8), pp1035-1049.

Rauch, A. and Martin, J. (2000), "EPOLLS Model for Predicting Average Displacements on Lateral Spreads" *Journal of Geotechnical and Geoenvironmental Engineering*, 126(4), pp 360-371.

Saltelli, A., Tarantola, S., and Chan, K. (1999), "Quantitative Model-Independent Method for Global Sensitivity Analysis of Model Output" *Technometrics*, 41(1), 39-56.

Seed, H. B. (1979), "Soil Liquefaction and Cyclic Mobility Evaluation for Level Ground during Earthquakes," *Journal of the Geotechnical Engineering Division*, ASCE, Vol. 105, No. GT2, Feb. 1979, pp 201-255.

Seed, H. B., Tokimatsu, K., Harder, L. F., and Chung, R. M. (1985), "Influence of SPT Procedures in Soil Liquefaction Resistance Evaluation," *Journal of Geotechnical Engineering*, ASCE, 111(12), pp. 1425-1445.

Shamoto, Y., Zhang, J., and Tokimatsu, K., (1998) "Methods for Evaluating Residual Post-Liquefaction Ground Settlement and Horizontal Displacement, Special Issue on Geotechnical Aspects of the January 17, 1995 Hyogoken-Nambu Earthquake, No. 2" *Soils and Foundations*, Japanese Geotechnical Society, pp 69-84.

Tatsuoka, F., Zhou, S., Sato, T., and Shibuya, S. (1990), "Method of Evaluating Liquefaction Potential and its Application," *Rep. on Seismic Hazards in the Soil Deposits in Urban Areas*, Ministry of Education of Japan, 75-109 (in Japanese)

Tokimatsu, K. and Asaka, Y., (1998) "Effects of Liquefaction-Induced Ground Displacement on Pile Performance in the 1995 Hyogoken-Nambu Earthquake" *Soils and Foundaitons*, Special Issue, Japanese Geotechnical Society, pp 163-77.

Toro, G.R., Abrahamson, N.A., and Schneider, J.F. (1997), "Model of Strong Ground Motions from Earthquakes in the Central and Eastern North America: Best Estimates and Uncertainties" *Seismic Research Letters*, 68, 41-57.

Tuttle, M. P. (2001), "The use of Liquefaction Features in Paleoseismology: Lessons Learned in the New Madrid Seismic Zone, Central United States" *Journal of Seismology* 5:361-380, Kluwer Academic Publishers.

Tuttle, M. P., Schweig, E. S., Sims, J. D., Lafferty, R. H., Wolf, L. W., and Haynes, M. L. (2002), "The Earthquake Potential of the New Madrid Seismic Zone" *Bulletin of the Seismological Society of America,* vol. 92, pp 2080-2089, Aug 2002.

U.S. Geological Survey (2009), "M7.3 Honduras Earthquake of 28 May 2009", Poster, ftp://hazards.cr.usgs.gov/sigeqs/20090528/20090528.pdf, (June 20, 2009).

Wang, W., Chen, G., and Hartnagel, B. (2007), "Real-time Condition Assessment of the Bill Emerson Cable-Stayed Bridge using Artificial Neural Networks" *SPIE*, paper 6529-56.

Watkins, C. (2009), *Personal Communications via E-mail*, 01 October 2009.

Woodward-Clyde Consultants, (1994) "Geotechnical Seismic Evaluation of Proposed New Mississippi River Bridge (A-5076), Cape Girardeau, MO" *Report No: 93C8036-500.*

Youd, T. L. (1997) "Liquefaction-Induced Damage to Bridges" Post-Earthquake Reconstruction Strategies: NCEER-INCEDE Center-to-Center Project, Proceedings of the Workshop on Earthquake Engineering Frontiers in Transportation Facilities, August 29, 1997.

Youd, T., Idriss, I., Andrus, R., Arango, I., Castro, G., Christian, J., Dobry, R., Finn, W., Harder, L., Hynes, M., Ishihara, K., Koester, J., Liao, S., Marcuson III, W., Martin, G., Mitchell, J., Moriwaki, Y., Power, M., Robertson, P., Seed, R., Stokoe, K. (2001), "Liquefaction Resistance of Soils: Summary Report from the 1996 NCEER and 1998 NCEER/NSF Workshops on Evaluation of Liquefaction Resistanc of Soils," *J. Geotech. Geoenviron. Eng.*, 127(10), 817-833.

Youd, T. L., Hansen, C. M., and Bartlett, S. F. (2002), "Rvised Multi-Linear Regression Equations ofr Prediction of Lateral Spread Displacement," *J. Geotech. Geoenviron. Eng.*, 128(12), 1007-1017

Yungul, S. H. (1971), "Magnetic Anomolies and the Possibilities of Continental Drifting in the Gulf of Mexico" *Journal of Geophysical Research,* vol. 76, pp 2639-2642.

Zhang, G., Robertson, P. K., and Brachman, R. W. I. (2004), "Estimating Liquefaction-Induced Lateral Displacements Using the Standard Penetration Test or Cone Penetration Test," *J. Geotech. And Geoenviron. Eng.*, 131(8), 861-871.

VITA

Kermit Nathanial Applegate was born on September 27, 1980 to Kermit Warren and Jody Marlene Applegate in the small town of Port Angeles, WA. There is where he spent most of his childhood. After high school, Kermit neglected his zeal for academics and engaged in the more primitive pursuit of Naval Special Warfare, but four years of driving speed boats over rough ocean swells was enough to satiate his childhood fantasies.

Once relieved of his duty, Kermit re-initiated his intellectual growth and by May 2005 obtained an Associate of Arts degree from Peninsula College in Port Angeles, WA. Upon completion of his AA, he enrolled in the University of Missouri – Rolla, where he earned a Bachelor of Science degree in civil engineering in May 2008. In April of that same year, Kermit obtained his Engineering Intern classification, but continued to attend UMR while it redefined itself as Missouri University of Science and Technology (Missouri S&T). Currently, Kermit is a Chancellor's fellow at Missouri S&T in pursuit of a May 2010 Master of Science degree in Civil Engineering.